Menno W.J. Prins

Magnetic imaging with photoexcited semiconductor tips in scanning tunneling microscopy

Magnetic imaging
with photoexcited semiconductor tips
in scanning tunneling microscopy

Menno W.J. Prins

Magnetic imaging
with photoexcited semiconductor tips
in scanning tunneling microscopy

een wetenschappelijke proeve op het gebied van
de Natuurwetenschappen

Proefschrift

ter verkrijging van de graad van doctor aan
de Katholieke Universiteit Nijmegen,
volgens besluit van het College van Decanen
in het openbaar te verdedigen op
donderdag 16 november 1995,
des namiddags te 3.30 uur precies

door

Menno Willem José Prins

geboren op 18 april 1967
te Renkum

Promotor: Prof. Dr. H. van Kempen

Nu dit proefschrift met alle punten en komma's het daglicht kan aanschouwen, wil ik de vele mensen bedanken die mijn vier Nijmeegse jaren tot een aangename, leerzame en produktieve tijd hebben gemaakt. In mijn ogen zijn regelmatige samenwerking en intense discussies essentieel voor het plezier en de vooruitgang in het onderzoek. In dit perspectief heb ik veel te danken aan Daniel, Ronnie, Maurice, Rogier, Ap en Herman. Ik bedank Daniel Abraham, die me wegwijs maakte in de mogelijkheden en onmogelijkheden van het tunnelen met gallium-arseen; Ronnie Jansen, voor de discussies die we met grote regelmaat en vaak even grote vasthoudendheid voerden; Maurice van der Wielen, voor zijn experimentele ijver en opgeruimde humeur; Rogier Groeneveld en Ap van Gelder, voor het openen van hun experimentele respectievelijk theoretische trucendozen; en Herman van Kempen, voor het vertrouwen en de vrijheid die hij me altijd gaf, en voor de dwarsverbanden die hij in onze werkbesprekingen regelmatig wist te leggen. Hoewel de resultaten niet in dit proefschrift zijn opgenomen, heb ik ook prettig samengewerkt met Ruud Vullers en Michael Stoelinga in de STM-experimenten, en met Harald Wierenga en Theo Rasing op het gebied van magnetisatie-geïnduceerde tweede-harmonische generatie. Ook wil ik vermelden dat Theo aan de basis stond van het projectvoorstel waaraan ik heb gewerkt. Erik van Leuken en Rob de Groot hebben me veel geleerd over de bandenstructuur van magnetische materialen. Huub Salemink bedank ik voor zijn kritische kommentaar op de eindtekst.

Op het gebied van de instrumentatie ben ik veel dank verschuldigd aan Jan Hermsen, Jan Gerritsen en Albert van Etteger. Ook kreeg ik hulp van Cees Beers, Adriaan van 't Hof, Jan van Huet, Frits Schut, Ran van Dongen, Henk Nijenhuis, R. Gelsing, W. Leenders, W. Corbeek en Ferry Derksen. Veel personen hebben aan dit onderzoek bijgedragen via het aanleveren van preparaten: André van Geelen prepareerde GaAs epilagen en membranen; Hans van Kesteren, H. Donkersloot en J. Kerkhof van Philips Research leverden de Pt/Co multilagen; Wim Van Roy en Jo De Boeck van het IMEC in Leuven fabriceerden de MBE-gegroeide preparaten met AlAs en τ-MnAl; Uwe Hartmann van de KFA in Jülich stelde Ni tips beschikbaar; Bernard Rousseeuw en Emiel van der Drift van DIMES in Delft prepareerden een patroon van aluminiumlijnen op glas; Willem van der Vleuten en Maarten Leys van de TU Eindhoven leverden GaAs preparaten; en Claude Chappert van de Université Paris-Sud stelde epitaxiaal goud op glas beschikbaar. In aanvulling hierop zou ik een lange lijst van personen op kunnen stellen die met het beantwoorden van vragen of door korte inspirerende gedachtenwisselingen het onderzoek telkens langs een volgende haarspeldbocht wisten te leiden. Elke bocht was essentieel, zodat ik ook die personen wil bedanken voor hun hulp en welwillendheid.

De afgelopen periode was niet alleen op vakinhoudelijk terrein waardevol, maar evenzeer vanwege de mensen die ik mocht ontmoeten. In dit opzicht heb ik het in de ambiance van de vakgroep EVSF2, met het duo Riki-Margriet als centraal aanspreekpunt, erg naar mijn zin gehad. Buiten werktijd was het altijd goed wat muzikale nootjes te kraken, waarvoor ik de leden van het Micro-Canoniek Ensemble en van

de salsaformaties Ayakamata en Macchina O bedank. Tenslotte is er de belangrijke achterban: Jos en Willem, die veel voor mij betekenen en mijn academische vorming altijd hebben ondersteund, Pjotr, Duke, Wendy, andere familieleden, vrienden en vriendinnen. Zonder de bovenstaande personen was mijn promotie-onderzoek onmogelijk geweest, en zeker uiterst saai. Dat laatste is me gespaard gebleven, ook dankzij de gezelligheid en kleurrijke invallen van Cilia.

Het waren vier goede jaren.

Contents

Chapter 1

General introduction to magnetic imaging

The understanding of the micromagnetic structure of surfaces and interfaces represents a great challenge for present-day researchers in solid-state physics. This subject of research is greatly stimulated by recent discoveries such as the perpendicular magnetic anisotropy of ultrathin magnetic films, the oscillatory exchange coupling through non-magnetic spacer layers, and the giant magneto-resistance in magnetic multilayers (e.g. [1]). In this perspective there is a great demand for convenient magnetic imaging techniques that allow to: (i) detect magnetic ordering on a submicrometer scale, (ii) determine the structure of magnetic domain walls with nanometer resolution, or (iii) resolve the spin-density variations of surfaces on a subnanometer scale. These wishes justify an effort directed toward the development of a magnetically sensitive scanning tunneling microscope (STM). The STM was invented in 1982 [2, 3] and is capable of imaging the topography of surfaces with atomic resolution. The present thesis deals with a the usage of semiconductor tips in a scanning tunneling microscope, in order to achieve magnetic sensitivity. To appreciate the context of this work, first we briefly discuss a selection of current magnetically sensitive imaging techniques, presented in Table 1.1. The topics addressed in this thesis are marked by an asterisk. The techniques are arranged according to their physical principle (measurement of magnetic stray field, magneto-optical effects, or electron interactions) and technical design (scanning probe or not).

The Bitter technique is based on the spreading of magnetic particles over a magnetic material [4]. The particles are attracted into areas with a high stray field gradient, yielding a pattern that can be imaged with an optical or an electron microscope. The Bitter technique is easy to use, but lacks the ability to give quantitative information on the underlying magnetic domain structure. Lorentz microscopy refers to the

1

	not scanning probe		scanning probe	
magnetic field	Bitter technique	[4]	MFM	[9]
	Lorentz microscopy	[5]	Hall probe	[10]
magneto-optical	optical far-field	[6]	optical near-field*	
electron microscopy	SEMPA	[7]	spin-polarized tunneling*	

Table 1.1: A selection of magnetic imaging techniques with a lateral magnetic resolution of one micrometer or less. The asterisk* marks the topics addressed in this thesis.

measurement of the deflection or phase-change of an electron beam in a transmission electron microscope (TEM) [5]. This technique gives quantitative magnetic information, but rather difficult thinning procedures are required to render the sample transparent to the electron beam of the TEM. The magneto-optical effects discovered by Faraday and Kerr in the last century, are at the basis of present-day magnetically sensitive optical microscopes [6]. The effects concern the dependence of the optical phase and amplitude on the sample magnetization, where the Faraday effect refers to a transmission geometry, and the Kerr effect to a reflection geometry. When used in a conventional optical microscope, the limit of lateral resolution is given by the Rayleigh diffraction limit, which tells that the resolving power is at best of the order of the optical wavelength (typically $0.5\,\mu m$). Finally, the scanning electron microscope with polarization analysis (SEMPA) records the polarization of low-energy secondary electrons being emitted from a sample that is subjected to a scanning electron beam [7]. Quantitative magnetic information is obtained from the first few atomic layers of the sample. The SEMPA as well as Lorentz microscopy operate under vacuum conditions and can yield a lateral magnetic resolution of about $20\,nm$.

The still growing family of scanning probe microscopies finds its origin in the invention of the scanning tunneling microscope (STM) in 1982 [2, 3] and the scanning force microscope in 1986 [8]. By the measurement of a tunneling current or of a cantilever deflection, these instruments allow for scanning of a pointed solid-state probe (a so-called tip) at a constant distance from the sample surface, where the probe-sample separation can be as small as one nanometer (see Fig. 1.1). The most widely used magnetically sensitive scanning probe technique is the magnetic force microscope (MFM) [9]. By scanning over a surface with a magnetic tip and varying the tip-surface separation, topographic images as well as a measurement of the gradient of the magnetic stray field can be made rather easily. Nevertheless, in order to quantitatively determine the magnetic domain structure of the sample, detailed knowledge
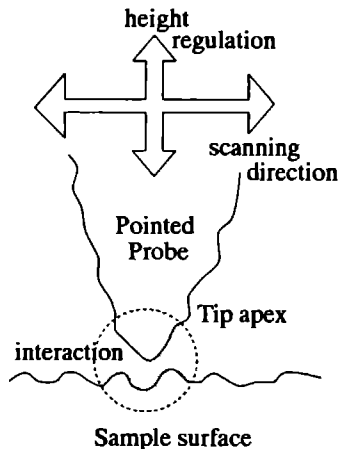
Figure 1.1: Schematic of a scanning probe microscope, where a pointed probe or tip is interacting with a sample surface. The tip-sample distance is typically one nanometer.

of the geometry and the magnetic properties of the tip is required. In addition, it is difficult to determine to what degree the stray field of the tip is disturbing the sample magnetization. A recently developed instrument with very low magnetic intrusiveness is the scanning Hall probe microscope [10], which utilizes a lithographically defined Hall bar to locally measure the magnetic stray field. Submicrometer lateral magnetic resolution has been achieved, but at present the technique is limited to cryogenic temperatures.

In a conventional optical microscope both the optical source and the optical detector are separated from the sample by a distance that is far larger than the wavelength of the light. This so-called far-field imaging is subject to the diffraction limit. It was known for a long time that the diffraction limit can be surpassed by descending into the optical near-field [11]. In practice this requires that either the optical source or the optical detector is positioned at a distance closer than the optical wavelength from the interaction volume of interest. In recent years various scanning near-field optical probes have been developed and succesfully applied to magneto-optical imaging. The first demonstration was made by Betzig *et al.* [12], using a tapered optical fibre as a local source of polarized light in a scanning force microscope. Silva *et al.* used a scanning luminescent silver particle, operating as a local detector of magneto-optical interactions [13]. In our laboratory, we demonstrated that a semiconductor tip in a scanning tunneling microscope can function as a sensitive local photodetec-

tor [14] that can be used for magneto-optical imaging [15]. The advantages of scanning magneto-optical near-field microscopes are threefold: (i) the probes are non-magnetic, so non-perturbing to the sample magnetization and insensitive to the application of a magnetic field, (ii) the microscopes can operate under ambient conditions, and (iii) the lateral magnetic resolution can be more than an order of magnitude smaller than the optical wavelength.

Finally, spin-polarized scanning tunneling microscopy deals with the development of tunneling probes that are selective to the electron spin, and thus sensitive to the spin-polarization of surface electronic states. Possible probes include tip-shaped magnetic materials [16]. Also semiconductor materials with appropriate spin-orbit interaction are probe candidates [17], where the spin-sensitivity can be achieved by optical means. More than two decades ago, optical spin-orientation of charge carriers was clearly demonstrated in spin-polarized electron sources made of cesium-covered gallium-arsenide (GaAs) [18]. The possibility of using a GaAs tip for spin-sensitive imaging is very promising, because the probe material is non-magnetic, the tip spin-orientation can be reversed by changing the optical polarization, and magnetic resolution on an atomic scale can be achieved in principle.

In this thesis we will report on studies of electron tunneling from photoexcited GaAs, with the aim of developing a magnetically sensitive scanning tunneling microscope. In Chapter 2 a model description as well as experimental investigations are presented on the (non spin-polarized) electrical transport that occurs in a photoexcited tunnel junction between a semiconductor and a non-magnetic metal [19]. In Chapter 3 we will present results on magneto-optical near-field imaging with a GaAs tip in a scanning tunneling microscope [20], with a subwavelength lateral magnetic resolution; it will be pointed out that with these tips a magneto-optical resolution of 10 nm is achievable in principle. Chapter 4 involves a model description of spin-dependent transport as well as experiments on the detection of spin-polarized tunneling by optical spin-orientation [21].

References

1. *Magnetism and structure in systems of reduced dimension,* edited by R.F.C. Farrow *et al.,* NATO-ASI series, series B: Physics vol. 309 (Plenum Press, New York, 1993).

2. G. Binnig, H. Rohrer, C. Gerber, and E. Weibel, Appl. Phys. Lett. **40**, 178 (1982).

3. Reviews on STM can be found in: *Scanning tunneling microscopy I, II, and III,* edited by R. Wiesendanger and H.-J. Güntherodt, Springer series in surface science vol. 20, 28, and 29 (Springer Verlag, Heidelberg, 1992/93); C.J. Chen, *Intro-*

duction to scanning tunneling microscopy, Oxford series in optical and imaging sciences vol. 4 (Oxford University Press, New York, 1993).

4. F. Bitter, Phys. Rev. **38**, 1903 (1931).

5. E. Fuchs, Naturwiss. **47**, 392 (1960); J.N. Chapman, J. Phys. D**17**, 623 (1984); J.N. Chapman, I.R. McFadyen, and S. McVitie, IEEE Trans. Magn. **26**, 1506 (1990).

6. For a review on magneto-optical effects see: M.J. Freiser, IEEE Trans. Magn. **4**, 152 (1968).

7. K. Koike and K. Hayakawa, Jpn. J. Appl. Phys. **23**, L187 (1984); J. Unguris, G. Hembrel, R.J. Celotta, and D.T. Pierce, J. Microscopy **139**, RP1 (1985).

8. G. Binnig, C.F. Quate, and C. Gerber, Phys. Rev. Lett. **56**, 930 (1986).

9. For a review on MFM see: P. Grütter, H.J. Mamin and D. Rugar, in *Scanning Tunneling Microscopy II*, edited by R. Wiesendanger, and H.-J. Güntherodt, Springer Series in Surface Sciences vol. 28 (Springer, Berlin, 1992), p. 151.

10. A.M. Chang, H.D. Hallen, L. Harriott, H.F. Hess, H.L. Kao, J. Kwo, R.E. Miller, R. Wolfe, J. van der Ziel, and T.Y. Chang, Appl. Phys. Lett. **61**, 1974 (1992); D.A. Brawner and N.P. Ong, J. Appl. Phys. **73**, 3890 (1993).

11. For a review on near-field optics see: D.W. Pohl, in *Scanning Tunneling Microscopy II*, edited by R. Wiesendanger and H.-J. Güntherodt, Springer Series in Surface Sciences vol. 28 (Springer, Berlin, 1992), p. 233.

12. E. Betzig, J.K. Trautman, R. Wolfe, E.M. Gyorgy, P.L. Finn, M.H. Kryder, and C.-H. Chang, Appl. Phys. Lett. **61**, 142 (1992).

13. T.J. Silva, S. Schultz, and D. Weller, Appl. Phys. Lett. **65**, 658 (1994).

14. M.W.J. Prins, M.C.M.M. van der Wielen, R. Jansen, D.L. Abraham, and H. van Kempen, Appl. Phys. Lett. **64**, 1207 (1994).

15. M.W.J. Prins, R.H.M. Groeneveld, D.L. Abraham, H. van Kempen, and H.W. van Kesteren, Appl. Phys. Lett. **66**, 1141 (1995).

16. R. Wiesendanger, H.-J. Güntherodt, G. Güntherodt, R.J. Gambino, and R. Ruf, Phys. Rev. Lett. **65**, 247 (1990).

17. S.F. Alvarado and Ph. Renaud, Phys. Rev. Lett. **68**, 1387 (1992).

18. For reviews on optical spin-orientation in GaAs see: *Optical orientation*, edited by F. Meier, and B.P. Zakharchenya, Modern problems in condensed matter sciences vol. 8 (Elsevier, Amsterdam, 1984); C. Hermann, H.-J. Drouhin, G. Lampel, Y. Lassailly, D. Paget, J. Peretti, R. Houdré, F. Ciccacci, H. Riechert, chapter 9 in *Spectroscopy of nonequilibrium electrons and phonons*, edited by C.V. Shank and B.P. Zakharchenya (Elsevier, Amsterdam, 1992) p. 397.

19. The contents of Chapter 2 were reported in *Photoamperic probes in scanning tunneling microscopy* by M.W.J. Prins, M.C.M.M. van der Wielen, R. Jansen, D.L. Abraham, and H. van Kempen, Appl. Phys. Lett. **64**, 1207-9 (1994), *Modulated photodetection with semiconductor tips in a scanning tunneling microscope* by R.H.M. Groeneveld, M.W.J. Prins, and H. van Kempen, Surf. Sci. **331-333**, 1299 (1995), *Depletion field focusing in semiconductors* by M.W.J. Prins and A.P.

van Gelder, submitted, and in *Photoelectrical properties of semiconductor tips in scanning tunneling microscopy* by M.W.J. Prins, R. Jansen, R.H.M. Groeneveld, A.P. van Gelder, and H. van Kempen, submitted.

20. The contents of Chapter 3 were reported in *Magneto-optical Faraday effect probed in a scanning tunneling microscope* by M.W.J. Prins, M.C.M.M. van der Wielen, D.L. Abraham, H. van Kempen, and H.W. van Kesteren, IEEE Trans. Magn. **30**, 4491 (1994), *Near-field magneto-optical imaging in scanning tunneling microscopy* by M.W.J. Prins, R.H.M. Groeneveld, D.L. Abraham, H. van Kempen, and H.W. van Kesteren, Appl. Phys. Lett. **66**, 1141 (1995), *Photosensitive semiconductor tips in a scanning tunneling microscope*, by M.C.M.M. van der Wielen, M.W.J. Prins, R. Jansen, D.L. Abraham, and H. van Kempen, in 'Photons and local probes', edited by O. Marti, NATO-ASI (Elsevier, Amsterdam), accepted, and *STM for magneto-optical imaging* by M.W.J. Prins, R.H.M. Groeneveld, H.W. van Kesteren, D.L. Abraham, R. Schad, and H. van Kempen, submitted.

21. The contents of Chapter 4 were reported in *Spin-dependent transmission at ferromagnet/semiconductor interfaces* by M.W.J. Prins, D.L. Abraham, and H. van Kempen, J. Magn. Magn. Mat. **121**, 109 (1993); *ibid.*, Surf. Sci. **287/288**, 750 (1993), *Spin-dependent transport in metal/semiconductor tunnel junctions* by M.W.J. Prins, H. van Kempen, H. van Leuken, R.A. de Groot, W. Van Roy, and J. De Boeck, submitted, and *Spin-polarized tunneling with GaAs tips in scanning tunneling microscopy* by M.W.J. Prins, R. Jansen, and H. van Kempen, submitted.

Chapter 2

Photoelectrical properties of semiconductor tunneling tips*

Abstract

We describe a model as well as experiments on the electrical properties of a photoexcited tunnel junction between a metal and a semiconductor material, as is established in a scanning tunneling microscope (STM). The model treats the case that carrier transport is mediated by capture and relaxation in the semiconductor surface states. In the semiconductor, majority carrier transport is determined by thermionic emission over the Schottky barrier and subsequent surface recombination. By optical excitation an additional minority carrier current is generated. The voltage that develops on the semiconductor surface is determined by the balance between majority and minority carrier current in the semiconductor, and the current across the tunnel barrier. We present model calculations of the (non-planar) band-bending profile in the semiconductor, which indicate that the subsurface electric field operates as an electrical lens that can focus or defocus the current.

---

*The contents of this chapter were reported in *Photoampertc probes tn scanntng tunneltng mtcroscopy* by M.W.J. Prins, M.C.M.M. van der Wielen, R. Jansen, D.L. Abraham, and H. van Kempen, Appl. Phys. Lett. **64**, 1207-9 (1994), *Modulated photodetectton wtth semtconductor ttps tn a scanning tunneltng mtcroscope* by R.H.M. Groeneveld, M.W.J. Prins, and H. van Kempen, Surf. Sci. **331-333**, 1299 (1995), *Depletion field focustng tn semtconductors* by M.W.J. Prins and A.P. van Gelder, submitted, and in *Photoelectrtcal properttes of semtconductor ttps tn scanntng tunneltng mtcroscopy* by M.W.J. Prins, R. Jansen, R.H.M. Groeneveld, A.P. van Gelder, and H. van Kempen, submitted.

Measurements were performed with moderately doped GaAs tips and samples prepared by cleavage. Continuous as well as modulated photoexcitation was used. Relationships are determined between tunnel current, applied voltage, incident optical power and tip-sample distance. The experimental results are well described by the model that includes carrier capture in the semiconductor surface states. It is shown that the sensitivity of the tunnel current to small variations in optical power is determined by the ratio of the tunnel barrier conductance to the Schottky barrier conductance. The implications for near-field optical imaging and spin-polarized tunneling with semiconductor tips are discussed.

2.1   Introduction

Since its invention the scanning tunneling microscope (STM) [1] has been used for studies on semiconductor materials. Initially these studies were mainly concerned with the determination of the atomic arrangement at semiconductor surfaces, but soon thereafter the spectroscopic capabilities of STM were applied in order to reveal information on the semiconductor energy bands (e.g. [2]). From these investigations it appeared that the current flow through the semiconductor can seriously be affected by the STM-induced band-bending in the semiconductor subsurface region, most notably with semiconductors of low doping density [3].

When irradiating the semiconductor material with light, the produced electron-hole pairs are separated by the internal electric field of the band-bending region, in this way producing a surface photovoltage and the possibility to draw a current without applying an external voltage. Hence, the semiconductor band-bending profile influences the results of photoexcitation in a sensitive way. Photoexcited STM studies have been conducted with the semiconductor material as the sample (e.g. [4]), but more recently also as a tip material photoexcited semiconductors have been subjected to investigation [5]–[7]. These tips hold special attraction with regard to near-field optical imaging [8] and as sources of optically oriented spin-polarized electrons [9, 10] (a detailed analysis of these applications is given in Chapters 3 and 4 of this thesis).

In this Chapter we intend to develop a thorough understanding of the current transport properties of photoexcited semiconductor materials in STM. The outline is as follows. First we present a model on electrical transport in a photoexcited metal-semiconductor STM junction for continuous as well as modulated irradiation. The model includes the influence of surface states on the semiconductor surface. Thereafter we show experimental data taken with moderately doped GaAs ($\sim 10^{23}$ m^{-3}) under ambient conditions. We present results on the relationship between tunnel current, applied voltage, incident power, tip-sample distance, and sensitivity to small variations in light power. The results are compared with our model calculations. Finally we draw conclusions on the internal transport mechanisms in our junctions, and discuss the consequences for the usage of optically excited semiconductor tips in STM.

2.2   Electro-optical model

For more than a century the electrical properties of metal-insulator-semiconductor junctions have been investigated in view of their rectifying behavior and photonic applications (for excellent textbooks see [11]–[13]). These investigations were mainly concerned with solid-state junctions having a planar geometry. Model calculations on semiconductor devices are complicated by the fact that electrostatic effects (band-bending) and carrier transport (electron distribution function, electrochemical potential) are strongly coupled. In addition, transport of majority as well as minority carriers has to be considered. In order for the calculations to be tractable, usually important assumptions are made. In devices with a very thin insulating layer that is of negligible resistance, one can assume that the semiconductor surface is in equilibrium with the metallic electrode. When the insulating layer strongly inhibits the current flow, one may assume that the semiconductor surface is in equilibrium with the semiconductor bulk. In an STM the conductance of the tunnel junction is an adjustable parameter; often we cannot use one of the above limiting cases, and a more general treatment is required.

We will present a model for current flow in a photoexcited metal-semiconductor tunnel junction, where now the surface electrochemical potential is a free parameter. The main assumption underlying this model is that the current flows via the surface states on the semiconductor surface, instead of directly from the metal into the semiconductor conduction or valence band. The incorporation of surface states into a model description is particularly important when considering semiconductor tips, because at the tip apex surface states are present due to the strongly reduced crystallographic symmetry (so even in a well-controlled environment). Another important consideration stems from the fact that in an STM the dimensions of the tunnel barrier are far smaller than the typical depth of the band-bending region in the semiconductor. Due to this fact, the profile of the band-bending region will strongly deviate from planar symmetry. We will present calculations of the band-bending region in a semiconductor material, for the case that a tunnel junction is established on a planar semiconductor sample, as well as for the case of a semiconductor shaped as a tip. Finally we will present a quasi one-dimensional model for direct as well as displacement currents resulting from modulated photoexcitation.

2.2.1   Planar junction

In a metal-semiconductor tunnel junction, a metallic and a semiconducting material are separated by a tunnel barrier. Due to work function differences, surface charges and the application of voltage to the junction, a space charge layer (depletion layer) is generally formed in the semiconductor subsurface region. Hence we are confronted with a serial arrangement of two barriers: a tunnel barrier and a so-called Schottky barrier. In Fig. 2.1 we have drawn the one-dimensional energy diagram for a planar
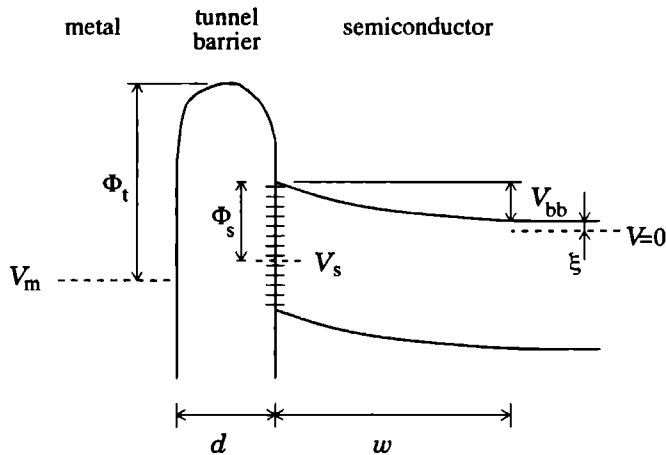
Figure 2.1: One-dimensional electronic energy diagram of a tunnel junction between a metal and a semiconductor. Indicated are: the tunnel barrier height (Φ_t), the Schottky barrier height (Φ_s), the band-bending voltage (V_{bb}), the difference between the Fermi level and majority carrier band-edge in the semiconductor bulk (ξ), the voltage applied between the metal and the semiconductor bulk (V_m), the semiconductor surface electrochemical potential (V_s). Along the vertical axis, the parameters are defined in volts. Horizontally are indicated: the metal-to-semiconductor separation (d), and the depth of the band-bending region (w). The picture is not on scale, because in general w is more than an order of magnitude larger than d.

tunnel junction with an n-type semiconductor. Indicated are the conduction and valence band edges in the semiconductor bulk, the band-bending region in the semiconductor, the surface states on the semiconductor surface, the tunnel barrier, and the metallic counter electrode. The bulk of the semiconductor is at zero electrical potential, the metallic electrode at the externally applied voltage V_m. The so-called surface or interface states within the forbidden energy gap are caused by the reduced symmetry of a surface as compared with the bulk, or by a modified chemical composition at the surface. For example, under ambient conditions GaAs forms a non-crystalline native oxide with a high density of surface states and a thickness of about a nanometer [14]. At the semiconductor surface we have indicated the surface electrochemical potential V_s. This potential can properly be assigned if the surface carriers are in thermal equilibrium. Because currents are flowing in the junction, strictly speaking this assumption is invalid. But since the processes of carrier capture and relaxation are generally very efficient at surfaces with surface states [15], we presume that the occupancy of the surface states obeys the Fermi-Dirac distribution. As can be seen

from the figure, the total band-bending in the space charge region is given by:

$$V_{bb} = \Phi_s - V_s - \xi ,\tag{2.1}$$

where Φ_s is the electrostatic Schottky barrier height (in volts*), and ξ is the difference between the Fermi level and the majority carrier band-edge in the semiconductor bulk. Φ_s is defined as the difference between the surface quasi-Fermi level and the position of the majority carrier band-edge at the semiconductor surface. In the following, we will assume that $|V_{bb}| \gg k_B T/e$ (25 mV at room temperature), and that the surface quasi-Fermi level remains between the conduction and valence band-edges at the surface.

Schottky majority carrier flow. Concerning majority carrier transport through the Schottky barrier, we will limit the model to the case where the dominant transport mechanism is given by thermally assisted emission of majority carriers over the barrier and subsequent recombination at the surface (the notions of majority and minority carriers refer to the carrier types as encountered in the semiconductor bulk). For high-mobility semiconductors this is not a very strong limitation. For example, at room temperature majority carrier transport in GaAs Schottky barriers is dominated by this so-called thermionic emission at doping densities of order $10^{23}\,\mathrm{m}^{-3}$ or lower. Following the thermionic emission theory, the density of current J_s flowing from the semiconductor surface to the bulk is given by [11]–[13]:

$$J_s = J_0 \left[\exp(\beta V_s) - 1 \right] , \qquad J_0 \equiv qNv_r \exp(-\beta \Phi_s) ,\tag{2.2}$$

where J_0 is the saturation current density, N is the semiconductor doping density, v_r is the effective recombination velocity at the potential energy maximum of the barrier, and $\beta = q/k_B T$. Here k_B is the Boltzmann constant, and T is the temperature. The parameter q equals $+e$ if the energy bands are bending upward toward the surface (as in Fig. 2.1) and $-e$ if the bands are bending downward, where e is the absolute magnitude of the electronic charge. In most n-type semiconductors the energy bands are bending upward toward the surface, such that $\Phi_s > 0$, $\xi > 0$ and $q = +e$; in most p-type materials the bands are bending downward and these three parameters are negative. The exponential factors in Eq.(2.2) cause the well-known rectifying current-voltage characteristic of a Schottky diode: if $\beta V_s > 0$ the band-bending magnitude is decreased and the Schottky barrier is operated in forward bias, whereas if $\beta V_s < 0$ the band-bending is increased and the diode is reversely biased. In case the actual process of thermionic emission is limiting the majority carrier transport (as in metal-capped Schottky diodes without a tunnel barrier), the effective recombination velocity is given by $A^{**} T^2 / [eN]$, where A^{**} is the modified Richardson constant [11].

---

*We define all barrier heights in volts, as is done in most papers on Schottky barrier theory (e.g. [11, 13]).

For example, in a metal-GaAs Schottky diode of $10^{23}\,\mathrm{m}^{-3}$ doping density, the effective recombination velocity is of order $10^7\,\mathrm{ms}^{-1}$. At free or oxidized semiconductor surfaces the recombination is generally less efficient, implying that surface recombination instead of thermionic emission limits the current flow. For example, in the native oxide on GaAs, the surface recombination velocity is of order $10^5\,\mathrm{ms}^{-1}$ [15]. Finally, Schottky barrier characteristics can deviate from the predictions of the thermionic emission theory due to the importance of other transport mechanisms, for example thermally assisted field emission or tunneling through the barrier. These transport mechanisms can be incorporated by adopting a slightly modified thermionic emission equation [13]:

$$ J_s = J_0 \exp(\beta V_s/n)\left[1 - \exp(-\beta V_s)\right] , \tag{2.3} $$

where n is the ideality factor [16]. With $n=1$ we recover Eq.(2.2); with $n>1$ the Schottky diode rectification is diminished. This formula determines the potential V_s required to draw a current through the Schottky barrier. As we will see later, V_s can have an appreciable value when using typical STM currents.

As pointed out in the previous equations, the majority carrier current through the Schottky barrier depends on the Schottky barrier height (Φ_s) via the formula for J_0. In case of a limited density of surface states, the barrier height is not constant due to capacitive interactions. To first order in V_m and V_s, the Schottky barrier height is easily calculated to be given by:

$$ \Phi_s = \Phi_s^0 - \frac{\tilde{C}_t[V_m - V_s] - \tilde{C}_s V_s}{\tilde{C}_t + \tilde{C}_s + e^2 D_{ss}} \equiv \Phi_s^0 - \gamma_t[V_m - V_s] + \gamma_s V_s , \quad 0 \le \gamma_{t,s} \le 1 \tag{2.4} $$

where Φ_s^0 is the barrier height in the equilibrium state (when $V_m=V_s=0$), $\tilde{C}_t$ is the tunnel barrier capacitance per unit area, $\tilde{C}_s$ is the Schottky barrier capacitance per unit area, and D_{ss} is the density of surface states (units $\mathrm{m}^{-2}\mathrm{J}^{-1}$) [17]. The tilde (˜) denotes that the capacitances are defined per unit area. The γ-factors are defined as: $\gamma_t \equiv \tilde{C}_t/[\tilde{C}_t+\tilde{C}_s+e^2 D_{ss}]$, and $\gamma_s \equiv \tilde{C}_s/[\tilde{C}_t+\tilde{C}_s+e^2 D_{ss}]$. Higher order terms to Eq.(2.4) result from the fact that $\tilde{C}_s$ and D_{ss} are not truly constant [18]. Eq.(2.4) tells us how at the surface the position of the majority carrier band-edge shifts with respect to the surface quasi-Fermi level, in response to the drop of electrochemical potential across the tunnel barrier (weighted by the factor γ_t) and in response to the potential drop across the Schottky barrier (weighted by the factor γ_s). The surface Fermi level is said to be pinned if γ_t and γ_s are approximately zero, i.e. in case of a high density of surface states. Combining Eqs.(2.1) and (2.4), the expression for the total band-bending becomes:

$$ V_{bb} = V_{bb}^0 - \gamma_t V_m - [1 - \gamma_t - \gamma_s] V_s \quad \text{with} \quad V_{bb}^0 = \Phi_s^0 - \xi . \tag{2.5} $$

The first term (V_{bb}^0) represents the band-bending in the equilibrium state. The second term describes the dependence of the band-bending on the external bias (V_m). In

case of a limited density of surface states, the semiconductor subsurface region is not completely shielded from the metal, such that the applied bias influences the band-bending in the semiconductor by a capacitive coupling (e.g. [3, 18, 19]). The third term takes account of the band-bending caused by the drop of electrochemical potential across the Schottky barrier (V_s), that is non-zero only in case of current flow in the semiconductor. The prefactor $[1-\gamma_t-\gamma_s]$ equals zero if there are no surface states $(D_{ss}=0)$, because in that case no charge is induced at the semiconductor surface. In order to determine the importance of these effects in our experiment, we need to assess the values of the weight factors γ_t and γ_s, that are a function of $\tilde{C}_s$, $\tilde{C}_t$, and D_{ss}. The capacitance of a Schottky barrier is associated with the modification of the depth of the space charge region upon change of the band-bending. In the depletion approximation (assuming a constant density of space charge eN) the capacitance per unit area is [11]–[13]:

$$\tilde{C}_s = \epsilon_0\epsilon_s/w , \qquad w = \sqrt{2\epsilon_0\epsilon_s V_{bb}/eN} , \qquad (2.6)$$

where w is the depth of the depletion region. In our experiments w ranges from 50 to 100 nm, so that (with $\epsilon_s=13$) $\tilde{C}_s$ ranges between 1 and 2×10^{-3} Fm^{-2}. For $\tilde{C}_t$ we can use the planar capacitor formula $\tilde{C}_t=\epsilon_0\epsilon_t/d$, where d is the separation between the metal and the semiconductor surface. For a vacuum tunnel barrier $(\epsilon_t=1)$ with $d=1$ nm, $\tilde{C}_t\simeq9\times10^{-3}$ Fm^{-2}. Finally, for oxidized GaAs the density of surface states (D_{ss}) ranges between 10^{36} and 10^{37} m^{-2}J^{-1} [11, 14]. From the above values, we estimate γ_t to range between 0.05 and 0.3, and find that γ_s is nearly an order of magnitude smaller than γ_t in our experimental situation. The γ-factors are rather small due to the high density of surface states present in the native oxide on GaAs. With the estimated γ-factors we conclude that in our experiments the band-bending in the semiconductor (cf. Eq. 2.5) is most strongly affected by the surface electrochemical potential, and is to a lesser extent sensitive to the potential of the metallic electrode.

Photoexcited minority carrier flow. Electron-hole pairs can be generated in the semiconductor material by irradiation with photons of energy higher than the band-gap. From the bulk of the semiconductor the carriers can reach the space charge region by diffusion. In the space charge region the minority carriers are swept toward the surface by the internal electric field [20], creating a photocarrier current from the semiconductor surface toward the bulk of size J_p per unit area. J_p is determined by many parameters, such as the incident light power P, the fraction of the light power that is absorbed in the semiconductor f_{abs} $(0\le f_{abs}\le1)$, and the extent to which the processes of minority carrier diffusion and drift are effective in collecting photocarriers at the semiconductor surface. This collection efficiency η_c $(0\le\eta_c\le1)$ depends on the absorption depth of the light relative to the bulk diffusion length and the depth of the space charge region. Solving the diffusion equation in case of planar symmetry

yields (e.g. [21]):

$$\eta_c = 1 - \frac{\exp(-\alpha_{ph}w)}{\alpha_{ph}L_d + 1} , \tag{2.7}$$

where α_{ph} is the photon absorption coefficient, and L_d is the minority carrier diffusion length. The diffusion length is given by: $L_d = [k_B T/e\,\mu\tau]^{1/2}$, where μ is the minority carrier mobility and τ is the minority carrier lifetime [15]. In high-quality GaAs the electron and hole mobility are about 0.8 and 0.04 $m^2V^{-1}s^{-1}$ respectively. The minority carrier lifetime depends on the majority carrier density (so on doping density and temperature) and on the material quality. At room temperature the minority carrier lifetime is a few nanoseconds in moderately doped GaAs [15], so the diffusion length ranges between one and a few micrometers. For photons of 633 nm wavelength $\alpha_{ph} = 4 \times 10^6$ m^{-1}, i.e. the optical penetration depth is 250 nm [22]. In other words, η_c is close to unity, and is modified by less than 4% when w increases from 50 to 100 nm. Hence we assume η_c to be constant for our experiment. This leads to the following equation for the photocurrent density flowing from the semiconductor surface toward the bulk:

$$J_p = -f_{abs}\eta_q\eta_c \frac{qP}{E_{ph}A_l} , \tag{2.8}$$

where η_q is the quantum efficiency of conversion of photons to electron-hole pairs ($0 \le \eta_q \le 1$), E_{ph} is the energy per photon, and A_l is the illuminated area. In our experiments the light intensity P/A_l ranges between zero and 10^6 Wm^{-2}. The total efficiency $\eta_q\eta_c$ can be close to unity for many semiconductor materials [23]. As we have seen, the space charge region in the semiconductor represents a barrier for majority carrier transport (J_s). On the other hand it constitutes an accelerating field for photoexcited minority carriers (J_p). Note that the sign of J_p is fixed by the sign of q, i.e. by the direction of the band-bending. It is interesting to estimate the excess minority carrier concentration at the surface (N_{sr}) that is associated with the surface recombination current due to photoexcited carriers. Given the surface recombination velocity v_{sr}, the density of surface recombination current becomes $J_{sr} \simeq e v_{sr} N_{sr}$. In our experiments the maximum photocurrent density is of order $10^6 Am^{-2}$. Using $v_{sr} = 10^5$ ms^{-1}, we find that $N_{sr} \le 10^{20}$ m^{-3}. This carrier concentration is negligible compared to the semiconductor doping density in our experiments ($\sim 10^{23}$ m^{-3}), and also too small to cause any significant minority carrier diffusion from the surface back into the bulk.

Tunneling current. The current across the tunnel barrier depends on the tunnel barrier shape, and on the electronic structure of the metal and of the semiconductor surface. Since these properties are not known in detail, we adopt the following simple description. The most characteristic property of a tunnel barrier is that the tunnel current has an exponential dependence on electrode separation. If the voltage drop across the tunnel barrier ($V_m - V_s$) is far smaller than the tunnel barrier height, the

tunneling current density (J_t) becomes [24]:

$$J_t \propto \exp(-2\kappa d)\,[V_m - V_s]\,, \qquad \kappa = [\,2m_e e\hat{\Phi}_t/\hbar^2\,]^{1/2}\,, \tag{2.9}$$

where m_e is the electron mass, and d is the electrode separation; in an STM d is of the order of one nm [25]. $\hat{\Phi}_t$ is the so-called apparent barrier height, that equals the barrier height (Φ_t) in case of a tunnel barrier with a rectangular shape [24]. Under ambient conditions, the apparent barrier height is generally lower than one volt due to surface contamination [24]. In our experiments the voltage drop ($V_m - V_s$) is also of the order of one volt, which gives rise to nonlinear current-voltage characteristics. In our model description this can be accounted for by adding a cubic term to the voltage dependence of the current [26].

The above description is valid if the surface electronic structures of both the metal and the semiconductor are not strongly dependent on the energy. With regard to the semiconductor, this translates into the requirement that the tunneling occurs from a continuous distribution of surface states, rather than from the semiconductor conduction or valence band. By a simple argument we can estimate whether this requirement is fulfilled. The probability of carrier capture in surface states is given by $\sigma_{cap}N_{cap}$, where σ_{cap} is the capture cross section and N_{cap} is the density of active surface states. For the GaAs native oxide $N_{cap} \simeq 10^{17}\text{-}10^{18}\,\text{m}^{-2}$ [11, 14] and $\sigma_{cap} \simeq 10^{-19}\text{-}10^{-18}\,\text{m}^2$ [27], giving a capture probability between 0.01 and unity. This is several orders of magnitude higher than the carrier transmission probability through a typical tunnel barrier [25]; thus we may assume that the tunnel current flows through the surface states instead of directly from the semiconductor conduction and valence bands into the metallic electrode (this issue is addressed more rigorously in Ref. [28]).

Let us consider the special case that $J_t = 0$ because $V_m = V_s$. At that point V_m is equal to the open-circuit voltage or so-called surface photovoltage (SPV), which is determined by the balance of majority and minority carrier current in the semiconductor: $J_s + J_p = 0$. Using Eq.(2.3), (2.4), and $\beta V_s \gg 1$ we find:

$$\text{SPV} = \frac{n}{1-\gamma_s n}\beta^{-1}\,\ln(-J_p/J_0^0)\,, \qquad J_0^0 \equiv qNv_r \exp(-\beta\Phi_s^0)\,, \tag{2.10}$$

Since J_p is proportional to the optical power P, a measurement of the SPV versus P can serve to determine the applicability of the presented model.

2.2.2   STM junction

The semiconductor surface electrostatic potential (i.e. the band-bending voltage gien in Eq. 2.5) is a function of (i) the electric field between the semiconductor and the metallic electrode, and (ii) the surface electrochemical potential. The first effect is only important in case of a limited density of surface states, because otherwise the
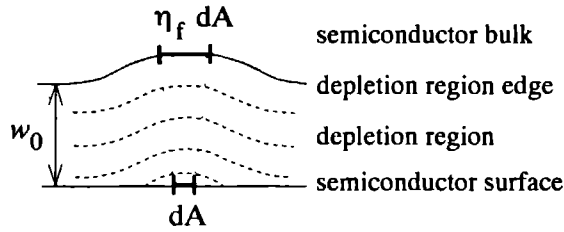
Figure 2.2: Schematic outline of the depletion region in a planar semicon-
ductor when a non-uniform reverse potential is applied to the surface. The
dashed lines represent equipotential lines. The depletion field focusing effi-
ciency (η_f) describes how, by following the electric field lines (represented by
the dotted lines), an infinitesimal area dA is mapped onto an area η_f dA at
the edge of the depletion region. In this case η_f is larger than unity, implying
that the field lines are focusing toward the semiconductor surface.

semiconductor subsurface region is completely shielded from the metal by the surface
states. (cf. the term with V_m in Eq. 2.5). The second mechanism is only effective in
case of a non-zero density of surface states, otherwise charge cannot be accomodated
at the semiconductor surface (cf. the term with V_s in Eq. 2.5). If we establish a metal-
semiconductor tunnel junction in an STM, (i) a non-uniform pattern of field lines is
set up between the tip and the sample, and (ii) a non-uniform surface electrochemical
potential is created. The latter results from the fact that the tunneling point rep-
resents a nanometer-sized injection point from which the current spreads out inside
the semiconductor material. In other words, due to the non-planar geometry of an
STM, the generated band-bending profile will deviate from one-dimensional symme-
try. A complete picture of the photoelectrical properties of such a system requires
simultaneously solving the three-dimensional electrostatic and transport equations.
The transport equation should include thermionic emission for the majority carriers,
and diffusion (outside the depletion region) and drift (inside the depletion region) for
the photoexcited minority carriers. Since this is unfeasible, in the following we will
develop a qualitative understanding of transport properties from electrostatic calcu-
lations only. The influence of the free carrier density associated with the tunneling
current is neglected [29].

Non-uniform band-bending in a planar semiconductor. Let us consider an STM junc-
tion between a metallic tip and a planar semiconductor surface at $z = 0$, where now
the non-uniform surface electrostatic potential is given by:

$$\Phi(x, y, 0) \;=\; F_0 + F_1(x, y) \;, \tag{2.11}$$

where F_0 is the constant potential of the unperturbed semiconductor surface, and F_1
represents the relative potential perturbation locally caused by the tunnel junction (for
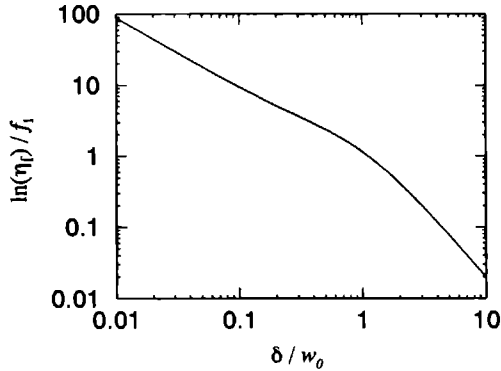
Figure 2.3: The natural logarithm of the depletion field focusing efficiency (η_f) divided by the relative magnitude of the potential perturbation (f_1), drawn as a function of the Gaussian width of the potential perturbation (δ). δ is normalized to the depth of the depletion region in an unperturbed planar semiconductor material (w_0). The focusing efficiency was deduced from a depletion field calculation in a *planar* semiconductor material. The calculation was performed to first order in the relative perturbation amplitude f_1 (see appendix A).

these calculations it is immaterial which mechanism is causing the non-uniform surface potential). With this boundary condition the subsurface depletion field has been calculated using perturbation theory, as is shown in appendix A. The calculations show that, with a locally applied reverse potential ($F_1/F_0 > 0$), the depth of the space charge region is locally increased and that the field lines tend to focus toward the spot where the local potential is applied (cf. Fig. 2.2). With a forward potential ($F_1/F_0 < 0$) the field lines defocus toward the spot where the potential is applied. In other words, the local potential modifies the depth of the space charge region and generates a *lateral* component of the electric field in the semiconductor subsurface region. Concerning carrier transport, this results in an effective transport section that depends on the band-bending profile. In case of photoexcited minority carriers – that are accelerated along the field lines in the space charge region – the effective section is increased (decreased) with a locally increased (decreased) band-bending. As such, the space charge field operates like an electrical lens with a variable diameter and focal length. Also the majority carrier transport is sensitive to the shape of the band-bending profile: the effective section for majority carrier transport will be larger with a reverse than with a forward potential. This effect may also provide an explanation for the weak rectification of current-versus-voltage characteristics often observed in point

contacts on semiconductors [12].

In order to quantify the focusing properties of the depletion field, let us consider a potential perturbation of Gaussian shape:

$$F_1 = f_1 F_0 \exp(-r^2/\delta^2) , \quad r = [x^2 + y^2]^{1/2} , \tag{2.12}$$

where δ is the Gaussian width and f_1 is the relative amplitude. As explained in appendix A, we then calculate the minority carrier trajectories in the depletion field and deduce a so-called focusing efficiency η_f. This efficiency describes how, by following the field lines, an infinitesimal area dA at $\vec{r}=\vec{0}$ is mapped onto an area η_f dA at the edge of the depletion region (cf. Fig. 2.2). From the calculations it follows that η_f exponentially depends on the perturbation amplitude f_1; the results are summarized in Fig. 2.3. For $f_1 > 0$ (reverse potential) the efficiency is larger than unity (focusing of field lines), whereas for $f_1 < 0$ (forward potential) the efficiency is smaller than unity (defocusing of field lines). Note that an increase of w_0 results in a larger focusing in reverse bias operation, and results in a larger defocusing in forward bias operation.

In our experiments the depth of the unperturbed depletion region ranges between 50 and 100 nm. The magnitude of the Gaussian width (δ) follows from the exact mechanism causing the non-uniform surface potential. If it is the penetration of field lines from the metallic tip, δ is expected to be of the order of the tip radius. On the other hand, if the non-uniform surface electrochemical potential is the driving mechanism, δ will depend on the details of the current flow in the semiconductor subsurface region. When δ is larger than the depth of the unperturbed depletion region ($\delta \gg w_0$) the efficiency tends to unity, because in that limit the depletion field is nearly uniform. On the other hand, for a perturbation that is applied very locally ($\delta \ll w_0$) the depletion field profile is strongly non-planar, such that η_f deviates from unity. The focusing efficiency can attain very large values in case of a reverse bias potential and a small δ. Let us estimate a reasonable maximum for the focusing efficiency. A lower limit to δ is given by the fact that the electric field along the surface cannot exceed the dielectric breakdown field, which is close to 10^8 Vm^{-1} in GaAs [11]; taking a perturbation amplitude of 0.2 V, we find that δ is larger than 2 nm. Using $w_0 \simeq 100$ nm, the lower limit for the ratio δ/w_0 is 0.02. From Fig. 2.3 and taking $f_1 = 0.2$, we deduce that $\ln(\eta_f) \simeq 0.2 \times 30$, i.e. a maximum depletion field focusing efficiency (η_f) of 4×10^2.

Band-bending in a semiconductor tip. When the STM tip is of semiconductor material, its non-planar geometry results in a non-planar space charge field. This experimental geometry is modeled in our calculation of the depletion field by assuming a rotationally symmetric body with a constant surface potential (see appendix A). Fig. 2.4 shows the calculated results for a semiconductor material of spherical symmetry, and for a semiconductor tip shaped as a paraboloid. Fig. 2.4A depicts the depth of the depletion region as viewed along the symmetry axis (w), divided by the value for a planar semiconductor (w_0). As expected, the curves tend to unity for blunt tips
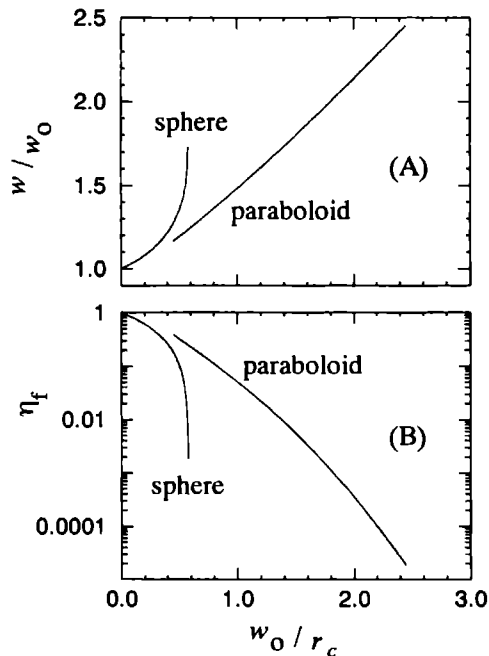
Figure 2.4: (A) The depth of the depletion region (w) and (B) the depletion field focusing efficiency (η_f), as a function of the inverse of the radius of curvature (r_c^{-1}) of a semiconductor material. Results are indicated for a semiconductor sphere with radius r_c, as well as for a paraboloid semiconductor tip with a radius of curvature r_c at the apex. w_0 is the depth of the depletion region in an unperturbed planar semiconductor material (w_0). In all cases a *constant surface potential* was assumed. The results for the sphere were derived from an exact calculation; the data for the paraboloid originate from an approximate solution (see appendix A).

($r_c^{-1} \to 0$). In a convexly shaped semiconductor (i.e. for finite r_c) the depth of the depletion region is larger than in a planar semiconductor. For the sphere the curve ends at $w = r_c = \sqrt{3}\, w_0$, for which the whole sphere has become depleted. The depth of the depletion region is not limited in a paraboloid semiconductor tip, because its shaft is of infinite length. For sharp paraboloid tips ($r_c < w_0$) the depth of the depletion region is proportional to the inverse of the radius of curvature. Fig. 2.4B shows the focusing efficiency for the sphere and the paraboloid. The focusing efficiency equals unity for blunt tips and rapidly decreases for sharper tips, indicating that the field lines are defocusing toward the surface. The strong similarity of the curves in Fig. 2.4A and 2.4B

stems from the fact that, for the considered range of parameters, the curvature of the equipotential lines in the depletion region closely resembles the curvature of the contour of the tip (see appendix A). In conclusion, when a tip-shaped semiconductor is compared to a planar semiconductor of the same material and with the same surface potential, the depletion region depth is larger and the focusing properties of the depletion field are biased toward defocusing.

Non-planar carrier flow. The previous calculations demonstrate that the profile of the band-bending region can strongly deviate from planar symmetry, when a metal-semiconductor tunnel junction is established in an STM. The driving mechanisms are the capacitive coupling between the tip and the sample, the non-uniform electrochemical potential at the semiconductor surface, and the shape of the tip. The most important conclusion is that we expect the flow of minority and majority carriers in the semiconductor to deviate from a one-dimensional picture. As an extension to our one-dimensional modeling of section 2.2.1, we therefore introduce an effective semiconductor transport section $A_s = \pi R_s^2$, where R_s is the effective section radius. Model calculations can now be based on the following equations: $I_p = A_s J_p$, and $I_t = I_s + I_p$, where I_t is the tunneling current, and I_s is the Schottky barrier majority carrier current. As an interesting example, let us consider the situation that no external bias is applied ($V_m = 0$). In that case the measured tunnel current can not be larger than the photoexcited minority carrier current density multiplied by the effective transport section: $|I_t| \leq A_s |J_p|$. Substituting this inequality into Eq.(2.8) gives:

$$A_s \geq \frac{|I_t| E_{ph} A_l}{f_{abs} \eta_q \eta_c |q| P} \quad \text{if } V_m = 0 \ . \tag{2.13}$$

In this way a measurent of the magnitude of the tunnel current at $V_m = 0$ yields a minimum collection area that has had to be effective in the semiconductor in order to generate the measured tunnel current. In the limit of very small tip-sample separation, the semiconductor surface potential drops to zero and the tunneling current equals the photocurrent. In other words, if $V_m = V_s = 0$, the above inequality becomes an equality, yielding the true value for the effective section in that particular limit.

In our experiments is not possible to determine the effective transport section for the majority carriers, because the Schottky barrier height (which determines J_s) is not *a priori* known. As a first approximation, for the majority carriers we use the same effective section as is used for the minority carriers: $I_s = A_s J_s$. In reality this assumption is not very accurate, since the two carrier types follow different transport mechanisms (thermionic emission for majority carriers, diffusion and drift for minority carriers). However, an error in the estimated majority carrier transport section of a factor of 10 for example, will limit the resulting error in the value of the Schottky barrier height (Φ_s) to $\sim \ln(10) k_B T / e \simeq 60 \, \text{mV}$, as we can read from Eq.(2.2).

2.2.3   Modulated photoexcitation

In the previous subsection we have described the considerations that led to a modified one-dimensional model for direct current transport between a metal and a semiconductor material in an STM. The major result is that, although the tunnel current is led through a nanometer-sized constriction, in the semiconductor the electrostatic and electrochemical potential are modified over an area that can be considerably larger. When modulated photoexcitation is applied, in addition to the direct currents also the displacement currents have to be analyzed. Direct currents are driven by a drop of electrochemical potential, whereas displacement currents are caused by a drop of electrostatic potential. Let us assume a time-dependent surface electrochemical potential of the form $V_s(t) = \text{Re}\{V_s + \Delta V_s \exp(j\omega t)\}$, while keeping V_m constant. As a result, through the Schottky barrier a modulation of direct current density of size $\tilde{G}_s \Delta V_s$ is generated, where $\tilde{G}_s = \partial J_s / \partial V_s$ is the differential conductance per unit area derived from Eqs.(2.2)-(2.4). In addition, a displacement current density is generated with magnitude $j\omega \tilde{C}_s [\Delta V_s - \Delta \Phi_s] = j\omega \tilde{C}_s [1 - \gamma_t - \gamma_s] \Delta V_s$, where we have used Eq.(2.4) with $\Delta V_m = 0$. The factor $[1 - \gamma_t - \gamma_s]$ ranges between zero ($D_{ss} = 0$) and unity ($D_{ss} \to \infty$). Thus, a limited density of surface states causes a reduction of the displacement current when expressed in terms of the electrochemical potential. In this particular case, the reduction can be taken into account by an effective capacitance of size $\tilde{C}_s [1 - \gamma_t - \gamma_s]$. Due to the high density of surface states in the native oxide on GaAs, the γ-factors are small in our experiments (cf. Eq. 2.6). Therefore the reduction factor is not of great concern. Omitting the reduction factor, we describe the total modulation of Schottky barrier current density by a complex admittance per unit area $\tilde{Y}_s = \tilde{G}_s + j\omega \tilde{C}_s$, such that $\Delta J_s = \tilde{Y}_s \Delta V_s$.

Fig. 2.5 shows the equivalent electrical circuit for time-dependent current transport in a metal-semiconductor STM junction, illuminated over an area $A_1 > A_s$. Quite arbitrarily the tip has been chosen to be the semiconductor material. Adopting a quasi one-dimensional model, two parallel current transport channels are distinguished. The first, called the constricted current channel, accounts for the current flow through the semiconductor effective section A_s and the tunnel barrier admittance Y_t. The second, named the wide channel, describes current flow through the remaining illuminated part of the semiconductor with section $[A_1 - A_s]$. The wide channel is capacitively coupled to the metallic electrode, described by a stray capacitance C_{str}. In the model $Y_{s,c} = A_s \tilde{Y}_s$ refers to the Schottky admittance in the constricted channel, and $Y_{s,w} = [A_1 - A_s] \tilde{Y}_s$ indicates the Schottky admittance in the wide channel. For completeness, also the external circuit admittance Y_{ex} has been incorporated in the figure. In the following analysis this parameter is omitted, since experimentally it was found to play a negligible role.

Let us consider a modulation of light intensity ΔP at frequency ω, which imposes a modulation onto the system by means of the following two electronic quantities: a modulation of the photocarrier current ΔJ_p according to Eq.(2.8), and a modulation
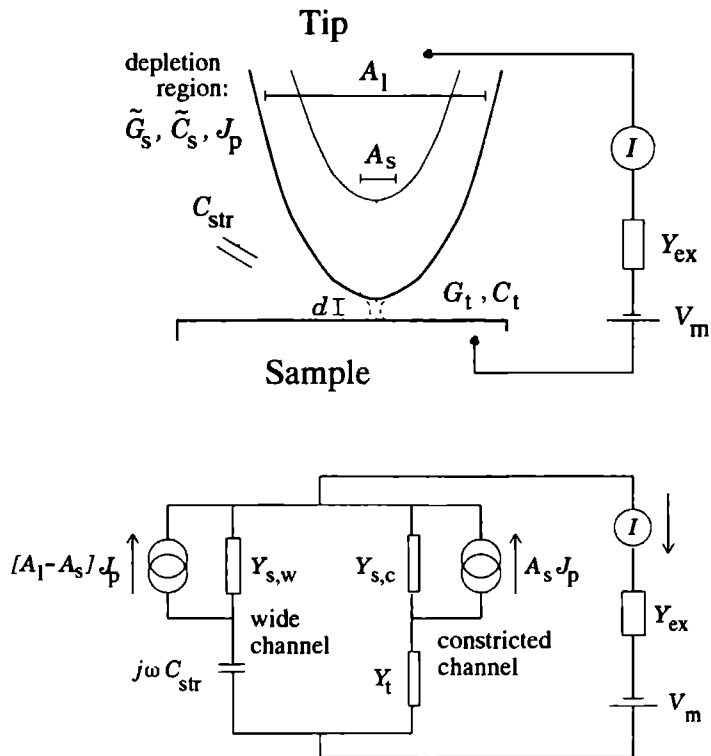
Figure 2.5: Electronic model (top) and equivalent circuit (bottom) of an illuminated metal-semiconductor STM junction, where in this case the semiconductor is shaped as a tip. A_l is the illuminated area of the tip. A_s is the section in the semiconductor subsurface region, that is effective for carrier transport toward the tunneling point. The dotted lines represent some relevant electric field lines. See the text for further explanation.

of the tunnel barrier conductance ΔG_t due to thermal expansion. Using the equivalent circuit, we calculate the modulation of voltage on the semiconductor surface in the constricted as well as in the wide channel, and deduce the total detectable current

modulation (see appendix B):

$$\Delta I = \underbrace{\frac{Y_t}{Y_t + Y_{s,c}} A_s \Delta J_p}_{\Delta I_{tp}} + \underbrace{\frac{Y_{s,c}}{Y_t + Y_{s,c}} [V_m - V_s] \Delta G_t}_{\Delta I_{tt}} + \underbrace{\frac{j\omega C_{str}}{j\omega C_{str} + Y_{s,w}} [A_l - A_s] \Delta J_p}_{\Delta I_C} .$$

$$(2.14)$$

The first term of ΔI is the modulation of constricted current due to photocurrent generation, and will be denoted by ΔI_{tp}. The second term is the modulation of constricted current caused by a modulation of the tunnel barrier conductance, abbreviated by ΔI_{tt}. The third term gives the displacement current through the stray capacitance C_{str} and is called ΔI_C. Note that in practical cases $\omega C_{str} \ll |Y_{s,w}|$.

The modulation of tunnel barrier conductance ΔG_t can be caused by thermal expansion of the junction. In this perspective, an important parameter is the distance of thermal diffusion within one modulation period, given by $d_{th} = [\kappa_{th}/\omega]^{1/2}$. Here κ_{th} is the thermal diffusivity, that equals approximately 5×10^{-5} m^{2}s^{-1} in GaAs. For the experimentally used modulation frequency of 84 kHz, we find a thermal diffusion length of 10μm. This is smaller than the typical spot size ($20\,\mu$m or larger). Therefore, we neglect lateral heat transport and consider the heat conduction to be one-dimensional. Then the modulation of tip-sample separation takes the following simple form [30]:

$$\Delta d = \frac{j\alpha_{th} f_{th} \Delta P}{\omega C_p A_l} ,$$

$$(2.15)$$

where α_{th} is the thermal expansion coefficient, f_{th} takes account of the fraction of incident optical power that is absorbed in the expanding body ($0 \leq f_{th} \leq 1$), and C_p is the heat capacity per unit volume. Both tip and sample can exhibit thermal expansion and hence cause a modulation of tip-sample separation. For example, using $\alpha_{th} = 10^{-5}$ K^{-1}, $f_{th} = 0.3$, $C_p = 10^6$ Jm^{-3}K^{-1}, and $\Delta P/A_l = 10^5$ Wm^{-2}, we estimate Δz to be less than 10^{-12} m at a modulation frequency of 84 kHz. Combining Eqs.(2.9) and (2.15), we find that the complex phase of $\Delta G_t/G_t$ is $-\pi/2$, implying that the conductance changes lag the optical power variations.

Finally, we note that in the outlined model the influence of a limited carrier relaxation time of the surface states is not considered. In surface states electron-hole recombination is generally very fast: in the native oxide on GaAs for example, recombination takes place on a subnanosecond time scale [15]. On the other hand, the cascade-like relaxation process of charges in the surface states can be rather slow if the density of surface states is low or if surface trap states are involved. The proper description by statistical mechanics requires solving the rate equations of the interactions between the surface states, the semiconductor conduction and valence band, and the metallic electrode [31]. A particular difficulty is that detailed knowledge of surface state properties is difficult to obtain. The incorporation of statistical parameters into our model remains to be investigated.
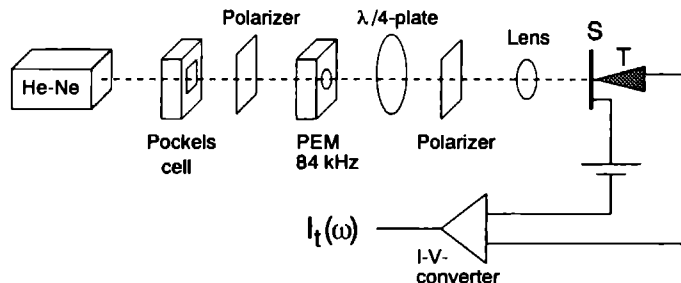
2.3 Experiment

Figure 2.6: Experimental arrangement. The STM-geometry is indicated for the usage of semiconductor tips (T) and a semitransparent sample (S).

The experiments were performed in an STM at ambient temperature and pressure, using GaAs samples as well as GaAs tips. Optical excitation was provided by a linearly polarized single-mode HeNe laser (633 nm). In order to be able to regulate the DC optical power and perform an optical power sweep, the beam was guided through a Pockels cell and polarizer, as depicted in Fig. 2.6. Subsequently, a photoelastic modulator (PEM), a $\lambda/4$ plate and an analyzer served to make a relative optical power modulation $\Delta P/P$ at 84 kHz. Finally the beam was focused into the STM junction by a 30-mm focal length objective. In the STM the spot diameter could be optimized with a relative uncertainty of 25%. Beam deflection due to the Pockels cell or the photoelastic modulator was verified to be negligible. In the STM junction the spot size amounted to a few tens of μm, yielding illumination intensities between zero and 10^6 Wm^{-2}. The estimated [32] local temperature rise was less than 1 K. Semiconductor tips were illuminated along the tip axis through a semitransparent sample (see Fig. 2.6), consisting of a 20-nm sputter-deposited Pt film on glass. The experiments on semiconductor samples were performed with sharply etched Pt-Ir tips, while illuminating the tunnel junction at about 50° from the sample normal. The GaAs tips and samples were prepared by cleaving polished and epitaxially grown (001) wafers along (110) and (1$\bar{1}$0) directions. The GaAs tips consist of a corner that is bounded by cleavage planes. Inspection by scanning electron microscopy and STM showed that cleavage produces well-defined corners with tip apex radii smaller than 100 nm. When used for topographical imaging in an STM, these tips yield a resolution close to a nanometer under ambient conditions [8, 10]. The GaAs was n-type (Si doped) or p-type (Zn doped), with doping densities ranging from 10^{22} m^{-3} to 5×10^{23} m^{-3}. The bandwidth of the STM constant-current regulation circuit was set between one and two kilohertz. The STM current was measured by a homemade current-to-voltage converter with a bandwidth of 100 kHz. The data have been corrected for the I-V

converter response, which at the highest frequencies could be determined with an accuracy of 10% and a phase uncertainty of about 10°. The signal was fed into a lock-in amplifier to allow for phase-sensitive detection of the current modulation.

2.4   Results and discussion

In this section we will present a comparison between experimental results and calculated curves. The latter were established by solving the current conservation rule $I_t = I_s + I_p$ with the equations presented in the previous sections. Except when stated otherwise, it was possible to fit the model calculations to the measurements with a certain range of values for the fit parameters. These values are summarized in Ref. [33]. Most experiments presented in this section were performed with semiconductor tips as well as with semiconductor samples. We could not detect any systematic differences between the photoelectrical properties of cleaved tips and planar samples of the same material; apparently, the Schottky barrier properties were more strongly determined by the voltages applied to the junction, than by the shape of the material. In our semiconductor materials the depletion region depth ranges between 50 and 100 nm, so for tips with at the apex a radius of curvature of that order, we do not expect to see differences with respect to a planar material (cf. section 2.2.2); in case of tips with a far smaller radius of curvature, a possible explanation for our experimental observation is that the cleaved GaAs tips have a very wide tip-angle (90 degrees), which suppresses the importance of the radius of curvature for the depletion field profile.

Fig. 2.7A shows measured static (so with the feedback-loop turned off) current versus voltage (I-V) characteristics at different setpoint values for current and voltage, corresponding to different values for the tip-to-sample separation. The indicated data are averages of 225 spectrocopic curves, taken with a GaAs tip in the absence of illumination. Panel (B1) shows calculated current versus voltage curves, where for the different curves only the tunnel barrier conductance was scaled. The top curve with repect to the bottom curve of panel (B1) involved an upscaling of the conductance by a factor of 25. This corresponds to an estimated change of the tip-to-sample separation of 0.5 nm (cf. Fig. 2.10).

At small positive voltages – when the Fermi level of the metallic electrode is positioned within the semiconductor bulk bandgap – we observe significant current flow, indicating that carrier flow mediated by surface states occurs. The observed rectification is a result of the pinning action of the surface states, which is well described by the model calculations. At 1 V reverse bias the current is smaller than 1 pA, indicating that at this point both the Schottky barrier conductance and the surface conductance are lower than $10^{-12}\,\Omega^{-1}$. Since in normal STM operation the junction conductance is of the order of $10^{-9}\,\Omega^{-1}$, this indicates that the surface conductance through the native oxide on GaAs is of negligible magnitude. Panel (B2) shows the calculated
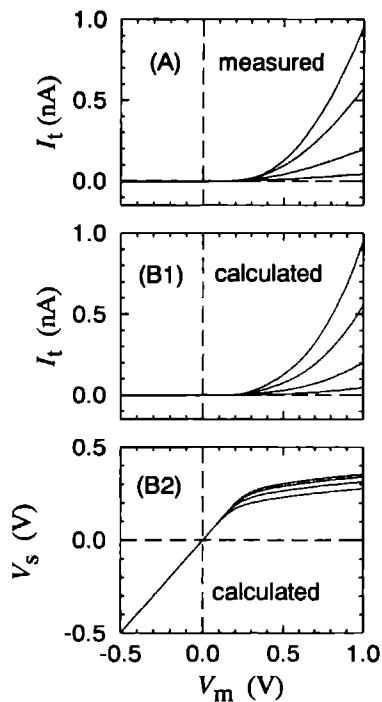
Figure 2.7: Measured (A) and calculated (B1) current versus voltage curves, for a non-illuminated GaAs tip (n-type, $2\times10^{23}\,\mathrm{m}^{-3}$ doping density). Panel (B2) shows the surface electrochemical potential V_s that follows from the calculated curves presented in (B1). The curves of panel (A) were measured starting from different setpoint values for current and voltage. The various calculated curves only differ in the magnitude of the tunnel barrier conductance. Fit parameters are summarized in Ref. [33].

surface electrochemical potential (V_s) that follows from the calculations. For $V_m < 0$ the Schottky barrier is reverse biased, such that the voltage drop across the Schottky barrier (V_s) equals the externally applied voltage (V_m). At an applied voltage higher than $\sim 0.2\,\mathrm{V}$, the Schottky barrier is sufficiently forward biased to be of comparable or higher conductance than the tunnel barrier, causing the voltage drop across the Schottky barrier to be only part of the applied voltage (V_m).

To further test the applicability of our model, we performed measurements of the surface photovoltage (SPV) versus optical power. As discussed with Eq.(2.10), the SPV
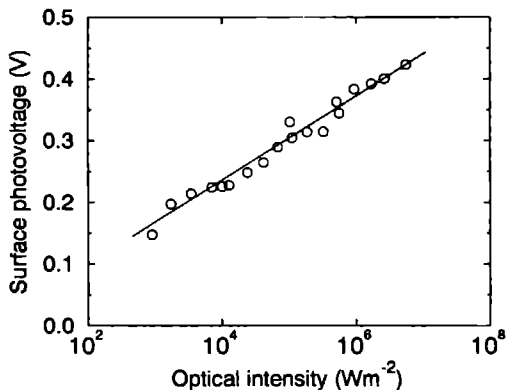
Figure 2.8: Measured (symbols) and calculated (line) surface photovoltage versus incident optical intensity for a GaAs sample (p-type, $10^{22}\,\mathrm{m}^{-3}$ doping density). Fit parameters are summarized in Ref. [33].

is determined by the zero-current point. Representative results are shown in Fig. 2.8, showing the expected logarithmic behavior. From the slope of the curve, for $n/[1-\gamma_s n]$ we deduce a value of 1.15 ± 0.10 (cf. Eq. 2.10). Actually, this value represents a measurement of n, because γ_s is very small in our system (see the estimates with Eq. 2.6). Because n is close to unity, we conclude that a model based on thermionic emission is indeed applicable. From the model calculation we deduce that the magnitude of the Schottky barrier height was 0.5 V for this p-type material. The barrier heights determined in this way [33] are in good agreement with the results of other measurement techniques [13]. Due to the higher barrier height of n-type material compared to p-type material, the SPV on the n-type material attains a reasonable value at substantially lower light intensities than needed for the p-type material.

In Fig. 2.9 we have depicted a set of I-V curves at a constant illumination intensity, for n-type GaAs of doping density $2\times10^{23}\,\mathrm{m}^{-3}$. The top panel (A) shows the measured data, the bottom panel (B) displays calculated curves for different magnitudes of the tunnel barrier conductance. With respect to the non-illuminated case (cf. Fig. 2.7), the most important differences are the appearance of a surface photovoltage, i.e. a shift of the zero-current point into the higher forward bias direction, and the observation of a considerable current at reverse bias. The SPV is the same for every tip-sample distance, within the experimental accuracy of about 10 mV (see also [5, 10]). If the photocarriers that are swept toward the semiconductor surface would not be captured in the surface states, but instead immediately be transmitted into the metallic electrode, the zero-current voltage would depend on the tunnel bar-
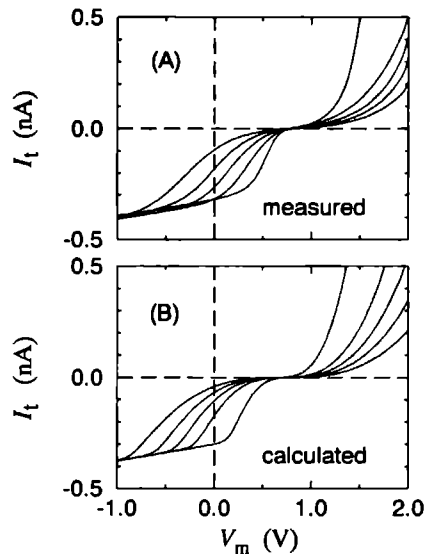
Figure 2.9: Measured (A) and calculated (B) current versus voltage curves for an illuminated GaAs tip (n-type, $2 \times 10^{23}\,\mathrm{m}^{-3}$ doping density). The curves of panel (A) were measured starting from different setpoint values for current and voltage. For the different curves of panel (B), only the magnitude of the tunnel barrier conductance was scaled. $P/A_1 = 10^3\,\mathrm{Wm}^{-2}$. Fit parameters are summarized in Ref. [33].

rier conductance in a very sensitive way. Since this is not observed, it proves that the carriers are captured in the surface states. In addition, we observe that the curves converge in the reverse bias direction ($V_m < 0$). The latter behavior is related to the limited amount of photoexcited carriers that can be collected at the tunnel junction. Qualitatively we can distinguish a photovoltaic and a photoamperic mode of operation of the semiconductor. The photovoltaic regime occurs in the vicinity of the SPV, when the tunnel current is smaller than the photocarrier current ($\sim 0.3\,\mathrm{nA}$); then the I-V curves can be described in terms of a nonlinear tunnel conductance connected to a voltage source with a high internal conductance. At reverse bias we enter the photoamperic regime; this corresponds to a highly loaded semiconductor, operating as a current source with a low internal conductance. In the absence of irradiation, this material does not allow to drawn current at reverse bias (cf. Fig. 2.7); according to Fig. 2.9 the maximum current at $V_m = 0$ amounts to approximately $0.3\,\mathrm{nA}$ at the specified light intensity. Using the equality of Eq.(2.13), we estimate the collection radius of photogenerated charge to be one μm. This is of the same order as the minor-
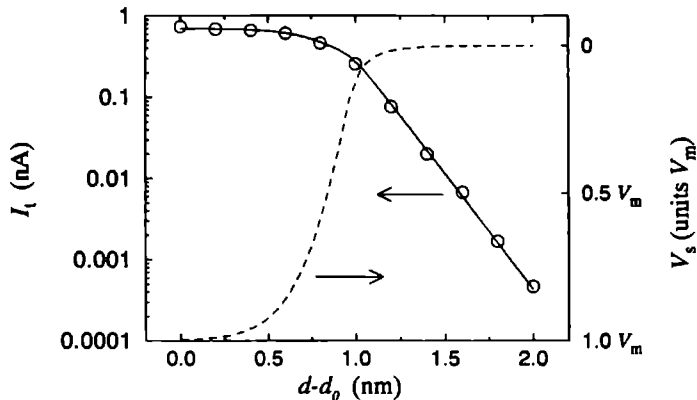
Figure 2.10: Tunnel current (left scale) and voltage drop across the Schottky barrier (right scale), as a function of the tip-sample separation (d) relative to the setpoint at $d=d_0$. For a non-illuminated GaAs tip (p-type, $5 \times 10^{23} \, \mathrm{m}^{-3}$ doping density). Symbols represent measured points, lines are calculated values. Constant applied voltage $V_m = 0.5 \, \mathrm{V}$. Fit parameters are summarized in Ref. [33].

ity carrier diffusion length in GaAs [15]. It is not surprising that carrier diffusion is of importance since the optical penetration depth ($0.25 \mu\mathrm{m}$) is larger than the depth of the band-bending region ($0.1 \mu\mathrm{m}$ at maximum). Note that the size of the saturation current significantly depends on the applied voltage. As was discussed with Eq.(2.7), the observed increase cannot be simply explained by an increase of the depth of the space charge region. As a possible explanation we invoke the focusing effect that becomes increasingly pronounced at reverse bias; to account for this effect, in the model calculation we have added a small linear voltage-dependence to the effective section A_s. In conclusion, the observed reverse bias current indicates that significant three-dimensional transport of minority carriers (focusing) occurs in the semiconductor subsurface region. The importance of minority carrier focusing by drift (inside the depletion region) versus focusing during diffusive transport (outside the depletion region) cannot be judged at present.

It was pointed out that an illuminated metal-semiconductor STM junction can be operated in two distinct regimes: the photovoltaic regime, when the Schottky barrier conductance is higher than that of the tunnel barrier; and the photoamperic regime, when the Schottky conductance is lower than that of the tunnel barrier. In the previous case (Fig. 2.9) the transition from one regime to the other is regulated by the bias voltage. Another way to establish the transition is by adjusting the tip-sample
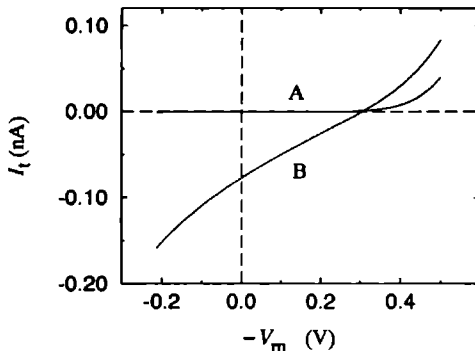
Figure 2.11: Current versus voltage curves without (A) and with (B) laser excitation at the same tip-sample separation, for a GaAs sample (p-type, $5 \times 10^{23}\,\mathrm{m}^{-3}$ doping density). These curves were composed by chopping the light at $4\,\mathrm{kHz}$. In the illuminated situation $P/A_1 = 10^5\,\mathrm{Wm}^{-2}$. Fit parameters are summarized in Ref. [33].

separation. Fig. 2.10 depicts a measurement of current versus tip-sample separation (relative scale) for a non-illuminated GaAs tip. By making reproducible topographic scans, it was verified that tip and sample were never in contact. The calculated curves for the tunnel current (left scale) and for the voltage drop across the Schottky barrier (right scale) are also indicated. At high tip-sample separation an exponential behavior of current versus distance is observed, in agreement with Eq.(2.9) [34]. Using that equation, from Fig. 2.10 we deduce for κ a value of $3.2\,\mathrm{nm}^{-1}$, which corresponds to an apparent tunnel barrier height ($\hat{\Phi}_t$) of $0.4\,\mathrm{V}$. These are reasonable values for a measurement under ambient conditions [24]. Upon closer approach, the current saturates when the tunneling conductance has become higher than the Schottky conductance; at that point the Schottky barrier voltage drop equals the externally applied voltage V_m, indicating that the Schottky barrier conductance has become the limiting factor for current conduction.

In a planar solid-state metal-semiconductor junction, the consequence of illumination is that an extra current contribution is added, with a sign independent of the bias voltage V_m: the absolute magnitude of the current increases in reverse bias and decreases at a forward bias higher than the SPV. However, in STM experiments with p-type GaAs of moderate or high doping, we have observed a very different behavior. An example is depicted in Fig. 2.11, showing I-V curves taken at the same tip-sample separation. At a forward bias higher than the SPV, upon illumination the current shows a clear increase, in contrast to the general behavior in planar devices. The estimated [35] increase of the tunnel barrier conductance due to thermal expansion

was less than 10%. By additionally measuring difference curves at high modulation frequencies (84 kHz), we verified that thermal expansion was not the reason for the observed crossing of the I-V curves.

Our calculations indicate that the direction of the band-bending was certainly not reversed by the applied forward bias. Hence, as was pointed out in section 2.2.1, in case of a forward bias potential on the semiconductor surface, J_s is of opposite sign compared to J_p. This means that in a forward biased planar junction, an increased illumination can not enlarge the total current density (J_s+J_p) flowing in the semiconductor, and as a result can not cause an increase of J_t. Qualitatively, the observed behavior can be explained by the fact that the effective section A_s depends on the band-bending profile. As we have discussed in section 2.2.2, in the space charge region the (de)focusing of field lines depends on the relative difference between the band-bending at the tunneling point and the band-bending away from the tunneling point (represented by the parameter f_1 in Eq. 2.12). Upon irradiating the semiconductor, there is an overall decrease of the depth of the band-bending region (w_0), which according to Fig. 2.3 gives a weaker defocusing in forward bias $(f_1<0)$. A weaker defocusing implies an increased effective section for charge transport through the Schottky barrier. Hence, when in forward bias the current is mainly determined by the flow of majority carriers, an increased effective section due to illumination gives an increase of the magnitude of the total current. In other words, the fact that curves (A) and (B) of Fig. 2.11 cross at a certain point, may be a consequence of the (de)focusing properties of the semiconductor band-bending region. At present we are unable to quantitatively model these effects, because the transport of majority carriers through a non-planar Schottky barrier has not yet been calculated.

Modulated photoexcitation. From the previous data we conclude that a semiconductor tunneling tip can be very sensitive to optical excitation, making these tips interesting as scanning local photodetectors [8] and as sources of optically oriented spin-polarized electrons [9, 10]. However, because an STM is normally operated in the constant-current mode, the frequency band between zero and about 2 kHz is used for stabilization of the tip-to-sample distance. Hence, additional signals have to be detected at frequencies higher than the bandwidth of the constant-current feedback system. In this perspective, we will study the response of a metal-semiconductor tunnel junction at a frequency of 84 kHz and compare the results to calculations based on the model described in section 2.2.3. The model calculations were made by solving the equivalent electrical circuit (cf. Fig. 2.5) for the constricted as well as for the wide channel, with the aid of an iterative computer code.

The sensitivity of the current to a modulated photoexcitation is depicted in Fig. 2.12 for p-type GaAs of $5\times10^{23}\,\mathrm{m}^{-3}$ doping density, and in Fig. 2.13 for n-type GaAs of $2\times10^{23}\,\mathrm{m}^{-3}$ doping density. The measurements were made by sweeping the
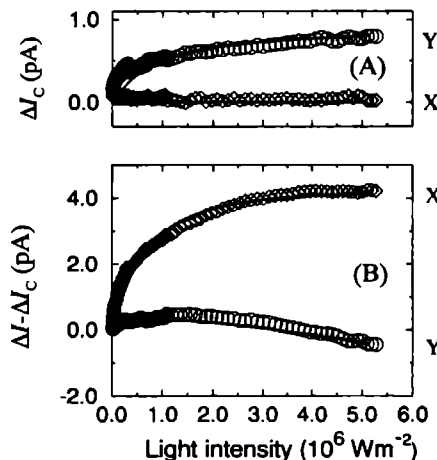
Figure 2.12: Measured (symbols) and calculated (lines) phase-sensitive current modulation (x=in-phase, y=out-of-phase) versus incident illumination intensity. The calculated curves are nearly obscured by the data. The top figure (A) shows the current modulation through the stray capacitance, measured while out-of-tunneling at a tip-sample separation of about $0.5\,\mu$m. The bottom figure (B) displays the current modulation while tunneling, corrected for the stray capacitance contribution. For a p-type GaAs tip of doping density $5 \times 10^{23}\,\text{m}^{-3}$. Fit parameters are summarized in Ref. [33]. Relative power modulation $\Delta P/P = 10\%$ at $84\,$kHz. Estimated uncertainty of current modulation is $0.2\,$pA. Set DC tunnel current $I = 0.5\,$nA; $V_\text{m} = 0.5\,$V.

DC optical power while keeping the constant-current feedback loop enabled. The relative modulation of incident optical power $\Delta P/P$ was constant during the sweep. The in-phase (x) and out-of-phase (y) current modulations were recorded with a lock-in amplifier. The top panels (A) show the signal detected when the tip was retracted from the sample by $\sim0.5\,\mu$m, i.e. a signal due to stray capacitive coupling between tip and sample only. The bottom panels (B) depict the current modulation measured in tunneling range, when the stray capacitance contribution has been subtracted.

Fig. 2.12A shows the measured stray capacitance signal when the tip was retracted from the sample by approximately $0.5\,\mu$m. The capacitive coupling can clearly be detected [36] and is well described by our model [37]. The model calculation yields a stray capacitance of $0.3\,$fF (the capacitance reduction factor of section 2.2.3 is neglected). When corrected for the stray capacitance signal, the measured signal while tunneling contains a photocarrier contribution (ΔI_tp) and a contribution due to modulation of the tunnel barrier conductance (ΔI_tt) by thermal expansion. As shown in
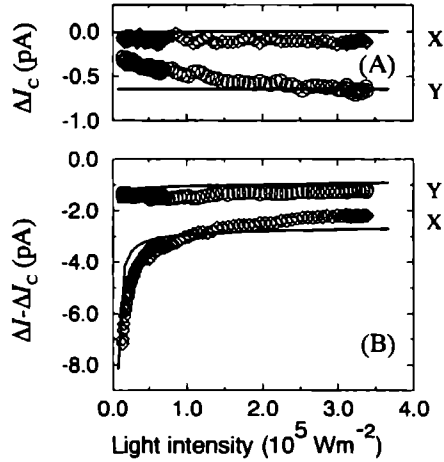
Figure 2.13: As Fig. 2.12, now for an n-type GaAs tip of $2 \times 10^{23}\,\mathrm{m}^{-3}$ doping density; $V_\mathrm{m} = 0$.

Fig. 2.12B, the combined signal contains an in-phase as well as an out-of-phase component (see [38]). The out-of-phase component has a contribution from ΔI_tp because Y_t is complex, and a contribution from ΔI_tt because ΔG_t (due to thermal expansion) is out-of-phase at $-\pi/2$. The model calculation takes account of the combined signal, yielding a tunnel barrier capacitance of 0.3 fF. This is the capacitance associated with the approach of the tip to the sample by about $0.5\,\mu\mathrm{m}$. For the relative tunnel barrier conductance modulation due to thermal expansion, the model calculation yields a value $[\Delta G_\mathrm{t}/G_\mathrm{t}]/\Delta P = 10\,\mathrm{W}^{-1}$. In this experiment the maximum value of ΔP was 0.16 mW. Using these values and Eq.(2.9) with $\kappa = 3.2\,\mathrm{nm}^{-1}$ (cf. Fig. 2.10), we calculate a corresponding modulation of tip-sample separation of $\Delta d = 0.2\,\mathrm{pm}$. This is close to the value that was estimated with Eq.(2.15). Furthermore, the size as well as the phase of the heating signal compare well with a similar measurement using a metallic tip and sample [7].

As depicted in Fig. 2.13, the data on modulated photoexcitation in n-type GaAs show a different behavior. This mainly originates from the fact that the Schottky barrier height is larger in n-type than in p-type material [13, 33]. As a consequence, the important changes in optical sensitivity occur at lower light intensities, where photothermal effects are still negligible. As shown in Fig. 2.13B, at high optical power a rather constant modulation signal is observed, in agreement with our model [39]. The signal phase is non-zero due to the tunnel barrier capacitance. The most striking feature comes in at low light power, when the modulation signal shows a rapid

increase. The increase is also observed if a reverse bias is applied to the junction. The reason is that the Schottky saturation current $I_0 = A_s J_0$ is very small for this material, far smaller than the tunnel current. As a result, the semiconductor surface voltage collapses and the tip-sample separation is reduced, when the size of the available photocurrent (I_p) approaches the magnitude of the tunnel current. At that point the photoamperic regime is approached; as expected, we observe that the tunnel current has a maximum sensitivity to variations of the optical intensity toward the photoamperic mode of operation (see also Ref. [6]). We were unable to make high-resolution topographic scans in the photoamperic mode of operation, most probably because in that regime the total tunnel current is rather insensitive to variations of the tip-sample distance. Finally, the model calculation for ΔI_C gives a signal of the right size and the right phase; the fact that the calculation does not explain the observed rather weak dependence on optical power remains to be investigated.

In conclusion, for p-type as well as for n-type GaAs tips (i.e. for material with respectively a low and with a high Schottky barrier height) of $\sim 10^{23}$ m^{-3} doping density, the response of the current to a modulation of optical power can be understood with the model outlined in section 2.2.3. The current is composed of signals due to photocarrier modulation, thermal expansion, and due to capacitive tip-sample coupling. For both materials, the signal due to photocarrier modulation saturates at high optical intensities. The sensitivity to optical power is highest for n-type GaAs close to the photoamperic mode of operation.

2.5   Summary and conclusions

From the theoretical estimations and a comparison between measurements and calculations, the following picture arises as to the photoelectrical properties of moderately doped GaAs in an ambient STM. First of all the semiconductor surface states play a crucial role. Not only do the surface states support current flow by strongly communicating with the semiconductor valence and conduction band, they are also effective in shielding the charge on the metallic electrode and in pinning the surface Fermi level. The current-voltage characteristics can be described by considering sequential transport through the serial arrangement of a tunnel and a Schottky barrier. The tunnel barrier is represented by a nonlinear conductance, whereas transport through the Schottky barrier can be described by thermionic emission of majority carriers. As a result, across the Schottky barrier an important drop of electrochemical potential may occur, especially in reverse bias operation. For a given semiconductor, the relative importance of the Schottky versus the tunnel barrier conductance can be tuned by changing the applied voltage or by adjusting the tip-to-sample separation. When optically exciting the semiconductor, an additional minority carrier current is generated in the semiconductor. The voltage that develops on the semiconductor surface

is determined by the balance between majority and minority carrier current in the semiconductor, and the current across the tunnel junction.

The heart of the photoelectrical properties of semiconductors in STM lies in the understanding of the carrier flow in the semiconductor subsurface region. The tunneling point represents a nanometer-sized constriction of current, but in the semiconductor subsurface region the current density distribution can have a considerably larger lateral extent. The effective section for majority and minority carrier transport in the semiconductor is determined by the band-bending profile and possible conduction along the surface. For the photoexcited minority carriers the effective collection radius is estimated by measuring the maximum tunnel current that can be drawn at a certain illumination intensity. This estimation yields a value of one μm for n-type GaAs and a somewhat lower value for p-type GaAs. Since the surface conductance was determined to be negligible, we attribute the measured photocarrier collection area to the non-planarity of the subsurface carrier flow. As we illustrated with electrostatic calculations, a locally applied reverse potential produces a band-bending profile that acts as a focusing lens for the collection of photoexcited minority carriers. According to our calculations, in the depletion region a focusing power of more than two orders of magnitude is possible. This effect can be enhanced by a focusing effect during the diffusive transport of carriers that are generated outside the depletion region.

The sensitivity of the tunnel current to a modulation of incident optical power was investigated. Good agreement was obtained between the experimental results and the model calculations. The appearance of a modulated surface photovoltage causes direct as well as displacement currents. Also a signal due to thermal expansion was present. Phase-sensitive detection allows for a separation of the different contributions.

To illustrate some consequences of our present understanding, we turn to the application of semiconductor tips for the detection of magnetic sample properties. Magnetic imaging can be achieved in two distinct ways, namely by magneto-optical near-field imaging [8] (see Chapter 3) and by spin-polarized tunneling due to optical spin-orientation [9, 10] (see Chapter 4). In magneto-optical imaging the semiconductor tip operates as a local photodetector that maps the polarization-dependent optical properties of a magnetic material. This implies that the main interest is directed toward a small collection volume for photocarriers and a high sensitivity to variations of the optical intensity. In principle the optical sensitivity of the tunnel current is highest for a material with a high Schottky barrier and a low doping density, operated in the photoamperic mode of operation (when the tunnel barrier conductance is higher than the Schottky barrier conductance). However, this mode of operation is not always convenient, because the tunnel current becomes rather insensitive to changes of the tip-sample separation, which can induce a loss of tunnel junction stability. The requirement of a small collection volume of photocarriers can be achieved by (i) a

reduction of the diffusion length (higher doping density, or a different semiconductor material), (ii) a reduction of the optical penetration depth to below the depth of the depletion region (radiation of shorter wavelength), or (iii) a reduction of the focusing power of the depletion field (forward bias operation, or a sharper tip). A possible reduction of the surface photovoltage and of the detectable photocarrier current can be compensated for by increasing the optical power. Special care will have to be taken to avoid signals due to thermal expansion to start dominating, for example by increasing the modulation frequencies; in turn this may yield a more pronounced contribution of displacement currents.

In a spin-polarized tunneling experiment the aim is to detect spin-polarized transmission through the tunnel barrier, which means that we should tune the junction to a high sensitivity for tunnel barrier transmission changes. Then the photovoltaic mode of operation is appropriate, for which the tunnel barrier conductance is lower than the Schottky conductance. Furthermore, it is of interest to obtain a low sensitivity of the tunnel current to variations of the optical power. This can be done by changing the externally applied voltage. Interestingly, for some materials we have observed a working point with the special feature that for a given applied voltage the tunnel current is insensitive to variations of the optical power (cf. Fig. 2.11).

In conclusion, the presented model gives a good description of the experimentally observed photoelectrical properties of moderately doped GaAs in an ambient STM. The model allows for clear predictions on the applicability of photoexcited semiconductor tips in STM. For future directions, in will be of interest to study the transition from a high to a low density of surface states, for example by preparing the semiconductor in an ultra-high vacuum environment, or by chemically treating the semiconductor surface [40, 41]. Furthermore, an improved understanding of the three-dimensional band-bending profile and the majority and minority carrier transport sections is needed. This issue can experimentally be addressed by studying the minority carrier collection area for materials of different doping density and diffusion length. These studies may also reveal the nature of the observed configurations where the tunnel current is insensitive to variations of the optical intensity. Finally, for high-frequency and time-resolved optical STM studies on semiconductors (e.g. [42]) it will be interesting to establish a statistical model of the electronic interactions between the semiconductor bands, the surface states, and the metallic counter electrode.

References

1. A review on STM can be found in: *Scanning tunneling microscopy I, II, and III*, edited by R. Wiesendanger and H.-J. Güntherodt, Springer series in surface

science vol. 20, 28, and 29 (Springer Verlag, Heidelberg, 1992/93).

2. R.M. Feenstra, Surf. Sci. **299/300**, 965 (1994).

3. R. Maboudian, K. Pond, V. Bressler-Hill, M. Wassermeier, P.M. Petroff, G.A.D. Briggs, and W.H. Weinberg, Surf. Sci. Lett. **275**, L662 (1992).

4. M. McEllistrem, G. Haase, D. Chen, and R.J. Hamers, Phys. Rev. Lett. **70**, 2471 (1993).

5. M.W.J. Prins, M.C.M.M. van der Wielen, R. Jansen, D.L. Abraham, and H. van Kempen, Appl. Phys. Lett. **64**, 1207 (1994).

6. M.W.J. Prins, M.C.M.M. van der Wielen, D.L. Abraham, H. van Kempen, and H.W. van Kesteren, IEEE Trans. Magn. **30**, 4491 (1994); M.C.M.M. van der Wielen, M.W.J. Prins, R. Jansen, D.L. Abraham, and H. van Kempen, in *Photons and local probes*, edited by O. Marti, NATO-ASI series (Elsevier, Amsterdam), accepted for publication.

7. R.H.M. Groeneveld, M.W.J. Prins, and H. van Kempen, Surf. Sci. **331-333**, 1299 (1995).

8. M.W.J. Prins, R.H.M. Groeneveld, D.L. Abraham, H. van Kempen, and H.W. van Kesteren, Appl. Phys. Lett. **66**, 1141 (1995).

9. M.W.J. Prins, D.L. Abraham and H. van Kempen, J. Magn. Magn. Mat. **121**, 152 (1993); Surf. Sci. **287/288**, 750 (1993).

10. R. Jansen, M.C.M.M. van der Wielen, M.W.J. Prins, D.L. Abraham and H. van Kempen, J. Vac. Sci. Technol. **B12**, 2133 (1994).

11. M.S. Sze, *Physics of Semiconductor Devices* (Wiley Int., New York, 1981).

12. H.K. Henisch, *Semiconductor contacts*, Int. series of monographs on physics No. 70 (Clarendon Press, Oxford, 1984).

13. E.H. Rhoderick and R.H. Williams, *Metal-Semiconductor Contacts*, Monographs in electrical and electronic engineering No. 19 (Clarendon, Oxford, 1988).

14. H.H. Wieder, J. Vac. Sci. Technol. **17**, 1009 (1980), and other contributions in this issue.

15. R.K. Ahrenkiel, chapter 2 in *Minority carriers in III-V semiconductors: physics and applications*, edited by R.K. Ahrenkiel and M.S. Lundstrom, Semiconductors and semimetals vol. 39 (Academic Press, San Diego, 1993), p. 39.

16. We will call n the ideality factor (as in [13]), although some authors prefer to call n the non-ideality factor [12].

17. In a similar way the dependence of the equilibrium-state barrier height (Φ_s^0) on the electrode workfunction difference can be described. This is omitted for clarity.

18. For the case that the density of surface states equals zero, the exact barrier height is calculated in: W.J. Kaiser, L.D. Bell, M.H. Hecht, and F.J. Grunthaner, J. Vac. Sci. Technol. **A6**, 519 (1988).

19. Z.-H. Huang, M. Weimer, and R.E. Allen, Phys. Rev. **B48**, 15068 (1993).

20. In GaAs the minority carrier velocity in the space charge field is scattering-limited at a value close to $v \simeq 10^5 \, \mathrm{ms}^{-1}$ [11]. Thus the sweep-out time is $\tau_s \simeq w/v \simeq 0.5 \, \mathrm{ps}$ when using $w = 50 \, \mathrm{nm}$. Since the recombination lifetime in GaAs is orders of

magnitude larger than a picosecond, recombination losses in the space charge region can be neglected.

21. C.M. Aldao, A. Palermo and J.H. Weaver, J. Vac. Sci. Technol. A **10**, 493 (1992).

22. D.E. Aspnes and A.A. Studna, Phys. Rev. B**27**, 985 (1983).

23. In comparison, for most materials the yield for electron photoemission is lower than 10^{-2} for photon energies in the visible region [W.E. Spicer, chapter 10 in *Optical properties of solids*, edited by F. Abelès (North-Holland, Amsterdam, 1972)].

24. C.J. Chen, *Introduction to scanning tunneling microscopy*, Oxford series in optical and imaging sciences vol. 4 (Oxford University Press, New York, 1993).

25. In an STM, the absolute value of the tip-to-sample separation (d) can be estimated as follows. Upon point-contact, the conductance is of the order of the quantum conductance ($2e^2/h \simeq 8 \times 10^{-5}\,\Omega^{-1}$); in an STM experiment, the tunnel barrier conductance ranges between 10^{-8} and $10^{-10}\,\Omega^{-1}$. Comparing the tunneling junction with the point-contact, we deduce that the relative tunnel barrier transmission ranges between 10^{-4} and 10^{-6}. This relative transmission probability is roughly determined by the factor $\exp(-2\kappa d)$ of Eq.(2.9), where $\kappa = 3.6 \pm 0.4\,\text{nm}^{-1}$ is a typical value under ambient conditions (cf. Fig. 2.10). With the mentioned range of the experimental transmission probability, we find a tip-to-sample separation of $d = 1.6 \pm 0.5\,\text{nm}$.

26. J.G. Simmons, J. Appl. Phys. **34**, 1793 (1963).

27. C.H. Henry and D.V. Lang, Phys. Rev. B**15**, 989 (1977).

28. H.C. Card, Solid-St. Electr. **18**, 881 (1975).

29. The free carrier density inside the semiconductor, caused by the tunneling current, can be estimated as follows. Assuming radial current flow inside the semiconductor close to the tunneling point, at a distance r into the semiconductor the current density is of the order of $J_s \simeq 1\text{nA}/r^2$. In case this current density is furnished by surface recombination, at the semiconductor surface the excess carrier concentration becomes $N_{sr} = J_s/[ev_{sr}] \simeq 5 \times 10^4/r^2$. Since in our experiments the doping density is about $10^{23}\,\text{m}^{-3}$, we deduce that the excess carrier concentration will not affect the band-bending profile at a distance of more than 2 nm from the tunneling point.

30. S. Grafström, J. Kowalski, R. Neumann, O. Probst, and M. Wörtge, J. Vac. Sci. Technol. B **9**, 568 (1991).

31. An example of a statistical description of surface states in a non-illuminated Schottky diode can be found in: J. Werner, K. Ploog, and H.J. Queisser, Phys. Rev. Lett. **57**, 1080 (1986).

32. Assuming radial heat conduction through a cone with solid angle Ω, we can estimate the temperature rise at the illuminated spot to be $\Delta T \simeq P/A_l \times \sqrt{\pi A_l}/(\Omega \lambda_{\text{th}})$, where λ_{th} is the thermal conductivity. In GaAs $\lambda_{\text{th}} \simeq 50\,\text{Wm}^{-1}\text{K}^{-1}$. Using $P/A_l = 10^6\,\text{Wm}^{-2}$, $A_l = (20\mu\text{m})^2$, and $\Omega = \pi/2$, we estimate the temperature rise at the spot to be 0.5 K.

33. The parameter values used in the model calculations for the GaAs materials are as follows. The Schottky barrier height in the equilibrium state, for n-type material: $|\Phi_s^0|=0.8\pm0.2\,\mathrm{V}$, and for p-type material $|\Phi_s^0|=0.4\pm0.1\,\mathrm{V}$. The radius of the effective semiconductor transport section: for n-type material $R_s=1.1\pm0.4\,\mu\mathrm{m}$, and for p-type material $R_s=0.3\pm0.2\,\mu\mathrm{m}$ (in each figure R_s was taken to be constant, except in Fig. 2.9). The ideality factor: $n=1.1\pm0.1$. The γ-factors of Eq.(2.4): $\gamma_t=0.1\pm0.1$, and $\gamma_s=0.02\pm0.02$ (in each figure the γ-factors were taken to be constant). Parameters of fixed magnitude: $C_t=0.3\,\mathrm{fF}$, $C_{str}=0.3\,\mathrm{fF}$, $v_r=10^5\,\mathrm{ms}^{-1}$, $\eta_q\eta_c=1$, $f_{abs}=0.2$, $\beta=38.7\,\mathrm{V}^{-1}$, $E_{ph}=1.96\,\mathrm{eV}$, and $\epsilon_s=13$.

34. In a serial arrangement of a tunnel barrier and a Schottky barrier, the current depends on the tip-sample separation (d) via the change of the tunnel barrier conductance (cf. Eq. 2.9) *as well as* via the change of the Schottky barrier height (cf. Eq. 2.4), as was also clearly pointed out in Ref. [19] for example. However, the Schottky barrier height is only of importance if the Schottky barrier (instead of the tunnel barrier) is the limiting factor for current conduction, i.e. when V_s is non-zero. In Fig. 2.10 this implies that for $d-d_0$ larger than 1 nm, the tunnel current is not determined by the band-bending in the semiconductor, but only by the tunnel barrier conductance.

35. According to Eq.(2.15) a power modulation of $10^5\,\mathrm{Wm}^{-2}$ at 4 kHz induces a change of tip-sample separation of 0.01 nm due to thermal expansion (this is an upper limit, because lateral heat transport has been neglected). Using the data in Fig. 2.10, the mentioned change of tip-sample separation gives a change of the tunnel barrier conductance of less than 10%.

36. Capacitive coupling of a photoexcited semiconductor tip has also been detected in an atomic force microscope: J. Mertz, M. Hipp, J. Mlynek, and O. Marti, Appl. Phys. Lett. **64**, 2338 (1994).

37. It follows from the model calculations of Figs. 2.12 and 2.13 that – under the specified operating conditions – the following statements are justified. First, it appears that the Schottky capacitance per unit area is of the order of $10^{-3}\,\mathrm{Fm}^{-2}$, and that the Schottky conductance per unit area ranges from $10^4\,\Omega^{-1}\mathrm{m}^{-2}$ at the lowest light intensities, up to $10^7\,\Omega^{-1}\mathrm{m}^{-2}$ at the strongest illumination. Since the modulation frequency was 84 kHz, this implies that the maximum complex angle of $\tilde{Y}_s$ is close to $10^{-2}\,\mathrm{rad}$. Hence we can essentially neglect the Schottky capacitance and assume $\tilde{Y}_s$ to be equal to $\tilde{G}_s$. As a result, the stray capacitance signal is purely imaginairy, which served as an additional phase calibration of the measurements. The tunnel barrier capacitance cannot be neglected; at 84 kHz the complex angle of Y_t amounts to a couple of tens of rad. Second, the semiconductor is operated in the photovoltaic regime, i.e. at every point $G_t \ll A_s\tilde{G}_s$. This implies that in sweeping the optical intensity, $\tilde{G}_s$ is the parameter that varies most strongly.   In view of the previous considerations, the power dependence of ΔI_C is determined by the factor $\Delta J_p/\tilde{G}_{s,w}$. The value of $\tilde{G}_{s,w}$ follows from the DC solution of the wide current channel: for $J_p<J_0$ the Schottky conductance has

a finite value close to $\tilde{G}_{s,w} = \beta A_s J_0$; if $J_p > J_0$ the value of $\tilde{G}_{s,w}$ becomes proportional to P. Thus we expect ΔI_C to initially increase with increasing P, and to flatten off at higher light intensities.

38. Taking account of the comments of Ref. [37], the magnitude of the in-phase component essentially behaves as $\Delta I_{tp} \propto P/\tilde{G}_{s,c}$. This yields a similar power-dependence as was discussed for ΔI_C [37].

39. At high optical power $\tilde{G}_{s,c}$ varies linearly with P. Since $\Delta I_{tp} \propto P/\tilde{G}_{s,c}$, at high power ΔI_{tp} is constant.

40. J.A. Dagata, W. Tseng, J. Bennett, F. Schneir, and H.H. Harary, Appl. Phys. Lett. **59**, 3288 (1991).

41. M. Passlack, M. Hong, E.F. Schubert, J.R. Kwo, J.P. Mannaerts, S.N.G. Chu, N. Moriya, and F.A. Thiel, Appl. Phys. Lett. **66**, 625 (1995).

42. M.J. Gallagher, T.G. Ruskell, D. Chen, D. Sarid, and H. Jenkinson, Appl. Phys. Lett. **64**, 256 (1994).

Chapter 3

Magneto-optical near-field imaging*

3.1 Introduction

Optical imaging with a resolution better than the wavelength of the light can be obtained by scanning a probe in close proximity to a sample, provided that the probe-to-sample separation and the probe diameter are of subwavelength size [1]. As was discussed in Chapter 2, in a scanning tunneling microscope (STM) [2] optical sensitivity can be obtained with semiconductor tips. Optical excitation of a semiconductor material generates electron-hole pairs, that are separated by the electric field in the semiconductor subsurface band-bending region. This results in a surface photovoltage and the possibility to draw a current without applying an external bias. The active detector size – represented by the so-called photocarrier collection radius – is essentially determined by the optical penetration depth, the minority carrier diffusion length, and the profile of the band-bending region, all of which can be tuned to be of subwavelength extent. Furthermore, in an STM the tip-to-sample separation is of the order of one nanometer (see Ref. [25] of Chapter 2). As a result, with semiconductor tips in an STM we have the opportunity to develop a convenient technique for

near-field optical imaging with a very high spatial resolution.

In an optical microscope, magnetic sensitivity can be achieved by the magneto-optical Kerr or Faraday effect [3]. This involves the detection of the modified amplitude and/or the polarization state of light that has interacted with a magnetic sample; the Faraday effect refers to a transmission geometry, and the Kerr effect to a reflection geometry. If one would like to use the magneto-optical effects for magnetic imaging with semiconductor tips in an STM, an optical modulation technique is required. This is due to the fact that the stabilization of the STM is generally performed by a constant-current feedback system, having a bandwidth of approximately 2 kHz. In this Chapter we will present a model experiment on magneto-optical near-field imaging, that is based on the modulation of the optical polarization. Via the tunneling current, the polarization-dependent optical transmission through a magnetic sample is detected. This is also refered to as the detection of Faraday ellipticity or magnetic circular dichroism (MCD) [3]. In this geometry we will demonstrate magnetic sensitivity by measuring a hysteresis loop and by imaging magnetic domains with sub-wavelength resolution. Attention is also paid to non-magnetic contrast that can occur in the measurements. Finally we will discuss the opportunities and restrictions of this novel magneto-optical imaging technique.

3.2   Experiment
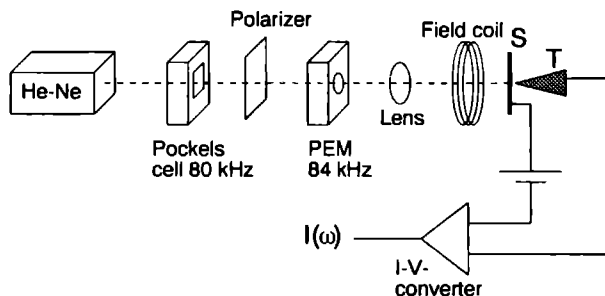
Figure 3.1: Experimental arrangement. See the text for further explanation.

The experiments were performed in an STM at ambient temperature and pressure. As depicted in Fig. 3.1, a semiconductor tip (T) was illuminated along the tip axis through a semitransparent sample (S). The sample was constituted of a thin ferromagnetic film on a glass substrate. A magnetic field coil was placed around the STM, producing DC fields up to 80 kA/m and pulsed fields of 800 kA/m. The optical beam of a linearly polarized single-mode HeNe laser (633 nm) was guided through a Pockels cell and a polarizer, which provided an intensity modulation (IM) of a few percent at 80 kHz.

Next the beam passed through a photoelastic modulator (PEM), introducing a 84-kHz sinusoidal polarization modulation (PM) between right- and left-handed circular polarization of the light. Finally the beam was focused onto the tunnel junction by a 30-mm focal length objective, to a spot of 20±5 μm diameter. To the metallic sample an external voltage V_m was applied. The current I was measured by a homemade 100-mV/nA current-to-voltage converter with a bandwidth of about 100 kHz. This signal was fed into two lock-in amplifiers for phase-sensitive detection of the current modulation. The bandwidth of the STM constant-current regulation system was 2 kHz. At every point of the scan the topographical height was recorded simultaneously with the current modulations at 80 kHz and 84 kHz.

The intensity modulation signal served to determine the optical response of the tip R, being the ratio of the detected relative tunnel current modulation $\Delta I^{IM}/I$ with respect to the preset relative modulation of incident optical power $\Delta P/P$. The calibrated polarization modulation signal is $\Delta I^{PM}/I$ divided by the response R and multiplied by $\sqrt{2}$ to account for the rms value of sinusoidal modulation. In order to be consistent with the definition of Faraday ellipticity [4] the circular dichroism signal (CD) is the calibrated PM signal divided by a factor of two.

The GaAs tips were prepared by cleaving (001) wafers along (110) and (110) directions, forming a corner bounded by these planes. Inspection by scanning electron microscopy and STM showed that cleavage produced well defined corners with tip apex radii smaller than 100 nm. We extensively characterized these tips by measuring current versus voltage curves with and without illumination, and by determining the current response to small light power variations (see section 2.4 of Chapter 2). While scanning we carefully followed the tip behavior by monitoring the quality of the topographical images and the stability of the response R.

When irradiating a semiconductor tip with a modulated light intensity, a modulation of current can be detected due to photoexcited carriers and due to thermal expansion (for a detailed description of these issues we refer to Chapter 2). The photocarriers can cause a direct as well as a displacement current to flow between the tip and the sample. The displacement current is due to the modulation of surface photovoltage on the irradiated part of the tip. In the following measurements, the signals due to displacement currents were more than ten times smaller than the signals measured while tunneling. We have corrected for the displacement current by substracting the modulation offset measured when the tip was out-of-tunneling range. Furthermore, we verified that the signal contribution due to thermal expansion was at least an order of magnitude smaller than the signal due to the direct current.

The Pt/Co multilayer sample consists of a 6-Å Pt base layer and 20 pairs of 3.5-Å Co and 6-Å Pt layers evaporated on a glass substrate [5]. This material is of special interest due to its perpendicular magnetic anisotropy, large magneto-optical constants, and resistance to oxidation. For the imaging experiment the sample was homogeneously magnetized except for rows of thermomagnetically written bits of opposite magnetization; this pattern was verified by far-field Kerr microscopy. Writing
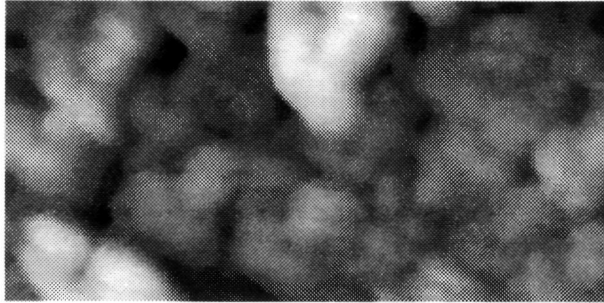
Figure 3.2: Topographic $100\times50\,\text{nm}^2$ scan of the Pt/Co multilayer, showing the characteristic microcrystallites. Greyscale range is $2\,\text{nm}$. Imaged with a p-type GaAs tip of $5\times10^{23}\text{-m}^{-3}$ doping density. Set DC tunnel current $I = 0.05\,\text{nA}$, $V_m = 0.5\,\text{V}$ (reverse bias direction). Incident light intensity $1\times10^6\,\text{Wm}^{-2}$.

was accomplished in a field of $25\,\text{kA/m}$ by locally heating the Pt/Co multilayer with a 488-nm Ar$^+$-laser beam focused onto the sample by a microscope objective. The bits have a diameter of $0.8\pm0.2\,\mu\text{m}$ and are spaced $2.0\pm0.1\,\mu\text{m}$ apart within the rows. The rows are separated by a distance of 2 to 3 μm.

3.3   Results

Fig. 3.2 shows a $100\times50\ \text{nm}^2$ topographic scan of a Pt/Co multilayer, obtained with an illuminated GaAs tip. The characteristic microcrystallites of 10 to 20 nm diameter originate from the columnar growth of the multilayer [5]. To demonstrate that our experimental arrangement is sensitive to sample magnetization, Fig. 3.3 shows hysteresis loops obtained with a macroscopic photodetector and obtained in the STM. Arrows indicate that the film was brought into its full remanent state with a $800\,\text{kA/m}$ pulse. The film was subsequently demagnetized by applying an external field H of increasing strength, each field application lasting for one second. After each field application the field was switched off and the helicity asymmetry was measured. The symbols represent individual measurements. Fig. 3.3A shows the circular dichroism (CD) of the film measured with a 1-mm diameter laser beam and a macroscopic photodetector. Fig. 3.3B shows a similar measurement made in an STM with a GaAs tip (n-type, $2\times10^{23}\,\text{m}^{-3}$ doping density). Both curves are of similar shape and signal size. However, to make certain that we are measuring the Faraday effect in the STM we conducted three control experiments. We checked that capping the Pt/Co multi-

photodetector

STM
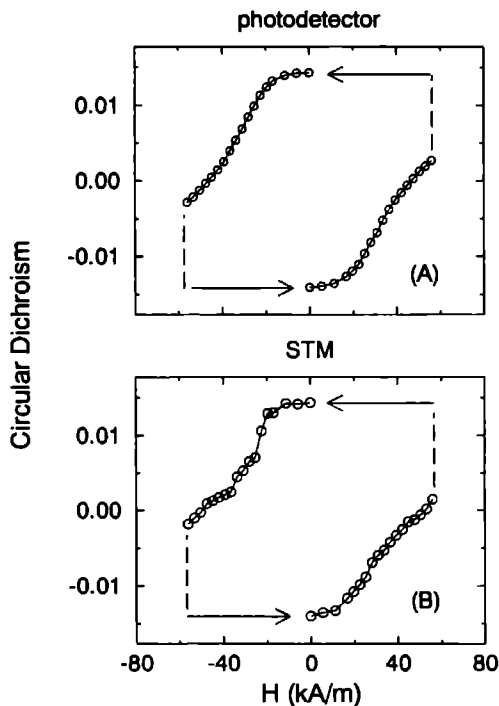
Figure 3.3: Circular dichroism (CD) of a Pt/Co multilayer having perpendicular magnetic anisotropy. Curve (A) is measured with a photodetector behind the free-standing multilayer. Curve (B) is measured in an STM with GaAs tip (n-type, $2\times10^{23}\,\mathrm{m}^{-3}$ doping density); set DC tunnel current $I = 0.9\,\mathrm{nA}$, $V_\mathrm{m} = 0$. For curve (B) the estimated measurement uncertainty is 2×10^{-3}. See text for further explanation.

layer with a 20-nm Au film did give similar results. We also verified that no current modulation signal was present when light of modulated linear polarization was used. Finally, in case of a non-magnetic Au film we verified that no helicity-dependent signal was detected in the tunnel current. Hence, we are clearly able to measure Faraday ellipticity with a semiconductor tip in a scanning tunneling microscope.

Fig. 3.4 demonstrates the magneto-optical imaging capabilities of our semiconductor tips. Fig. 3.4A shows a $6.0\times3.6\,\mu\mathrm{m}^2$ image of the magnetic bits, taken in 8 minutes observation time. The bits were detected by the CD signal measured while scanning. In this image the bits were written in rows from bottom to top. Indeed, we observe that in this direction the inter-bit distance is approximately $2\,\mu\mathrm{m}$. Outside the area with the bits a CD signal with uniform sign has been observed, whereas on the bits
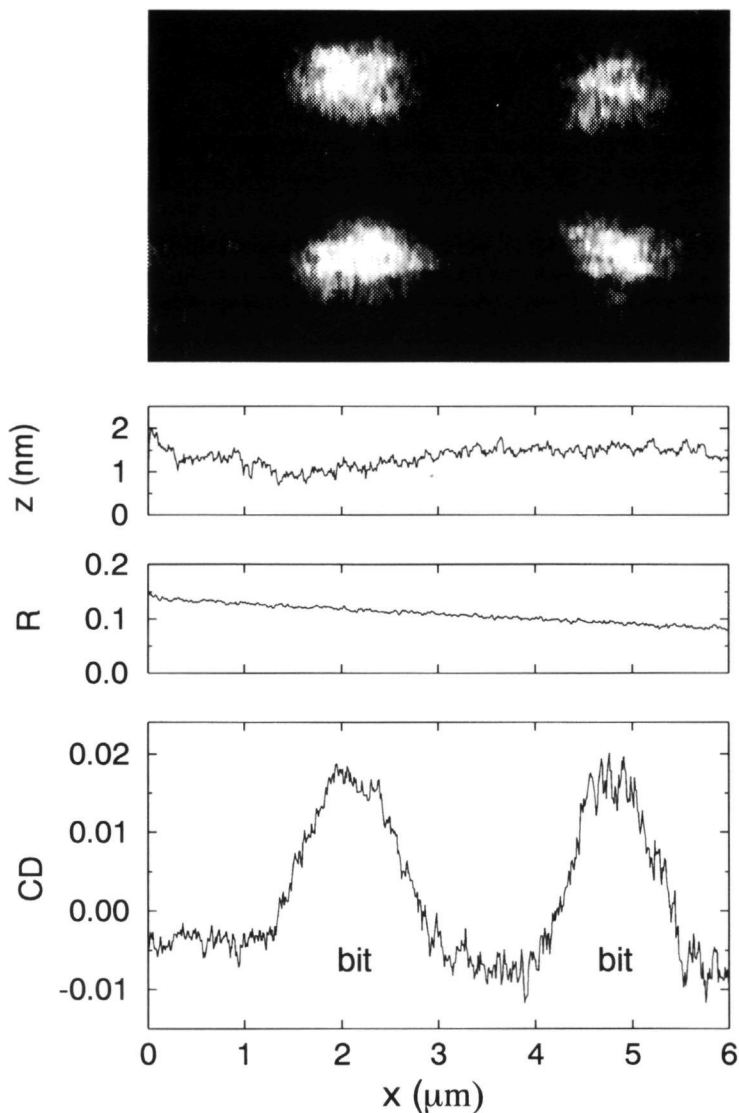
Figure 3.4: (A) Circular dichroism (CD) image of magnetic bits written in a Pt/Co multilayer. Curves (B)-(D) represent topography, response, and circular dichroism respectively, measured on a horizontal line scan over the two topmost bits of image (A). Recorded with a p-type 4×10^{23}-m^{-3} doped GaAs tip. Incident illumination intensity $1\times10^6\,\mathrm{Wm^{-2}}$. Set DC tunnel current $I = 0.5\,\mathrm{nA}$, $V_m = 0.5\,\mathrm{V}$ (reverse bias direction).

a sign reversal of the CD signal was found. The observation of a sign reversal is in agreement with the fact that the bits have opposite magnetization with respect to the rest of the sample. Further details are given in Fig. 3.4B to 3.4D, showing the simultaneously measured topography, response R, and CD signal on a line scan over the two topmost bits of Fig. 3.4A. The fine structure on the topographic signal is due to the presence of microcrystallites, as has been shown in Fig. 3.2. Note that the scales for the topographic corrugation and the lateral coordinate differ by three orders of magnitude. The response R is essentially flat and merely shows a gradual lateral variation, probably due to differences in light power arriving at the sample. It is only in the CD signal that the bits become clearly visible.

The difference of CD on the bits and aside of the bits yields a value for the measured *magnetic* circular dichroism (MCD) of 1.1×10^{-2}. Shining a 1-mm diameter laser beam through the homogeneously magnetized part of the Pt/Co multilayer and placing a macroscopic photodetector behind the sample, we measured a MCD of 1.4×10^{-2} (as in Fig. 3.3A). With respect to this measurement, in the STM the size of the MCD is reduced by 20 to 30 percent. This can be ascribed to multiple reflections taking place between the apex of the GaAs tip and the metallic sample: the presence of GaAs in close proximity (~ 1 nm) to the sample causes an enhanced optical transmission and a reduced MCD (we verified this effect by magneto-optical calculations, as described in section 4.3.3 of Chapter 4). When the tip was retracted from the sample by $0.5\,\mu m$, i.e. by a distance larger than the tip radius, a measurement of the MCD using the displacement current gave the same value as measured with the photodetector. Note that we did not observe a reduction of MCD in Fig. 3.3B: for an n-type GaAs tip of $2 \times 10^{23}\,m^{-3}$ doping density the photocarrier collection radius ($\sim 1\,\mu m$, see Chapter 2) is an order of magnitude larger than the tip radius ($\sim 0.1\,\mu m$), such that multiple reflections play an insignificant role.

Comparing the CD measured on the bits with the CD aside of the bits, we observe that the CD reverses sign but is of unequal magnitude. This we attribute to the presence of a non-magnetic contribution to the CD. In part this can be due to a residual intensity modulation present in the incident optical beam. Also, the non-magnetic signal can be due to a polarization-sensitivity intrinsically present in the tunnel junction. An asymmetry to circular polarization can be caused by the combination of an element shifting the optical phase and a polarizing element, as is easily shown with the aid of Jones matrices [6]. A phase-shift may be introduced by a tilt of the sample normal with respect to the light propagation direction, while polarization-sensitivity can originate from a tip being tilted or having low symmetry at the apex. When tilt angles of tens of degrees are involved, the helicity-asymmetry can in principle be of the order of 10^{-2} [7].

As pointed out, using a semiconductor tip we are able to determine magneto-optical properties of a sample on a very local scale. Occasionaly, the CD-images taken on the sample area with prewritten bits were perturbed by interference-like features, of which a dramatic example is shown in Fig. 3.5. The vertical axis represents the

Figure 3.5: Circular dichroism image of magnetic bits, including interference-like features. See the text for further explanation. Area $6.1 \times 3.0 \, \mu m^2$.

slow scanning direction. Neither the simultaneously measured topographical image nor the image of the optical response R revealed any irregularities. In the upper part of the CD image (most clearly in the upper left corner) we observe a horizontal line of discontinuity in the interference rings. Above that line the interference pattern seems to be 'dragged' along in the slow scanning direction. At the top of the image the scanning was suddenly interrupted by instabilities in the feedback system, after which the tip did not any more yield proper scans. We observed interference-like features in several separate measurements, most notably on a part of the sample with a visible density of tiny fragments, deposited by crashing a previous GaAs tip. Furthermore, whenever the scanning tip would approach the center of the rings, the scanning was interrupted by tunneling instabilities. We attribute these observations to the presence of a particle on the sample surface in the vicinity of the imaged area. We believe that the pattern of rings is due to the interference of the normally transmitted light with the waves scattered by the particle. A 'dragged' interference pattern (as at the top of Fig. 3.5) may then be explained as the result of a weakly bound particle that is slowly moved over the surface by the scanning tip. In this interpretation, the fact that the center of the rings could never be imaged is understandable if the particles are too large to be imaged, if the particles are weakly attached to the sample surface, or if the particles badly conduct the current to the sample surface. A detailed understanding of the shape of the observed interference image requires a model calculation on the near-field optical pattern that is set up between the sample, the tip and the particle. This issue remains to be investigated.

3.4   Discussion and conclusions

In the Pt/Co multilayers used, the domain wall width is of the order of the grain size, which is 10 to 20 nm in our case. From the steepest edges observed in our circular dichroism images, we estimate that the lateral optical resolution is 250 nm with a p-type GaAs tip of 10^{23}-m^{-3} doping density, at the specified operating conditions. This resolution is determined by the extent to which photocarriers generated in the tip are able to reach the apex and tunnel into the counter electrode, as pointed out in Chapter 2. The collection volume of photocarriers is determined by several parameters, such as the tip shape, the penetration depth of the light, the photocarrier diffusion length, and the depletion field profile. In our imaging experiments the incident optical intensity was 1×10^6 Wm^{-2}. Taking account of approximately 20% optical transmission through the sample, and using a photon-to-electron conversion efficiency of 100%, we find a maximum density of photocarrier current arriving at the semiconductor surface of $0.1\,\mu A$ per μm^2. Since we are drawing 0.5 nA of tunnel current, we can estimate the minimum collection area of photogenerated charge to be approximately $(70\,nm)^2$. This value is of the same order as the measured lateral optical resolution squared. The important point is that although the tip is scanning in full illumination, causing both near- and far-field radiation to be absorbed in the tip, the tip volume that can supply carriers to the tunneling current is limited due to the optical and electrical transport lengths involved (see also Chapter 2). The main optical parameter is the penetration depth of the light, which in GaAs is 250 nm for radiation of 633 nm wavelength [8]. Important electrical transport lengths are the minority carrier diffusion length ($\sim\mu m$ [9]) and the depletion region width (~70 nm). A decrease of collection volume may be achieved by (i) a reduction of the diffusion length (higher doping density, or a different semiconductor material), (ii) a reduction of the optical penetration depth to below the depletion region width (radiation of shorter wavelength), or (iii) a reduction of the focusing properties of the depletion field (forward bias operation, or a sharper tip). A resulting reduction of detectable photocarrier current has to be compensated for by increasing the optical power. Special care will have to be taken to avoid signals due to thermal expansion to start dominating, for example by increasing the modulation frequencies. As an example, having 10 mW light power absorbed in the tip with a 20-μm spot diameter, and drawing 0.5 nA of tunnel current, we estimate a lateral optical resolution of 6 nm to be achievable with a tip having an optimized collection volume of photocarriers (with these parameters the estimated tip temperature rise is about 15 K; see Ref. [32] of Chapter 2).

An advantage of the above presented technique is that simultaneously magnetic information and high-resolution topographic information is extracted. Furthermore, since the probe is non-magnetic, one can study the sample properties upon application of an external magnetic field. For geometrical reasons (e.g. sample roughness [10] or the presence of scattering centers) in images also non-magnetic polarization contrast

may appear. These effects can be substracted by reversing the sample magnetization. It is interesting to note that our measurement technique allows for studies of both electrical and magnetic sample ordering, by using circular and linear light polarizations. Optical intensity as well as optical rotation may be detected. In order to detect the optical rotation, a tip with analyzing power is required; covering one side of a cleaved GaAs tip by a metallic thin film we verified that a high degree of linear polarization-sensitivity can indeed be achieved. Our technique may be operated in both a transmission and in a reflection geometry. For the reflection geometry, one may consider irradiation from the side of the tip, or irradiation along the tip axis if the tip shaft is transparent. Detection of the optically induced displacement current opens the possibility for a fast imaging mode. A measurement scheme that is closely related to the above presented technique is spin-polarized tunneling by optical spin-orientation in GaAs, which will be treated in Chapter 4. The magneto-optical Kerr/Faraday effect is sensitive to the *bulk* magnetization, whereas spin-polarized tunneling is sensitive to the spin-polarization of electronic states at the sample *surface*. The respective effects may be separated by their dependence on excitation wavelength, surface preparation, and bias voltage. Ideally, one would like to combine the two measurements, so as to be able to simultaneously measure sample topography, bulk magnetization, and surface spin-structure with (sub)nanometer resolution.

References

1. *Near field optics*, edited by D.W. Pohl and D. Courjon, (Kluwer, Dordrecht, 1993).
2. A review on STM can be found in: *Scanning tunneling microscopy I, II, and III*, edited by R. Wiesendanger and H.-J. Güntherodt, Springer series in surface science vol. 20, 28, and 29 (Springer Verlag, Heidelberg, 1992/93).
3. For a review on magneto-optical effects see: M.J. Freiser, IEEE Trans. Magn. **4**, 152 (1968).
4. W. Reim and J. Schoenes, in *Ferromagnetic Materials*, Vol. 5, edited by K.H.J. Buschow and E.P. Wohlfarth (Elsevier, Amsterdam, 1990), p. 134.
5. W.B. Zeper, F.J.A.M. Greidanus, P.F. Garcia, and C.R. Fincher, J. Appl. Phys. **65**, 4971, (1989); W.B. Zeper, H.W. van Kesteren, B.A.J. Jacobs, J.H.M. Spruit, and P.F. Carcia, J. Appl. Phys. **70**, 2264 (1991). Our Pt/Co multilayers were prepared by H.W. van Kesteren, H.C. Donkersloot and J.M. Kerkhof at the Philips Research Laboratories, Eindhoven.
6. R.M.A. Azzam and N.M. Bashara, *Ellipsometry and polarized light* (North Holland, Amsterdam, 1987).
7. When an optical plane wave arrives at an abrupt interface (discrete change of refractive index from value N_1 to N_2), the relative Fresnel transmission coeffi-

cient for s-polarized light with respect to p-polarized light is given by: $\rho = t_s/t_p = [N_2\cos(\theta_1) + N_1\cos(\theta_2)]/[N_1\cos(\theta_1) + N_2\cos(\theta_2)]$, where θ_1 and θ_2 are the angles between the interface normal and the optical propagation direction in materials 1 and 2 respectively [6]); when N_2 differs from N_1 by an appreciable amount (as is the case for an air-metal interface for example), it follows that ρ can deviate from unity by an amount of the order of 0.1 when θ_1 is a couple of tens of degrees. A helicity-asymmetry can result from a series of *two* interfaces that are tilted with respect to the optical propagation direction, provided that the propagation vector and the normal vectors of the two interfaces do not lie in one and the same plane.

8. D.E. Aspnes and A.A. Studna, Phys. Rev. **B27**, 985 (1983).

9. R.K. Ahrenkiel, chapter 2 in *Minority carriers in* III-V *semiconductors: physics and applications*, edited by R.K. Ahrenkiel and M.S. Lundstrom, Semiconductors and semimetals vol. 39 (Academic Press, San Diego, 1993), p. 39 .

10. T.J. Silva, S. Schultz, and D. Weller, Appl. Phys. Lett. **65**, 658 (1994).

Chapter 4

Spin-polarized tunneling by optical spin-orientation*

Abstract

We describe a model as well as experiments on spin-polarized tunneling with the aid of optical spin-orientation. This involves tunnel junctions between a magnetic material and gallium-arsenide (GaAs), where the latter is optically excited with circularly polarized light in order to generate spin-polarized carriers. As in our (non-polarized) transport model of Chapter 2, we take account of carrier capture in the semiconductor surface states. We propose to describe the semiconductor surface in terms of the spin-dependent energy distribution function, the so-called surface spin-splitting. This can be calculated from the balance of the polarized electron and hole flow in the semiconductor subsurface region, the polarized tunneling current across the tunnel barrier between the magnetic material and the semiconductor surface, and the spin-relaxation at the semiconductor surface.

We present measurements on the circular-polarization-dependent photocurrent (the so-called helicity-asymmetry) in thin-film tunnel junctions of $Co/Al_2O_3/GaAs$. In the absence of a tunnel barrier, the helicity-asymmetry is caused by magneto-optical effects (magnetic circular dichroism). In case a tunnel barrier is present, the data cannot be explained by magneto-optical effects only; the deviations provide evidence that spin-polarized tunneling due to optical spin-orientation occurs. In

Co/τ-MnAl/AlAs/GaAs junctions we did not observe deviations from the magneto-optical effects, most probably due to the weak spin-polarization of τ-MnAl along the tunneling direction.

Also, we present data obtained in a scanning tunneling microscope (STM) with a GaAs tip and a Pt/Co multilayer sample under ambient conditions. A helicity-asymmetry of tunnel current was found with a size of 4 pA, which was verified not to be due to variations of the optical power. According to our model and estimations, this observation can be explained by spin-polarized tunneling, with a lower limit to the semiconductor surface spin-splitting and spin-lifetime of 4 mV and 0.4 ns respectively.

4.1   Introduction

Since the early seventies, spin-polarized tunneling studies have been conducted in order to derive information about spin-dependent electronic states [1]. Nearly all of these studies involved thin-film tunnel junctions. With the advent of the scanning tunneling microscope (STM) [2] in the eighties, the possibility emerged to perform tunneling studies on a highly localized scale. However, it is non-trivial to develop a spin-selective STM probe (a so-called tunneling tip), that would allow for studies of the spin-dependent electronic structure of magnetic materials with atomic resolution. In this respect, there are essentially three possibilities for the tip material: (i) a superconductor, (ii) a magnetic material, or (iii) a semiconductor. For each of these materials, in this introductory section we will very briefly point out how spin-selectivity can be achieved, and mention the experiments already performed with planar solid-state tunnel junctions as well as in an STM.

(i) The measurement of spin-polarized tunneling with a superconducting material, is based on the Zeeman splitting of the (unpaired) quasiparticle states of a spin-paired superconductor (for an excellent review see [1]). As a result of an applied magnetic field H, in a small spectral range of order $\mu_B H$ at the edges of the superconducting gap, tunneling with only one spin-orientation is achieved. By measuring the differential conductance versus applied voltage, it is possible to determine the spin-polarization of the tunneling current. Many successful experiments were performed with thin-film tunnel junctions involving superconducting Al, an Al_2O_3 tunnel barrier, and a wide variety of magnetic counter electrodes. In these junctions the electron spin is well-conserved during the tunneling process. The application of this technique in an STM is difficult, because a tip with a superconducting state at the apex has to be operated in rather high magnetic fields. To our knowledge, this technique has not yet been applied in an STM.

(ii) In case of tunneling between two magnetic materials, the quantity to be determined is the junction conductance for parallel versus antiparallel orientation of the electrode magnetizations. The relative change of the conductance gives a measure for the product of the spin-polarizations of the electrode materials. This technique

has been treated in a number of theoretical papers [3]. Experiments have been performed with planar junctions [4] as well as with an STM in an ultra-high vacuum environment [5]. Due to magnetostriction and magnetostatic interactions, in an STM the relative orientation of the tip and sample magnetization is not easily modified without changing the tip-to-sample distance. In addition, the perturbation of the sample magnetic structure by the tip remains a matter of concern. It may however be possible to obtain some information on spin-polarized tunneling by comparing the surface topography and current-voltage characteristics measured with a magnetic tip on different atomic sites.

(iii) Due to the spin-orbit interaction, by optical means a spin-selectivity can be achieved in a non-magnetic semiconductor. For that reason also a III-V semiconductor material can be used in a spin-polarized tunneling experiment. For example, the injection of non-equilibrium spin-polarized carriers can be detected due to the emission of polarized radiation. In an STM the emission of polarized luminescence due to spin-polarized tunneling has already been observed with ferromagnetic tips and a GaAs sample [6]. On the other hand, spin-polarized carriers can be created by photoexcitation with circularly polarized light, so-called optical spin-orientation [7]. The possibility of using optical spin-orientation in GaAs for the purpose of spin-polarized tunneling has been discussed in several publications [8]-[13]. These ideas originate from the successful operation of spin-polarized electron sources based on optical excitation of cesium-covered p-type GaAs (e.g. [14]). The application of GaAs for magnetic imaging has become a hot issue with the development of cleaved GaAs tips for STM operation, under ultra-high vacuum conditions [15] as well as under ambient conditions [16, 17]. In the latter studies, optical excitation was already included, but the spin-sensitivity of GaAs tips was not yet demonstrated.

In this Chapter we will be concerned with the usage of optical spin-orientation in GaAs in order to achieve spin-selectivity in a tunneling arrangement. First, a model description of spin-dependent transport will be given. This model includes the subsurface transport processes in the semiconductor and spin-relaxation at the semiconductor surface. Experimental results obtained with planar junctions as well as with STM will be presented. Finally we will discuss the application of optical spin-orientation in GaAs for atomic-scale magnetic imaging.

4.2   Spin-dependent transport model

In this section we describe a model for spin-dependent transport in a tunnel junction between a metallic and a semiconductor material, when optical spin-orientation is applied. This system is rather complicated, because one should not only consider the tunnel current between the metal and the semicondutor surface, but also the electron and hole currents in the semiconductor subsurface region. The tunneling current has already been treated theoretically by Molotkov [11] in a Green's function formalism,

and by Laiho and Reittu [12] for plane electronic waves; we will describe the tunneling current by the transfer Hamiltonian approach [18], in a convenient form for a modulation experiment. To our knowledge, the spin-dependent transport in the semiconductor, including the subsurface electron and hole currents, the surface states and spin-relaxation therein, has not been treated elsewhere. The incorporation of surface states into a model description is particularly important when considering semiconductor tips, because at the tip apex surface states are present due to the strongly reduced crystallographic symmetry (so even in a well-controlled environment).

In a III-V semiconductor like GaAs, optical spin-orientation involves photoexcitation with light of circular polarization [7]. At the direct gap of GaAs the conduction band is predominantly formed of Ga-derived wavefunctions with s-symmetry, whereas the valence band consists of As-derived wavefunctions of p-symmetry. Because of the spin-orbit interaction in the valence band, the optical transition probabilities are such that circularly polarized photons with an energy close to the bandgap give a maximum spin-polarization of 50% in unstrained GaAs [19]. An important consequence of optical spin-orientation, is that in the semiconductor the energy distribution of charge carriers deviates from equilibrium and is unequal for the two spin-orientations, the latter quality being essential for a spin-polarized tunneling experiment.

In the following, we will first consider the spin-dependent tunneling current flowing between a magnetic material and a semiconductor surface, for a given spin-dependent energy distribution of carriers at the semiconductor surface. Next, we will present a model description of the mechanisms that determine the size of the spin-dependence of the energy distribution function at the semiconductor surface, the so-called semiconductor surface spin-splitting.

Spin-polarized tunneling. The present derivation of the spin-dependent tunneling current is based on the transfer Hamiltonian approach, a first order perturbation method that applies in case of a low tunnel barrier transparency [18]. As depicted in Fig. 4.1, the magnetic electrode is described by single-particle spin-dependent wavefunctions ψ_μ^σ with energies E_μ^σ, and by a spin-independent energy distribution function $\mathcal{F}_m$. The σ-superscript indicates the spin-orientation with respect to a given quantization axis (parallel or spin-up equals $\uparrow$, antiparallel or spin-down equals $\downarrow$); we will use identical spin quantization axes for the two materials. Since the semiconductor is not magnetic, the semiconductor surface is described by the spin-independent wavefunctions ψ_ν with energies E_ν; however, due to optical spin-orientation the carriers at the semiconductor surface follow a spin-dependent energy distribution ($\mathcal{F}_s^\sigma$).

In a good tunnel barrier no scattering centers are available, such that the electron energy and the electron spin are conserved during the tunneling process. In that case, the tunnel current (I_t^σ) for spin-orientation σ from the magnetic material to the
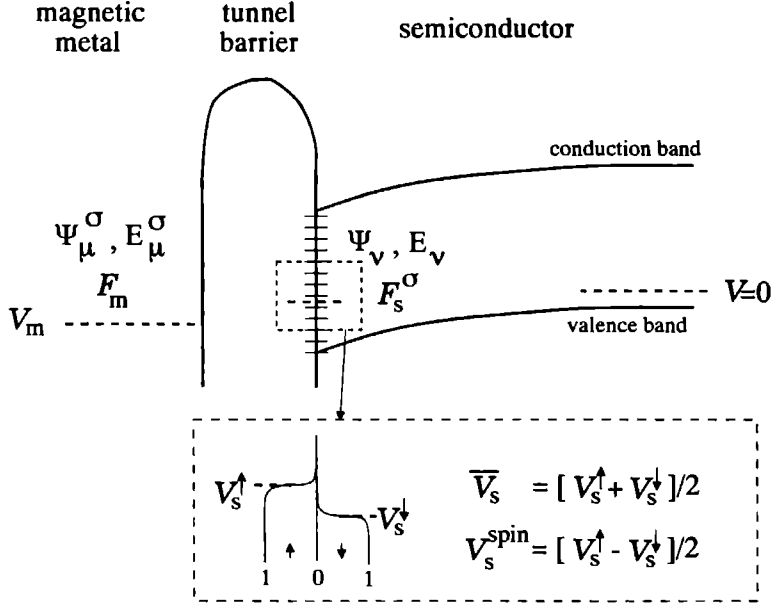
Figure 4.1: One-dimensional electronic energy diagram of a tunnel junction between a magnetic metal and a p-type semiconductor. The blow-up shows the occupation of the surface states for the two spin-directions. The spin-dependent quasi-Fermi level is represented by V_s^σ. See the text for further explanations. The picture is not on scale, because in general the band-bending region in the semiconductor is considerably larger than the tunnel barrier width.

semiconductor surface can be expressed as follows:

$$I_t^\sigma \quad = \quad \frac{1}{-e} \int d\varepsilon \; [\; \mathcal{F}_m(\varepsilon + eV_m) - \mathcal{F}_s^\sigma(\varepsilon) \;] \; G_t^\sigma(\varepsilon) \tag{4.1}$$

$$G_t^\sigma(\varepsilon) \quad = \quad \frac{2\pi e^2}{\hbar} \sum_{\mu\nu} \delta(\varepsilon + eV_m - E_\mu^\sigma) \, \delta(\varepsilon - E_\nu) \, |M_{\mu\nu}^\sigma|^2 \tag{4 2}$$

$$M_{\mu\nu}^\sigma \quad = \quad \frac{\hbar^2}{2m} \int d\vec{S} \cdot [\; \psi_\mu^{\sigma*} \nabla \psi_\nu - \psi_\nu \nabla \psi_\mu^{\sigma*} \;] \tag{4.3}$$

where e is the absolute magnitude of the electron charge. The magnetic electrode is at the externally applied potential V_m. The energy-zero is given by the Fermi level in

the semiconductor bulk. The function $G_t^\sigma(\varepsilon)$ takes account of all energy-conserving tunneling transitions at energy ε, for states with spin-orientation σ. As we will see, G_t^σ closely relates to the differential tunneling conductance. $M_{\mu\nu}^\sigma$ is the well-known tunneling matrix element; the surface integral ($\int dS$) is evaluated inside the barrier separating the two materials. Note that no assumption is made with respect to the shape of the two electrodes, or the dimensionality of the system. The matrix element takes account of the overlap of the wavefunctions of the respective electrode materials. This parameter is spin-dependent because the wavefunctions of the magnetic material depend on the electron spin. Calculation of the total tunnel current yields:

$$I_t \;=\; \sum_\sigma I_t^\sigma \;=\; \frac{1}{-e} \int d\varepsilon \; \{ \; \underbrace{[G_t^\uparrow + G_t^\downarrow][\mathcal{F}_\mathrm{m} - \overline{\mathcal{F}}_\mathrm{s}]}_{\text{spin-integrated}} - \underbrace{[G_t^\uparrow - G_t^\downarrow][\mathcal{F}_\mathrm{s}^\uparrow - \mathcal{F}_\mathrm{s}^\downarrow]/2}_{\text{spin-selective}} \; \} \;, \quad (4.4)$$

where $\overline{\mathcal{F}}_\mathrm{s} \equiv [\mathcal{F}_\mathrm{s}^\uparrow + \mathcal{F}_\mathrm{s}^\downarrow]/2$ is the spin-averaged distribution function at the semiconductor surface. The first term takes account of the spin-integrated tunnel current. The second term is present in case of a spin-polarized magnetic material ($G_t^\uparrow \neq G_t^\downarrow$) and a spin-imbalance in the semiconductor ($\mathcal{F}_\mathrm{s}^\uparrow \neq \mathcal{F}_\mathrm{s}^\downarrow$). An expression similar to Eq.(4.4) was derived in Ref. [11]. In the following we will assume that at the semiconductor surface each spin-subsystem is close to thermal equilibrium, because the processes of carrier capture and relaxation are generally very efficient at surfaces with surface states [20]. This means that the spin-subsystems approximately follow an energy-shifted Fermi-Dirac distribution: $\mathcal{F}_\mathrm{s}^\sigma(\varepsilon) \simeq f(\varepsilon + eV_\mathrm{s}^\sigma)$, where V_s^σ is the spin-dependent surface potential. As indicated in Fig. 4.1, this allows for the definition of the spin-averaged surface potential: $\overline{V}_\mathrm{s} \equiv [V_\mathrm{s}^\uparrow + V_\mathrm{s}^\downarrow]/2$, and of the surface spin-splitting: $V_\mathrm{s}^\mathrm{spin} \equiv [V_\mathrm{s}^\uparrow - V_\mathrm{s}^\downarrow]/2$.

In our experiments a modulation of optical polarization and/or of optical intensity is applied. As a result, the spin-dependent distribution function at the semiconductor surface becomes time-dependent with the following form: $\mathcal{F}_\mathrm{s}^\sigma(t) = \mathrm{Re}\{\mathcal{F}_\mathrm{s}^\sigma + \Delta\mathcal{F}_\mathrm{s}^\sigma \exp(j\omega t)\}$, where ω is the modulation frequency. The associated time-dependent surface potential becomes: $V_\mathrm{s}^\sigma(t) = \mathrm{Re}\{V_\mathrm{s}^\sigma + \Delta V_\mathrm{s}^\sigma \exp(j\omega t)\}$. To first order in the modulation amplitudes, with Eq.(4.4) we find the following modulation of the total tunneling current:

$$\Delta I_t \;=\; - \; \{ \; \underbrace{[G_t^\uparrow + G_t^\downarrow] \, \Delta\overline{V}_\mathrm{s}}_{\text{spin-integrated}} + \underbrace{[G_t^\uparrow - G_t^\downarrow]\Delta V_\mathrm{s}^\mathrm{spin}}_{\text{spin-selective}} \; \} \;, \quad (4.5)$$

where $\Delta\overline{V}_\mathrm{s} = [\Delta V_\mathrm{s}^\uparrow + \Delta V_\mathrm{s}^\downarrow]/2$, and $\Delta V_\mathrm{s}^\mathrm{spin} = [\Delta V_\mathrm{s}^\uparrow - \Delta V_\mathrm{s}^\downarrow]/2$. The spin-selective contribution of Eq.(4.5) can also be written as follows:

$$\Delta I_t \;=\; - \, G_t \, \mathcal{P}(G_t) \, \Delta V_\mathrm{s}^\mathrm{spin} \;, \quad (4.6)$$

where $G_t \equiv G_t^\uparrow + G_t^\downarrow$ and $\mathcal{P}(G_t) \equiv [G_t^\uparrow - G_t^\downarrow]/G_t$. The negative sign in Eq.(4.6) results from the definition of the direction of current flow. $\mathcal{P}(G_t)$ is the normalized polar-

ization of the spin-dependent tunnel conductance. This quantity was evaluated by Laiho and Reittu [12, 13] for a two-band free-electron ferromagnet in a planar junction, showing that the size of $\mathcal{P}(G_t)$ depends not only on the bulk bandstructure, but also on the tunnel barrier height and shape. Experiments [1] as well as calculations [12] indicate that $\mathcal{P}(G_t)$ can be tens of percents for materials like Fe, Co, and Ni.

An ideal optical spin-orientation experiment involves only a modulation of the surface spin-splitting (ΔV_s^{spin}), not a modulation of the spin-averaged surface potential ($\Delta \overline{V_s}=0$). However, in case of an unwanted modulation of the optical power, the spin-averaged potential will also modulate*. This can for example be due to the magneto-optical Kerr/Faraday effect (see Chapter 3). Also non-magnetic effects can give a modulation of optical power, for example polarization-dependent optical scattering in the tunnel junction, or imperfect alignment of optical components. In our experiments, we find that ΔV_s^{spin} and $\Delta \overline{V_s}$ are of comparable size, namely of the order of a few percent of $\overline{V_s}$, i.e. of the order of 10 mV. In order to separate the spin-selective from the spin-integrated contributions to the current modulation, an additional technique is required. As will be demonstrated in sections 4.3 and 4 4, the separation can be achieved by varying the photon energy, the tunnel barrier width, and the applied voltage In addition to the above described modulation of tunnel current, displacement currents and signals due to thermal expansion can appear (see Chapter 2). These signals are not of interest here, since they carry no spin-selectivity.

Semiconductor surface spin-splitting.   The spin-dependence of the energy distribution function at the semiconductor surface (the so-called surface spin-splitting) is determined by the flow of spin-polarized minority and majority carriers in the semiconductor subsurface region**, the spin-relaxation rate at the semiconductor surface, and the spin-polarized tunnel current from the semiconductor surface to the magnetic electrode. In order to calculate the semiconductor spin-splitting, we present a one-dimensional spin-dependent transport model This model is based on the work of Chapter 2, where the electron spin was still ignored. As was already pointed out in Fig. 4.1, the metal-semiconductor junction is modeled as a device with three 'electrodes': the metallic electrode, the semiconductor surface states, and the semiconductor bulk. The metal is biased with respect to the semiconductor bulk Fermi level by the externally applied voltage V_m. Between the metal and the surface states a tunnel barrier is present; the surface states and semiconductor bulk are separated

---

*A modulation of optical power causes a nonzero $\Delta \overline{V_s}$, but also affects the value of ΔV_s^{spin} However, the relative change of the value of ΔV_s^{spin} is only of the order of $\Delta \overline{V_s}/\overline{V_s}$, which is negligible in our experiments

**Note that in a semiconducting material it is important to discriminate between majority and minority *carriers* (holes or electrons) As we will see in section 4.3 3, in magnetic materials it is often useful to distinguish the majority and minority *spin-direction*. The notions of majority and minority particles always refer to the situation encountered in the bulk of the material

by a Schottky barrier, i.e. the semiconductor subsurface band-bending region. The band-bending region represents a barrier for majority carrier transport; at the same time, it constitutes an accelerating field for photoexcited minority carriers. It was pointed out in Chapter 2 that the deviations from one-dimensional carrier flow in an STM junction can be accomodated by introducing an effective section for minority and majority carrier transport in the semiconductor subsurface region; for clarity, we will omit this effective transport section in the following.

The important spin-polarized currents are given by: the current density of photoexcited carriers (J_p^σ), the majority carrier current density through the Schottky barrier (J_s^σ), and the tunnel current density (J_t^σ). We define J_t^σ to flow from the magnetic electrode to the semiconductor surface; J_p^σ and J_s^σ represent flow from the semiconductor surface to the semiconductor bulk. Let the density of spin-up(-down) electrons at the semiconductor surface be given by $N_{ss}^\uparrow (N_{ss}^\downarrow)$. The excess density of spin-up electrons is defined as $N_{ss}^{spin} \equiv N_{ss}^\uparrow - N_{ss}^\downarrow = -eV_s^{spin} D_{ss}$, where D_{ss} is the total density of surface states (units $m^{-2}J^{-1}$). The density of surface states is assumed to be uniform over the range of interest (as for example applies to the native oxide on GaAs [21]). When at the surface the spin-lifetime is given by τ^{spin}, the density of current flowing from the spin-up to the spin-down spin-subsystem at the surface becomes:

$$J_{ss}^{spin} = \frac{-eN_{ss}^{spin}}{\tau^{spin}} = \frac{e^2 D_{ss}}{\tau^{spin}} V_s^{spin} \equiv \tilde{G}_{ss}^{spin} V_s^{spin} , \qquad (4.7)$$

where $\tilde{G}_{ss}^{spin} \equiv e^2 D_{ss}/\tau^{spin}$ is the spin-conductance between the spin-subsystems at the semiconductor surface. The tilde ($\tilde{\ }$) denotes that the conductance is defined per unit area. Bookkeeping of the flow of spin and charge yields the following equations for the spin-dependent current densities at the semiconductor surface:

$$J_p^\uparrow + J_s^\uparrow - J_t^\uparrow + J_{ss}^{spin} = 0$$
$$J_p^\downarrow + J_s^\downarrow - J_t^\downarrow - J_{ss}^{spin} = 0 \qquad (4.8)$$

Adding and substracting these equations, and using the normalized spin-polarizations of the respective currents, we find:

$$J_p + J_s - J_t = 0$$
$$J_p \mathcal{P}(J_p) + J_s \mathcal{P}(J_s) - J_t \mathcal{P}(J_t) + 2\tilde{G}_{ss}^{spin} V_s^{spin} = 0 \qquad (4.9)$$

where $J_i \equiv J_i^\uparrow + J_i^\downarrow$ and $\mathcal{P}(J_i) \equiv [J_i^\uparrow - J_i^\downarrow]/J_i$, $i \in \{p, s, t\}$. The so-called photoamperic mode of operation of the metal-semiconductor tunnel junction (see Chapter 2) refers to the situation that the tunnel barrier represents a far higher conductance than the Schottky barrier, i.e. $J_t \simeq J_p$, and $|J_s| \ll |J_p|$. In that limit the size of the tunneling current (J_t) is given by the size of the photocurrent (J_p), and is not affected by the polarization of the photocurrent $\mathcal{P}(J_p)$. Or to put it differently, whatever the polarization of the photocurrent, all the photoexcited carriers will be tranported into

the metallic electrode, because the Schottky barrier is too high. This is an unde-
sirable situation for a spin-polarized tunneling experiment, where spin-sensitivity is
wanted in the total tunneling current. In order to maximize the spin-sensitivity in
the total tunneling current, we should operate in the so-called photovoltaic regime
(see Chapter 2), when the tunnel barrier conductance is lower than the conductance
of the Schottky barrier. Then the tunnel current (J_t) is negligible with respect to
the photocurrent, and $J_s \simeq -J_p$. This situation has the important advantange that
the spin-splitting at the semiconductor surface is only determined by the photocur-
rent and the Schottky majority carrier current, independent of the tunneling current
properties.

Let us calculate the size of the spin-splitting at the semiconductor surface for
p-type GaAs in the *photovoltaic* mode of operation. By optical spin-orientation in
GaAs, the spins of the electrons as well as the hole spins are oriented in principle.
However, due to the spin-orbit interaction a strong coupling exists between the hole's
angular momentum and its quasimomentum ($\vec{k}$), resulting in a loss of the hole spin-
orientation on the timescale of the momentum relaxation time ($\tau_p \sim 10^{-13}$ s); in the
conduction band this strong coupling is absent, causing the electron spin-lifetime to
be many orders of magnitude larger [22]. In p-type GaAs the bands are generally
bending downward from the bulk toward the surface, which drives the optically ori-
ented electrons toward the surface [23]. In the photovoltaic mode of operation, this
flow of electrons (the minority carrier current J_p) is balanced by the hole current that
flows through the Schottky barrier (the majority carrier current J_s); the latter is given
by thermally-assisted transport over the electrostatic barrier and subsequent surface
recombination [24, 25] (see also Chapter 2). Since the holes are hardly polarized, we
can neglect the spin-dependence of the hole energy distribution in the semiconductor
bulk; in addition, for a small spin-splitting the surface recombination velocity does
not depend on the electron spin. In other words, in p-type GaAs we can to first or-
der neglect the polarization of the majority carrier current $\mathcal{P}(J_s)$ with respect to the
polarization of the minority carrier current $\mathcal{P}(J_p)$; In that case, using Eqs.(4.7) and
(4.9) in the photovoltaic mode of operation ($J_t = 0$), we find the following expression
for the spin-splitting of the surface potential:

$$V_s^{\text{spin}} = -\mathcal{P}(J_p) J_p \frac{\tau^{\text{spin}}}{2e^2 D_{ss}} \quad . \tag{4.10}$$

Thus, for a maximum spin-selective tunneling current (cf. Eq. 4.6), it is appropriate
to use p-type GaAs in the photovoltaic mode of operation, with a large magnitude
and polarization of the photocarrier current, a large surface spin-lifetime, and a low
density of surface states.

In summary, we have analyzed the spin-dependent tunneling current in a tunnel
junction between a magnetic material and a semiconductor, where in the latter a

modulation of spin-orientation was established by optical means. In the semiconductor, account was taken of the polarized hole and electron currents, and the carrier capture and transport in the surface states. For future directions, it will be of interest to model the polarization of the majority carrier current, which will be important for large values of the surface spin-splitting and for n-type materials [23].

4.3 Planar junctions

4.3.1 Introduction

This section deals with experiments on planar ferromagnet/insulator/semiconductor junctions. The sample substrate is GaAs, with a tunnel barrier of Al-oxide or AlAs. The ferromagnet is a Co thin film, with or without an ultrathin τ-MnAl film inserted. In these junctions the light traverses the magnetic thin film before reaching the semiconductor material. This implies that the magneto-optical Faraday effect can be of importance. Upon transmission through the magnetic film, the change of optical *polarization* is of the order of 10^{-2}, which can safely be neglected. More importantly, the Faraday effect results in a helicity-dependence of the transmission of optical *power* into the semiconductor material, an effect that is also of the order of 10^{-2}. In other words – when applying a technique of modulation of optical polarization – concurrently with a modulation of the spin-orientation of the electrons also the amount of photoexcited carriers is modulated. In the context of Eq.(4.5), this was refered to in terms of the spin-selective and spin-integrated contributions to the current modulation. The two contributions can be separated by varying the photon energy and by comparing devices with different tunnel barrier thicknesses [26], as will be described in the following sections.

4.3.2 Experiment

GaAs(Al/Al$_2$O$_3$)Co   The samples with an Al$_2$O$_3$ tunnel barrier were prepared in an eletron-beam evaporation system. The substrates were GaAs (110) surfaces cleaved under ambient conditions. The exposure of the GaAs to the ambient gives an oxidic layer with a thickness of about a nanometer and a high density of surface states [21]. The GaAs was p-type (Zn doped) or n-type (Si doped) with doping densities in the range 10^{23} to 10^{24} m^{-3}. First, on the substrate an Al film was deposited; in order to prevent island growth the substrates were cooled with liquid nitrogen. Subsequently, during a couple of hours the Al was oxidized by a glow discharge in oxygen at a pressure of $\sim$0.1 Torr, while the sample was allowed to reach room temperature. Similar procedures are known to produce good tunnel barriers with a thickness of about 2 nm (e.g. [1, 4]). Finally, 15 nm of Co and a 5-nm Au cap layer were deposited. A quartz microbalance was used to measure the film thickness.

All depositions were carried out at approximately 0.2 nm/s with a chamber pressure in the 10^{-7} Torr range.

GaAs(AlAs)τ-MnAl Co[*]   The samples with an AlAs tunnel barrier were prepared by molecular beam epitaxy (MBE) on GaAs (001) substrates. The growth was done in two separate MBE chambers, the first containing non-magnetic elements only, the second one including some magnetic elements. The base pressure of the chambers was in the high 10^{-11} and low 10^{-10} Torr range, respectively. The growth rates were controlled by setting the atomic or molecular fluxes to the desired value, and by *in situ* measuring the RHEED (reflection high-energy electron diffraction [27]) intensity oscillations. The RHEED pattern served to monitor the surface structure and verify the epitaxial growth of the layers. In the first chamber a 1-μm thick p-doped buffer layer (C-doped, 10^{24} m^{-3}) was deposited on a p-type GaAs (001) substrate, at a growth temperature of 560 °C and a growth rate of $\sim$1μm per hour. The substrate was then cooled to room temperature and an As passivation layer was deposited during 2 hours to protect the sample from the atmosphere during transfer to the second chamber. To regain the p-doped GaAs surface, in the second chamber the substrate was heated to evaporate the As protection layer and some remaining oxygen. An epitaxial AlAs tunnel barrier was then deposited (20 nm AlAs for sample M171, and 2 nm AlAs for sample M172) at a substrate temperature of 580 °C.

There is a limited set of ferromagnetic materials that can epitaxially be grown on AlAs, one of these materials being τ-MnAl. The latter is a metastable phase of the intermetallic MnAl system, with a composition ratio Mn/Al of about 55/45 [28]. τ-MnAl has a tetragonal unit cell, and is well lattice-matched to GaAs. On the AlAs tunnel barrier an ultra-thin τ-MnAl layer was deposited (as a so-called template) for Co epitaxy. The template involved the deposition of 5 alternating monolayers of Mn and Al (5 so-called bilayers) to form an amorphous layer, and annealing at $\sim$250°C to form a crystalline template [29]. This template allows for growth of the forced bcc phase of Co [30]–[32]. 4 nm of Co were deposited at a substrate temperature of $\sim$250 °C and a rate of 75 nm/h. The growth was concluded by an amorphous GaAs passivation layer (15 nm) deposited at $\sim$80 °C.

Measurement.   As sketched in Fig. 4.2, in our experiments the propagation direction of the incident optical beam was collinear with the applied magnetic field, and (within about 5°) also collinear with the sample normal. For the mentioned ferromagnetic thin films the easy magnetization orientation is in the film plane. A magnetization-component parallel to the incident beam was created by an external magnetic field of 300±30 kA/m, supplied by an electromagnet with a hole bored through one pole for optical access. Sample sizes were a few mm^2. Low-impedance back contacts to the substrate were made by InGa droplets. Typical excitation levels

---

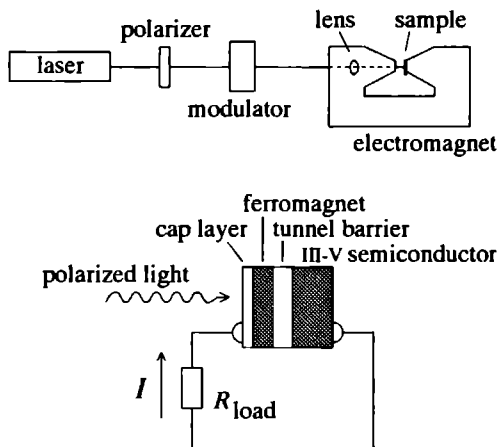[*]These samples were prepared by W. Van Roy at the IMEC, Leuven, Belgium.

Figure 4.2: Experimental arrangement (top) and device construction (bottom).

were a few mW focussed to a spot diameter of about 50 μm, yielding closed circuit currents (I) in the μA range. Different photon energies were provided by an Ar-ion (for photon energies of 2.71, 2.54 or 2.41 eV), a HeNe (1.96 eV), and an AlGaAs (1.52 eV) laser. The helicity-dependence of the current was determined by modulating the light between positive and negative helicity, and measuring the response with a lock-in amplifier (ΔI). A reversal of magnetic field was employed in order to substract minor signals of non-magnetic origin (electrical pickup or a residual intensity modulation due to imperfect optical alignment).

For all devices we measured the current response (R) to a modulation of incident optical power (ΔP), where the response is defined as $R = [\Delta I/I]/[\Delta P/P]$. For junctions with a tunnel barrier, we observed that the response became larger than unity and phase-shifted at modulation frequencies higher than about one kilohertz; this we attribute to the appearance of a displacement current that flows through the tunnel barrier. Since in the following experiments we want to detect direct currents only, we chose the modulation frequency low enough to ensure that the response (R) was unity. The application of an external bias of more than a few tenths of a volt across the samples often gave rise to a sudden lowering of the device resistance. This is indicative of the formation of low-resistance spots, most probably at the sample edges. We verified that the helicity-asymmetry $\Delta I/I$ was not sensitive to a sudden change of the device resistance; this can be understood from the fact that a low-resistance spot simply operates as a resistor in parallel to the externally attached load resistance (R_{load} in Fig. 4.2). In the following measurements the load resistance was lower

than the internal resistance of the junctions, and no external bias was applied to the junctions.

4.3.3   Results and discussion

Al$_2$O$_3$ barrier.   The top panel of Fig. 4.3 shows the helicity-asymmetry $\Delta I/I$ as a function of photon energy, for samples of different growth batches. Devices (A) are constructed without an Al/Al$_2$O$_3$ interlayer. As was pointed out with Eq. (4.9), in devices without a tunnel barrier the spin-dependent effects should be minimized, such that only magneto-optical effects can give a helicity-asymmetry to the tunnel current. For these devices, the dashed line (A') represents a calculation of the helicity-asymmetry of the optical power absorbed in the semiconducting substrate; the optical propagation and absorption in the layered system was calculated with a matrix formalism [33] that takes account of the (polarization-dependent) complex refractive indices of the layers [34]. The optical constants were taken from the literature [35, 36]. As can be seen from comparison of curves (A) to the calculation (A'), this description of the magneto-optical signal is quite accurate; the difference between the magnitude of the measured values (left scale) and the calculated values (right scale) is due to the incomplete magnetization of the ferromagnetic thin film, as we confirmed by measurements at higher fields.

Device (B) was prepared by depositing a single 8-nm Al film, that was subsequently oxidized. The Al$_2$O$_3$ layer has a thickness of $\sim$2 nm [1, 4], so that $\sim$6 nm of Al remains between the GaAs and the Al$_2$O$_3$. Due to the conducting Al film on the semiconductor surface, devices prepared in this way are not expected to show maximum spin-dependent transmission effects (this was not yet recognized in our previous publication in Ref. [37]). This expectation is based on the high density of states at the semiconductor surface, which according to Eq. (4.10) gives a low spin-splitting at the semiconductor surface. Additional magneto-optical calculations on the structure of device (B) show that – when compared to device (A) – the helicity-asymmetry is reduced by 20% at 1.5 eV and is modified by less than 4% at 2.7 eV. Since these reductions are approximately observed, we conclude that also device (B) shows a helicity-asymmetry mainly due to magneto-optical effects.

Device (C) is composed of a double barrier, i.e. twice an Al film of $\sim$2 nm was deposited and oxidized. Since these Al films were so thin, we can assume that they were completely oxidized [1, 4]. Additional magneto-optical calculations on the structure of device (C) point out that – when compared to device (A) – the magneto-optical contribution to the helicity-asymmetry is changed by less than 4% in the photon energy range of interest. In other words, the strong deviations of curve (C) from curve (A) – at 1.5 eV photon energy a reduction of helicity asymmetry of 60% – cannot be explained by magneto-optical effects. The striking feature is that the deviations are largest at near-bandgap excitation (i.e. toward 1.42 eV), and that curve (C) converges with curve (A) at higher photon energy: qualitatively the same wavelength depen-
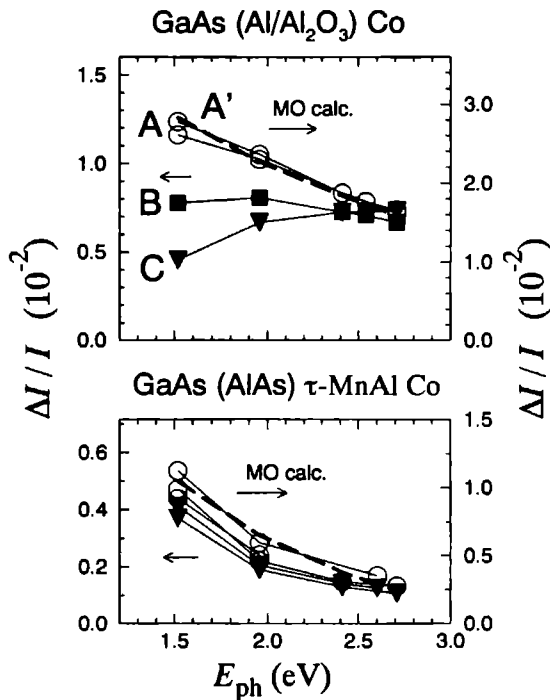
Figure 4.3: Helicity asymmetry $\Delta I/I$ as a function of photon energy E_{ph}. Top: Al_2O_3 devices. Curves (A) represent the measured asymmetries for devices with no Al/Al_2O_3 interlayer. Curve (B) refers to a device of incompletely oxidized Al ($\sim$6 nm Al and $\sim$2 nm Al_2O_3). Curve (C) gives the results for a completely oxidized Al interlayer ($\sim$4 nm Al_2O_3). The dashed line (A') represents a magneto-optical calculation of the helicity-asymmetry of optical power absorbed in the GaAs substrate in the absence of an Al/Al_2O_3 interlayer (MO calc, right scale). Bottom: AlAs devices. The circular symbols represent data of samples with a 2-nm AlAs barrier, whereas the triangular symbols refer to samples with a 20-nm AlAs barrier. The dashed line represents a magneto-optical calculation of the helicity asymmetry of optical power absorbed in the GaAs substrate (MO calc, right scale). Solid lines are guides to the eye.

dence is observed for spin-polarized photoemission from cesium-covered GaAs [7]. This wavelength dependence is mainly determined by the spectral behavior of the optical dipole transitions and spin-relaxation mechanisms [7]. Following our model description (cf. Eq. 4.5) we attribute the observed deviations of curve (C) from curve (A) to a spin-selective current contribution, i.e. the occurance of spin-dependent tunneling of optically oriented carriers.

At $1.5\,$eV photon energy, the measured difference of the helicity asymmetry $(\Delta I_t/I_t)$ between curves (C) and (A) of Fig. 4.3A amounts to $(7\pm1)\times10^{-3}$. Let us analyse this observation with our model of spin-dependent transport, in order to deduce the spin-splitting at the semiconductor surface. It follows from other measurements on Al_2O_3 tunnel barriers [38], that the differential tunneling conductance is rather constant in case of a voltage drop of less than a tenth of a volt, and that for higher voltages the differential conductance increases with a quadratic dependence on the voltage drop. In other words, a lower limit to the differential tunneling conductance is given by $G_t \geq I_t/[V_m - \overline{V}_s]^*$; because no external voltage was applied in these experiments ($V_m = 0$), with Eq.(4.6) we find that the relative spin-splitting at the semiconductor surface is either given by:

$$\frac{\Delta V_s^{\text{spin}}}{\overline{V}_s} = \frac{1}{\mathcal{P}(G_t)} \frac{\Delta I_t}{I_t} \tag{4.11}$$

or is of a lower absolute magnitude. In earlier spin-polarized tunneling measurements with fully magnetized Co, a spin-polarization of $|\mathcal{P}(G_t)|=0.35$ was detected [1]; in our experiment, along the direction of the incident beam the magnetization was measured to be less than 50% of its saturation value, such that a reasonable estimate for $|\mathcal{P}(G_t)|$ is 0.15 ± 0.05. Using the measured value for $\Delta I_t/I_t$, with Eq.(4.11) we deduce that the relative spin-splitting at the semiconductor surface $(\Delta V_s^{\text{spin}}/\overline{V}_s)$ was lower than or equal to $(5\pm2)\times10^{-2}$ in this experiment. As was pointed out with Eqs.(4.9) and (4.10), the value of the surface spin-splitting (V_s^{spin}) is not only determined by the photoexcited minority carrier current, but also by the surface spin-relaxation, the Schottky majority carrier current, and the tunneling current. The magnitude of the spin-averaged potential $(\overline{V}_s)$ strongly depends on the Schottky barrier height (see Chapter 2). In our devices the determination of the spin-averaged potential $(\overline{V}_s)$ was inhibited due to the presence of low-resistance spots, so that we are unable at present to further analyze the previous experimental result in the perspective of our model description.

Finally, we tentatively analyze the sign of the spin-polarization of the tunnel conductance that follows from our measurment. In magnetic materials, it is common

---

*We neglected the spin-selective contribution with respect to the spin-integrated contribution. This is allowed, because we will find that the relative spin-splitting at the semiconductor surface was far smaller than unity in this experiment.

usage to define the electron spin-orientation to be positive if the electron belongs to the majority-spin type, i.e. if the magnetic moment of the electron is aligned with the sample magnetization (e.g. [1, 39]). For electrons the orientation of the spin-magnetic moment is opposite to the spin-orientation. Thus, to be consistent with the above convention, we should choose the spin-quantization axis of the electronic wavefunctions *opposite* to the direction of the external magnetic field. In the following analysis we will define the spin-quantization axis of the electronic wavefunctions to be equal to the sample normal, and choose the external magnetic field to be parallel to the propagation direction of the incident beam. In that case, it follows from other measurements [40] that the magnetic circular dichroism of Co is such that light of negative helicity is less strongly absorbed than light of positive helicity. This implies that due to magneto-optical effects, in our junctions a higher photocurrent is measured for light of negative helicity. When light of near-bandgap photon energy and negative helicity is used, the electron spins are preferentially oriented parallel to the quantization axis [7]: $V_s^{\text{spin}}/\overline{V}_s > 0$ if $V_m = 0$. Since we attributed a *decrease* of $\Delta I/I$ to spin-polarized tunneling, using Eq.(4.11) we derive that the spin-polarization of the tunnel conductance $\mathcal{P}(G_t)$ was of negative sign. In earlier spin-polarized tunneling measurements with superconducting Al and an Al_2O_3 tunnel barrier, with fully magnetized Co a spin-polarization of $+0.35$ was detected, corresponding to predominantly tunneling of majority-spin electrons at the Co Fermi level [1]. It is well-known that different measurement techniques can give a different sign for the spin-polarization; for example, spin-polarized photoemission from Co shows predominantly minority-spin electrons at the Fermi level [41, 42]. Comparing our measurement with the measurements of Ref. [1], it may well be that in the respective experiments the electron tunneling occurs at a different energy.

AlAs barrier. The bottom panel of Fig. 4.3 shows the helicity-asymmetry $\Delta I/I$ as a function of photon energy for devices with an AlAs tunnel barrier, a τ-MnAl template, and a Co thin film. The circular symbols represent measurements on samples with a 2-nm AlAs barrier, whereas the triangular symbols were measured on samples with 20 nm of AlAs. In the same way as was calculated for the Al_2O_3 junctions, the dashed line represents a magneto-optical calculation of the helicity-asymmetry of the optical power absorbed in the semiconducting substrate; we verified that the calculated helicity-asymmetry is hardly affected by the thickness of the AlAs interlayer.

In case of a spin-polarized tunneling effect, we expect to observe a different helicity-asymmetry of the current for samples with a thin and with a thick tunnel barrier, as was discussed with Eq.(4.9); this is not observed in Fig. 4.3. Futhermore, we observe that the measured data are close to the calculated magneto-optical curve. In other words, the data can be explained by magneto-optical effects only, and we find no evidence for spin-polarized tunneling within the measurement uncertainty of $\sim 10^{-3}$.
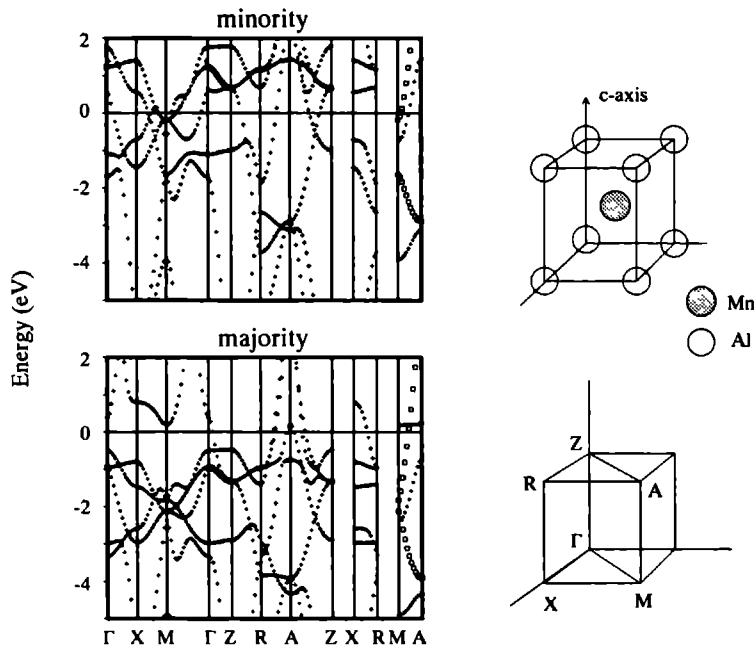
Figure 4.4: Electron energy bands of bulk τ-MnAl along high-symmetry directions, calculated with the Localized Spherical Wave (LSW) method. Crosses represent non-degenerate states, whereas squares represent double-degenerate states. On the right side are indicated the τ-MnAl unit cell and the irreducible part of the Brillouin zone.

Bandstructure calculations.   In view of the previous results, bandstructure calculations of τ-MnAl were performed by H. van Leuken at the University of Nijmegen (for details we refer to Ref. [43]). For both spin directions, Fig. 4.4 shows the calculated energy bands and Fig. 4.5 the calculated density of states. The spin-polarization of the total number of electrons at the Fermi level is $\mathcal{P}_N \equiv [N^\uparrow - N^\downarrow]/[N^\uparrow + N^\downarrow] = -0.37$, where $N^{\uparrow(\downarrow)}$ is the number of majority(minority)-spin electrons at the Fermi level. This polarization mainly results from the strongly spin-split Mn 3d-bands in the ΓXM-plane of the Brillouin zone, representing wavefunctions that are itinerant in the planes containing the Mn atoms.

Concerning the implications of the calculated bandstructure for a tunneling experiment, it is important to realize that tunneling is a direction specific probing tech-

Figure 4.5: Calculated density of states per unit cell in bulk τ-MnAl, for the minority and majority spins. Zero-energy corresponds to the Fermi level.

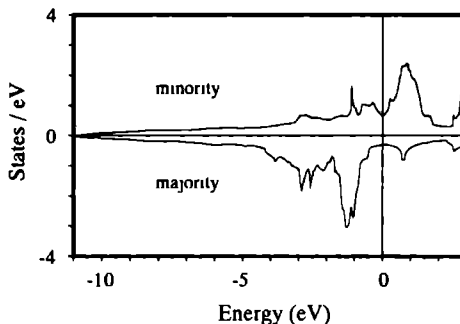nique. In our junctions, the tunneling direction is given by a cone of less than 5 degrees around the sample normal [48], which is the c-axis of the τ-MnAl unit cell. Thus, the most important contributions to the spin-dependent tunneling conductance G_t^σ (defined in Eq. 4.2) are given by the energy bands that are dispersive in the z-direction of the Brillouin zone, i.e. the bands that cross the high-symmetry directions ΓZ, MA and XR. Along these directions we observe a rather similar bandstructure for the majority- and minority-spin electrons: at the Fermi level the crossings of respectively three and four states are involved; when constructing the Fermi surface, it appears that for both spin-directions the mentioned axes are crossed by three Fermi sheets of comparable character. This is in strong contrast to the bandstructure-polarization in the ΓXM plane. In other words, along the xy-planes the conductance is strongly spin-polarized, whereas perpendicular to these planes a spin-polarization is hardly present. We also performed bandstructure calculations (not shown) for the structure of our samples (an ultra-thin τ-MnAl layer sandwiched between GaAs and Co). These calculations indicated that the electronic structure of the Mn and Al atoms adjacent to the GaAs is similar to the bulk τ-MnAl electronic structure, such that the previous analysis also applies to the junctions of our experiments.

4.3.4   Conclusions

An important outcome of our measurements on planar junctions, is that the detection of spin-polarized tunneling by optical spin-orientation can be complicated by the occurance of magneto-optical effects. In our measurements the magneto-optical contribution to the helicity-asymmetry of photocurrent (Faraday effect) is of the order of 10^{-2}, which is larger than the contribution attributed to spin-polarized transmission. Nevertheless, by varying the photon energy and the tunnel barrier thickness, it is pos-

sible to filter out the magneto-optical effects. We have obtained some experimental evidence for the presence of spin-polarized tunneling by optical spin-orientation in $Co/Al_2O_3/GaAs$ junctions, where the deduced relative spin-splitting at the semiconductor surface $(\Delta V_s^{spin}/\overline{V}_s)$ amounts to approximately 5×10^{-2}. In MBE-grown samples with an AlAs barrier we did not observe spin-polarized tunneling, most probably due to the presence of an ultrathin τ-MnAl layer adjacent to the AlAs barrier. The ultrathin template was needed for high-quality Co epitaxy. Spin-split bandstructure calculations confirmed that the conductance along the tunneling direction is hardly spin-polarized due to the τ-MnAl layer.

For future experiments it is important to reduce the magneto-optical contribution to the tunnel current modulation. Since the Faraday effect scales with the film thickness, ultrathin magnetic films can be used, such as MBE-grown Fe or Co (e.g. [50, 51]). Also it is of interest to avoid the appearance of low-resistance spots in the devices, for example by edge passivation; this will allow for detailed studies of the current-voltage characteristics, and for studies of the voltage dependence of the spin-polarized tunneling current.

4.4   STM junction

4.4.1   Introduction

A model experiment on optical spin-orientation in an STM can in principle be performed with a magnetic sample and a semiconductor tip, or with a semiconductor sample and a magnetic tip. It is important that radiation of near-circular polarization is absorbed near the STM tunneling point. Hence, an illumination geometry that approaches rotational symmetry is preferred, which is best achieved with illumination along the sample normal. This can involve the usage of a semiconductor membrane and a magnetic tip [52], or a semitransparent magnetic thin film and a semiconductor tip. The following sections deal with our experiments on a semitransparent Pt/Co multilayer and p-type GaAs tips.

As was pointed out with Eq.(4.5), when applying a modulation technique for spin-polarized tunneling by optical spin-orientation, one should separate the spin-integrated and spin-selective contributions to the current modulation. The spin-integrated contribution can in principle be caused by several effects: (i) Because the junction contains a magnetic material, a helicity-dependent optical transmission occurs due to magneto-optical effects such as magnetic circular dichroism [53]. (ii) If the geometry of the tip/sample combination is of low symmetry, the optical scattering and absorption in the tunnel junction can in principle depend on the helicity of the light; this is a near-field optical phenomenon that is hard to control. (iii) Finally, the modulation of optical power can be due to imperfect optical alignment, causing the optical beam that enters the STM to contain a small power modulation in addition to

the helicity modulation.

In the experiments with planar junctions, a variation of photon energy and sample magnetization were employed in order to separate the spin-averaged and spin-selective signals. However, in an STM experiment it is not trivial to employ these techniques without disturbing the critical optical alignment or the tunnel junction itself. On the other hand, in a metal-semiconductor STM junction there is a strong voltage-dependence of the sensitivity of the current to variations of the optical power (see Chapter 2); by sweeping the voltage, we can tune the tunnel junction to a low sensitivity to variations of the optical power, such that we can isolate a signal due to spin-polarized tunneling. The involved dual-frequency modulation technique and experimental results are presented in the following sections.

4.4.2   Experiment
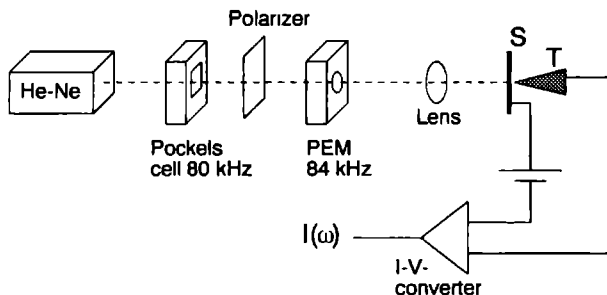
Figure 4.6: Experimental arrangement. See the text for explanation.

The experiments were performed in an STM at ambient temperature and pressure. As depicted in Fig. 4.6, the optical beam of a linearly polarized single-mode HeNe laser (633 nm) was guided through a Pockels cell and a polarizer, which provided an intensity modulation (IM) of a few percent at 80 kHz. The beam passed through a photoelastic modulator (PEM), introducing a 84-kHz sinusoidal polarization modulation (PM) between a positive and negative helicity of the light. Finally the beam was focused onto the tunnel junction by a 30-mm focal length objective, to a spot of 20 ± 5 μm diameter. The tunneling current (I_t) was measured by a homemade 100-mV/nA current-to-voltage converter with a bandwidth of about 100 kHz. Above $\sim$60 kHz the converter response was determined with an estimated accuracy of 10% and a phase uncertainty of about 10°. The bandwidth of the STM constant-current regulation system was 2 kHz. The current signal was fed into two lock-in amplifiers for phase-sensitive detection of the current modulation (ΔI_t) at 80 and 84 kHz. A signal of spin-polarized tunneling due to optical spin-orientation appears in the PM-signal (circular polarization modulation at 84 kHz). As was pointed out above, in the PM-

signal there can also be a contribution due to a simultaneously occuring unwanted modulation of the optical intensity at 84 kHz. We employ the IM-signal (intensity modulation at 80 kHz) in order to determine the sensitivity of the tunnel current to a modulation of optical intensity. This knowledge can serve to isolate the contribution due to spin-polarized tunneling in the PM-signal at 84 kHz (circular polarization modulation). The frequencies of the modulations (80 and 84 kHz) were chosen of similar magnitude in order to ascertain an equal response of the total current detection system.

The GaAs tips were prepared by cleaving (001) wafers along (110) and (1$\bar{1}$0) directions, forming a corner bounded by these planes. Inspection by scanning electron microscopy and STM showed that cleavage produces well-defined corners with tip apex radii smaller than 100 nm. The Pt/Co multilayer sample consists of a 6-Å Pt base layer and 20 pairs of 3.5-Å Co and 6-Å Pt layers evaporated on a glass substrate [54]. This material exhibits perpendicular magnetic anisotropy with 99% magnetic remanence. No external magnetic field was applied during the measurements.

4.4.3   Results

Fig. 4.7 shows static (so with the tip-sample distance regulation system turned off) curves of the current modulations measured by the lock-in amplifiers (top panel) and the measured tunneling current (bottom panel) versus applied voltage, for a p-type GaAs tip of 10^{25} m^{-3} doping density. The indicated data are averages of 225 spectrocopic curves, each curve taken in 60 ms time. In the bottom panel, the zero-current point is clearly displaced along the voltage axis, indicating the presence of a photoinduced surface voltage of about -0.1 V. The current modulations were detected in-phase with the modulations applied to the optical beam. The square symbols represent the signal due to a modulation of the optical intensity (IM). At reverse bias (positive sample voltage) the current is most sensitive to intensity variations, whereas in forward bias (negative sample voltage) the sensitivity is small. At even higher forward bias the modulation signal reverses sign. These observations are in agreement with the model and experimental results reported in Chapter 2. The circular symbols represent the signal measured at the frequency of circular polarization modulation (PM). Clearly this curve has a different voltage-dependence than the curve of intensity modulation. In particular, where the sensitivity to intensity modulation tends to zero, still a significant helicity-dependent current is observed of size $\Delta I_t = 4 \pm 1$ pA. We attribute this current modulation to spin-dependent tunneling of optically oriented charge carriers. The data in Fig. 4.7 represent the clearest indication that we obtained on the possibility of spin-polarized tunneling by optical spin-orientation in an STM. It was not possible to perform a similar measurement while scanning, due to the increased noise levels and shorter measurement times.
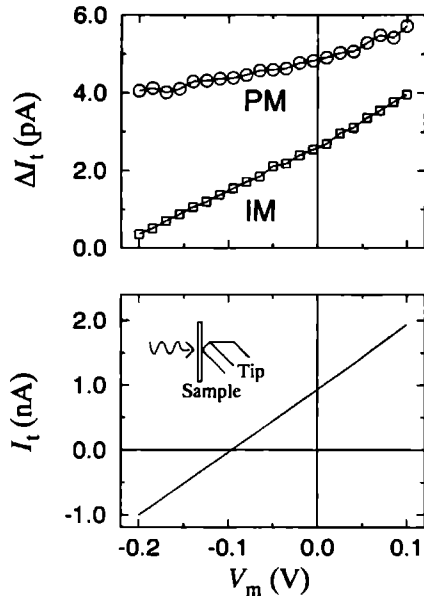
Figure 4.7: Experimental results of the dual-frequency modulation technique applied to a p-type GaAs tip of 10^{25} m^{-3} doping density tunneling on a Pt/Co multilayer. The indicated data are averages of 225 spectrocopic curves, each curve taken in 60 ms time. Top: Current modulations measured by the lock-in amplifiers, as a function of the voltage applied to the magnetic sample (V_m). The square symbols indicate the signal resulting from a modulation of the optical intensity (IM). The circular symbols denote the signal due to a modulation of the light polarization (PM). The estimated signal uncertainty due to drift during the measurements is about 1 pA. Bottom: Measured current versus voltage curve for the same junction. The inset shows the illumination geometry. Incident optical power P=5mW.

4.4.4   Discussion

With the aid of our model on spin-polarized transport, in the following we calculate the semiconductor spin-splitting and the surface spin-lifetime from estimations of the spin-polarization of the tunneling conductance and of the photocurrent.

Tunneling conductance polarization. In order to estimate the spin-splitting at the semiconductor surface, we need to assess the spin-polarization of the tunnel conductance $\mathcal{P}(G_t)$ for our Pt/Co multilayer. In earlier spin-polarized measurements with thin-film tunnel junctions, for Co a spin-polarization of $|\mathcal{P}(G_t)|$=0.35 was detected [1].

However, for several reasons we cannot simply adopt this value for our sample surface:
(i) The Pt/Co multilayer was capped with 6 Å of Pt, i.e. with 2 to 3 atomic layers
of Pt [57]. This means that the electron tunneling does not occur directly into the
Co, but rather into the Pt surface atoms that are spin-polarized due to the exchange
interaction with the underlying Co [41].
(ii) We do not expect the polarization of the electronic states to be uniform over
the sample surface, because the Pt/Co multilayer is constituted of microcrystallites
with a diameter of 10 to 20 nm [54], as we also verified with STM measurements (see
Chapter 3).
(iii) Due to the operation under ambient conditions a thin contamination layer will
have formed on the surface. It is well known that tunneling is not inhibited by a
contamination layer, and that Pt/Co multilayers are resistant to oxidation [54], Nev-
ertheless, the operation under ambient conditions adds uncertainty to the value of
the surface polarization. From the previous statements, we believe that the average
polarization of our sample surface should be more than an order of magnitude lower
than of pure Co; however at selected sites we assume that a reasonable upper limit
for the polarization $|\mathcal{P}(G_t)|$ is about 0.1 .

With this estimate, we deduce the semiconductor surface spin-splitting in the
following way. From the I-V curve depicted in Fig. 4.7 we deduce a tunnel barrier
conductance of $G_t \simeq 10^{-8} \, \Omega^{-1}$; using Eq.(4.6), the measured tunnel current modu-
lation of 4 pA, and the estimated upper limit for $|\mathcal{P}(G_t)|$ of 0.1 , we deduce that in
our experiment the value for the spin-splitting $(\Delta V_s^{\text{spin}})$ was 4 mV or larger (we pay
no attention to the sign of the polarization, since we did not calibrate the sign of
the helicity-dependence of the current). With a measured surface photovoltage of
0.1 V (cf. Fig. 4.7), we obtain a relative spin-splitting of $|\Delta V_s^{\text{spin}}/\overline{V}_s|=(4\pm3)\times10^{-2}$ or
larger. Note that this value is close to the experimental result obtained with the
planar junctions of Al_2O_3 and Co.

Photocurrent polarization. The polarization of the photoexited minority carrier cur-
rent $\mathcal{P}(J_p)$ arriving at the surface of our GaAs tip is determined by the magnitude
of the spin-polarization at excitation and the spin-relaxation during transport to the
semiconductor surface. In addition, optical refraction in the GaAs tip may reduce the
photocurrent polarization. These issues are addressed in the following.
(i) Theoretically, the absorption of circularly polarized gap-energy photons in GaAs
gives an electron spin-polarization of 0.5 [19]. Between creation and arrival at the
semiconductor surface, the photoexcited carriers suffer energy and spin relaxation.
For this reason, the spin-polarization of electrons photoemitted from GaAs (doping
$\sim10^{25} \, m^{-3}$) that is activated to negative electron affinity, usually ranges from 0.2 to
0.3 at room-temperature operation [58]. For photons with an energy larger than the
bandgap, the theoretical value of the spin-polarization at excitation is reduced and the
carriers suffer additional energy and spin relaxation before arrival at the semiconduc-
tor surface. For a photon energy of 1.96 eV (633 nm wavelength) the spin-polarization

of photoemitted electrons decreases by more than a factor of three when compared to the case where gap-energy (1.42 eV) photons are used [58, 59].

(ii) The optical polarization inside the GaAs is affected by the shape of the material. A rigorous calculation of the polarization-dependent penetration of optical waves into a semiconductor tip is complicated by the non-trivial geometry of the STM junction. By a simple calculation however, we can estimate an upper limit to the distortion of the optical polarization in the tunnel junction. Ideally, our cleaved GaAs tunneling tips have the shape of a regular tetrahedron, i.e. at the apex there is a three-fold rotational symmetry around the tip axis. If the tip axis is collinear with the optical propagation direction, then at the tip apex there is no asymmetry to linear or circular polarization; in other words, the polarization of the impinging light is conserved along the tip axis in the semiconductor material. However, because in an STM experiment also *lateral* minority carrier transport is involved (see Chapter 2 and the notion of an effective collection radius), the off-axis optical polarization is of importance. Off the tip axis, the local geometry is determined by the tip surface, of which the normal vector is at a large angle with the optical propagation direction: for our cleaved tips this angle amounts to 45°. We can easily calculate the optical penetration of a circularly polarized plane wave at an angle of 45° into GaAs [55], which shows that the reduction of the degree of circular polarization in the GaAs is only 12%.

(iii) When in GaAs circularly polarized photons with near-bandgap energy are absorbed, at a fixed location the average spin-orientation of the photoexcited electrons is normal to the plane of rotation of the electric vector, i.e. collinear with the optical propagation direction [7]. However, due to the optical refraction the propagation direction is not uniform in the GaAs tip. For a GaAs surface at an angle of 45°, the propagation direction of the transmitted beam is modified by an angle of $45° - 11° = 34°$ with respect to the incident beam [55]. In our experiment, the propagation direction of the incident beam (i.e. the sample normal) is a convenient spin-quantization axis, because the Pt/Co multilayer sample has its magnetic anisotropy along the same direction. In other words, due to the optical refraction the direction of the spin-orientation of photoexcited carriers deviates at most 34° from the quantization axis. Projection of the direction of the spin-polarization on the quantization axis gives a factor of $\cos(34°) = 0.83$, i.e. the modified optical propagation direction results in a reduction of the spin-polarization by 17%. In conclusion, from statements (i)-(iii) we deduce that a value of 0.1 represents an upper limit to the photocurrent polarization for our experimental situation.

   With the previously deduced value of the spin-splitting ($V_s^{spin} \geq 4 \, mV$), we calculate the spin-lifetime by using Eq.(4.10) of our model description. In our experiment, the illumination intensity was about $10^7 \, Wm^{-2}$, which implies that $J_p \simeq 5 \times 10^6 \, Am^{-2}$ (see Chapter 2); the density of surface states (D_{ss}) in the native oxide on GaAs is $10^{36} \, m^{-2}J^{-1}$ or larger [21, 25]. Using these values and $\mathcal{P}(J_p) \leq 0.1$, with Eq.(4.10) we deduce that the surface spin-lifetime (τ^{spin}) was 0.4 ns or larger in our experiment.

4.4.5 Conclusions

We have presented a dual-frequency modulation technique that allows for the detection of a spin-polarized tunneling signal due to optical spin-orientation in an STM configuration. A modulation of optical polarization not only generates a modulation of spin-orientation, but concurrently gives a modulation of the amount of photoexcited carriers. This can be caused by the magneto-optical Kerr/Faraday effect in the magnetic material, a low symmetry of the tunnel junction, or improper optical alignment. Thus, for the detection of spin-polarized tunneling it is prerequisite to tune the tunnel junction to a low sensitivity for unwanted variations of the optical intensity. In order to find the required parameters (e.g. applied voltage, tip-sample separation) we have to analyze the sensitivity to intensity variations by modulating the optical intensity (at a different frequency than the modulation of optical polarization). In a metal/semiconductor STM junction, this sensitivity strongly depends on the applied voltage, as was already pointed out in Chapter 2. By sweeping the applied voltage one can conveniently select the junction parameters such that spin-polarized tunneling can be detected.

Using a GaAs tip and a Pt/Co multilayer under ambient conditions, we delivered evidence for the possibility of spin-polarized tunneling by optical spin-orientation. The measured tunnel current modulation due to spin-polarized tunneling was $4\,\text{pA}$. The estimated spin-polarization of the tunneling conductance is 0.1 or lower in that experiment; with this estimation, the experimental observation implies that the spin-splitting at the semiconductor surface (V_s^{spin}) was $4\,\text{mV}$ or larger. According to our model and estimations, a spin-splitting of that size corresponds to a surface spin-lifetime of $0.4\,\text{ns}$ or larger.

Although we were not able to perform magnetic imaging, this should be possible by increasing the ratio of signal to noise; this may involve an optimization of the photon energy, the optical intensity, and the semiconductor surface preparation. Furthermore, it will be of importance to improve our knowledge of the spin-polarization in the semiconductor and in the magnetic material. With respect to the semiconductor, information on the polarization of the photoexcited carriers can be derived from measurements of polarized photoluminescence or spin-polarized photoemission; an improved definition of the surface electronic properties of the magnetic material can be achieved by preparation and *in situ* measurement of the sample in a well-controlled environment, such as an ultra-high vacuum.

4.5 General discussion and conclusions

In this Chapter we presented a model for spin-polarized transport in a photoexcited tunnel junction between a magnetic metal and a semiconductor, where the semiconductor charge carriers are polarized by optical orientation. The semiconductor surface

was described in terms of a spin-dependent distribution function or quasi Fermi level V_s^σ. The model clearly demonstrates that the spin-selective contribution to the total tunneling current is proportional to the product of the spin-dependence of the tunneling conductance $(G_t^\uparrow - G_t^\downarrow)$ and the spin-split quasi-Fermi level at the semiconductor surface $(V_s^\uparrow - V_s^\downarrow)$. The sensitivity of the total tunneling current is maximized in the photovoltaic mode of operation, i.e. when the tunnel current represents a negligible disturbance to the semiconductor. For that mode of operation, in a p-type material the spin-splitting at the semiconductor surface is proportional to the density and the polarization of the photoexcited electrons, to the surface spin-lifetime, and inversely proportional to the density of surface states.

Experimental results were shown for planar junctions as well as in an STM configuration. In both cases a technique of polarization modulation was employed, and the resulting tunnel current modulation was detected. A complication is that the current modulation is caused by optical spin-orientation and spin-dependent transmission over the tunnel barrier, *as well as* by a modulation of optical power absorbed in the semiconductor. The power modulation can for example be due to the magneto-optical Kerr/Faraday effect, which was at the basis of the experiments reported in Chapter 3. We explain that the separation of the two contributions can be established by varying the photon energy, the tunnel barrier width, and the applied voltage. From the experiments with planar junctions, an upper limit to the relative spin-splitting at the semiconductor surface $([V_s^\uparrow - V_s^\downarrow]/[V_s^\uparrow + V_s^\downarrow])$ was deduced to be 5%. In the STM experiment with a GaAs tip, the relative spin-splitting at the surface was 4% or larger; according to our model and estimations this corresponds to a spin-lifetime of 0.4 ns or larger.

Concerning the application of optical spin-orientation to magnetic imaging, it is of interest to estimate the importance of magnetic forces. In our experiments the maximum light intensity was of the order of $10^7\,\mathrm{Wm}^{-2}$. For 1.5 eV photons the absorption depth is about 1μm in GaAs [60]; if every photon yields one electron-hole pair, the photoelectron generation rate is 4×10^{31} electrons per second per m^3. In case of 50% spin-polarization and a lifetime of 10 ns, in the semiconductor this gives a maximum photo-induced magnetization of $2\times10^{23}\,\mu_B\,\mathrm{m}^{-3}$. This is equal to an average optically-induced magnetic moment of less than $10^{-5}\,\mu_B$ per atom. With such a low magnetization the resulting magnetic dipolar forces are negligibly small. It is more difficult to evaluate the size of an exchange force in an optically oriented metal-semiconductor tunnel junction, because of the nonequilibrium spin-dynamics involved. Concerning the spin-splitting at the semiconductor surface, from our experimental results we deduce that the spin-splitting V_s^{spin} (4 mV) is smaller than the surface photovoltage (0.1 V). Although a spin-splitting as high as 0.1 V may be achievable, this is still an order of magnitude smaller than the exchange splitting in Fe or Co. From the above estimates we conclude that the magnetic forces, in a tunnel junction between a ferromagnetic material and an optically-excited semiconductor, are small compared to the case of two magnetic counter electrodes.

Summarizing, optical spin-orientation in III-V semiconductors provides a unique opportunity to detect spin-polarized tunneling in an STM. This is mainly due to the fact that the spin-polarization in the semiconductor can be reversed by optical means. We successfully investigated this mechanism for spin-selectivity, in planar junctions as well as in an STM with a cleaved GaAs tip. In an ultra-high vacuum environment, with cleaved GaAs tips atomic imaging of a non-magnetic material was already demonstrated [15]. We firmly believe that magnetic imaging with subnanometer resolution is within reach, using optically oriented semiconductor tips in an STM. As was demonstrated in Chapter 3, with a similar experimental arrangement it is possible to perform magneto-optical near-field imaging. Magneto-optical interactions are sensitive to bulk magnetization, whereas spin-polarized tunneling is sensitive to the spin-dependence of the electron states at the sample surface. We demonstrated that the respective effects may be separated by their dependence on photon energy, tunnel barrier width, and bias voltage. Ideally, one would like to combine the two measurements, so as to be able to simultaneously measure sample topography, bulk magnetization, and surface spin-structure with (sub)nanometer resolution.

In the future, it will be important to perform measurements in a well-controlled environment, such as an ultra-high vacuum. This will allow for the preparation of well-defined magnetic surfaces, and for a better control of the density of states on the semiconductor surface. The influence of an applied magnetic field on the surface spin-splitting should be investigated [61]. It will be interesting to compare results of p-type and n-type GaAs; we expect important differences because the polarized electrons represent minority carriers in p-type material and majority carriers in n-type material [22, 23]. Besides GaAs also other III-V materials are candidates for spin-polarized tunneling; one example is InGaP [62], that is more stable (due to the presence of In), has a wider bandgap (due to P), but on the other hand has a lower spin-orbit splitting (due to P) when compared to GaAs. With opaque magnetic samples, irradiation can be accomplished from the side of the tip, or through the tip in case the tip shaft is transparent; the latter can for example involve a corner of a semiconductor membrane that is supported on glass.

References

1. R. Meservey and P.M. Tedrow, Phys. Rep. **238**, 173 (1994).
2. A review on STM can be found in: *Scanning tunneling microscopy I, II, and III*, edited by R. Wiesendanger and H.-J. Güntherodt, Springer series in surface science vol. 20, 28, and 29 (Springer Verlag, Heidelberg, 1992/93).

3. J.C. Slonczewski, Phys. Rev. **B39**, 6995 (1989); A.A. Minakov, and I.V. Shvets, Surf. Sci. Lett. **236**, L377 (1990); S.N. Molotkov, Surf. Sci. **261**, 7 (1992); D. Bürgler, and G. Tarrach, Ultramicr. **42**, 194 (1992).

4. J.S. Moodera, L.R. Kinder, T.M. Wong, and R. Meservey, Phys. Rev. Lett. **74**, 3273 (1995); T. Miyazaki and N. Tezuka, J. Magn. Magn. Mat. **139**, L231 (1995); and references therein.

5. R. Wiesendanger, H.-J. Güntherodt, G. Güntherodt, R.J. Gambino, and R. Ruf, Phys. Rev. Lett. **65**, 247 (1990).

6. S.F. Alvarado and Ph. Renaud, Phys. Rev. Lett. **68**, 1387 (1992).

7. *Optical orientation*, edited by F. Meier and B.P. Zakharchenya, Modern problems in condensed matter sciences vol. 8 (Elsevier, Amsterdam, 1984).

8. Japanese patent A62139240 (Hitachi Ltd), publication date 22 June 1987; European patent A0355241 (IBM Corporation), publication date 28 February 1990.

9. D.T. Pierce, Phys. Scr. **38**, 291 (1988).

10. W.T.M. Wolters, Master's thesis, University of Nijmegen, December 1988.

11. S.N. Molotkov, JETP Lett. **55**, 174 (1992).

12. R. Laiho and H.J. Reittu, Surf. Sci. **289**, 363 (1993).

13. H.J. Reittu, J. Phys.: Cond. Mat. **6**, 1847 (1994).

14. C. Hermann, H.-J. Drouhin, G. Lampel, Y. Lassailly, D. Paget, J. Peretti, R. Houdré, F. Ciccacci, H. Riechert, chapter 9 in *Spectroscopy of nonequilibrium electrons and phonons*, edited by C.V. Shank and B.P. Zakharchenya (Elsevier, Amsterdam, 1992) p. 397.

15. G. Nunes and N.M. Amer, Appl. Phys. Lett. **63**, 1851 (1993).

16. M.W.J. Prins, M.C.M.M. van der Wielen, R. Jansen, D.L. Abraham, and H. van Kempen, Appl. Phys. Lett. **64**, 1207 (1994).

17. R. Jansen, M.C.M.M. van der Wielen, M.W.J. Prins, D.L. Abraham and H. van Kempen, J. Vac. Sci. Technol. **B12**, 2133 (1994).

18. N.D. Lang, chapter 2 in: *Scanning tunneling microscopy III*, edited by R. Wiesendanger and H.-J. Güntherodt, Springer series in surface science vol. 29 (Springer Verlag, Heidelberg, 1992/93).

19. D.T. Pierce and R.J. Celotta, chapter 6 in Ref.[7].

20. R.K. Ahrenkiel, chapter 2 in *Minority carriers in III-V semiconductors: physics and applications*, edited by R.K. Ahrenkiel and M.S. Lundstrom, Semiconductors and semimetals vol. 39 (Academic Press, San Diego, 1993), p. 39.

21. H.H. Wieder, J. Vac. Sci. Technol. **17**, 1009 (1980), and other contributions in this issue.

22. M.I. Dyakonov and V.I. Perel, chapter 2 in Ref.[7].

23. In n-type GaAs, the optically oriented electrons (now the majority carriers) are swept into the semiconductor bulk by the subsurface electric field. Hence, in principle the semiconductor surface can become spin-polarized by *majority carrier* transport over the Schottky barrier.

24. E.H. Rhoderick and R.H. Williams, *Metal-Semiconductor Contacts*, Monographs

in electrical and electronic engineering No. 19 (Clarendon, Oxford, 1988).

25. M.S. Sze, *Physics of Semiconductor Devices* (Wiley Int., New York, 1981).

26. To first order, the contributions to the helicity-asymmetry of the tunnel current from spin-polarized tunneling and from the magneto-optical effect, linearly depend on the inproduct of the light helicity and the sample magnetization. As a result, these two contributions cannot be separated by modifying the optical polarization or the sample magnetization.

27. D.P. Woodruff and T.A. Delchar, *Modern techniques of surface science* (Cambridge Univ. Press, London, 1986).

28. A.J.J. Koch, P. Hokkeling, M.G. van der Steeg, and K.J. de Vos, J. Appl. Phys. **31S**, 75S (1960).

29. T. Sands, J.P. Harbison, M.L. Leadbeater, J.S.J. Allen, G.W. Hull, R. Ramesh and V.G. Keramidas, Appl. Phys. Lett. **57**, 2609 (1990).

30. G.A. Prinz, Phys. Rev. Lett. **54**, 1051 (1985).

31. A.Y. Liu and D.J. Singh, J. Appl. Phys. **73**, 6189 (1993).

32. J. De Boeck, C. Bruynseraede, H. Bender, A. Van Esch, W. Van Roy, and G. Borghs, MBE-conference (Osaka, Japan, 1994), to be published in J. Cryst. Growth.

33. R.P. Hunt, J. Appl. Phys. **38**, 1652 (1967); R. Atkinson, and P.H. Lissberger, J. Magn. Magn. Mat. **118**, 271 (1993).

34. W. Reim and J. Schoenes, in *Ferromagnetic Materials*, Vol. 5, edited by K.H.J. Buschow and E.P. Wohlfarth (Elsevier, Amsterdam, 1990), p. 134.

35. P.G. van Engen, K.H.J. Buschow, and M. Erman, J. Magn. and Magn. Mat. 30, 374 (1983).

36. P.B. Johnson and R.W. Christy, Phys. Rev. B6, 4370 (1972); *ibid.* B9, 5056 (1974).

37. M.W.J. Prins, D.L. Abraham, and H. van Kempen, J. Magn. Magn. Mat. **121**, 109 (1993); *ibid.*, Surf. Sci. **287/288**, 750 (1993).

38. E.L. Wolf, *Principles of electron tunneling spectroscopy* (Oxford Univ. Press, New York, 1985).

39. J. Kessler, *Polarized electrons*, Springer series on atoms and plasmas vol. 1 (Springer Verlag, Berlin, 1976).

40. In the convention described in Ref. [34], for Co and using radiation with a photon energy between 1.5 and 3 eV, the polar Kerr rotation and ellipticity are negative, and the Faraday rotation and ellipticity are positive (see for example K.H. Clemens and J. Jaumann, Z. Physik **173**, 135 (1963), or Ref. [35]). When the magnetic field is oriented in the propagation direction of the incident beam, this means that incident light of right-handed circular polarization is absorbed more strongly than light of left-handed circular polarization, where right(left)-handed circular polarization means that at a fixed location the electric vector rotates clockwise(counterclockwise) for an observer facing the optical beam. The radiation *helicity* is defined as the angular momentum with respect to a fixed quantiza-

tion axis. If the quantization axis is defined *opposite* to the propagation direction of the light, right(left)-handed circularly polarized light is of positive(negative) helicity.

41. W. Weber, D.A. Wesner, D. Hartmann, and G. Güntherodt, Phys. Rev. **B46**, 6199 (1992).

42. C. Carbone, E. Vescovo, O. Rader, W. Gudat, and W. Eberhardt, Phys. Rev. Lett. **71**, 2805 (1993).

43. τ-MnAl has a tetragonal crystal structure with $a=2.77$ Å and $c=3.54$ Å (space group 123 in the *International Tables* [44]). The Wyckoff positions a and d are occupied. The ratio of Mn to Al was taken to be 50/50. *Ab initio* localized-spherical-wave (LSW) bandstructure calculations [45] were performed using a scalar-relativistic Hamiltonian and including all core electrons. Local-density exchange-correlation potentials [46] inside space-filling, and therefore overlapping, spheres around the atomic constituents were used. In the construction of the LSW basis [45], the spherical waves were augmented by solutions of the scalar-relativistic radial equations indicated by the atomic-like symbols $3s$ and $3p$ for Al, and $4s$, $4p$ and $3d$ for Mn. In the internal l-summation for the augmentation of the central Hankel function at surrounding atomic sites one extra l-value was included, i.e. $3d$ orbitals were added on Al and $4f$ orbitals on Mn. About 150 degrees of freedom were used for screening the central Hankel functions, resulting in screening clusters with a size of 27 atoms. Iterations were performed with $\vec{k}$-points lying in the centers of simplexes filling an irreducible part of the first Brillouin zone. The volume per point was 2.6×10^{-7} Å^{-3}. Self-consistency was assumed when the changes in the local partial charges in each atomic sphere decreased to below 10^{-4}. Subsequently the densities of states were obtained by an analytical quadratic integration method [47] using the $\vec{k}$-points on the apices and mid-vertices of the simplexes.

44. *International Tables for Crystallography*, edited by T. Hahn, volume A: Space Group Symmetry (Reidel, Dordrecht, 1983).

45. H. van Leuken, A. Lodder, M.T. Czyżyk, F. Springelkamp, and R.A. de Groot, Phys. Rev. **B41**, 5613 (1990).

46. L. Hedin and B.I. Lundqvist, J. Phys. **C4**, 2064 (1971).

47. M.S. Methfessel, M.H. Boon, and F.M. Muller, J. Phys. **C20**, 1069 (1987).

48. The direction-sensitivity of tunneling through a planar barrier, is due to the fact that an electron with a large momentum parallel to the tunnel barrier (so with a large transverse kinetic energy) has a low penetration into the tunneling barrier [49]. Assume an electron with a wavevector that is at an angle α with respect to the sample normal. By simple plane-wave matching, it can easily be derived that the relative transmission probability through the tunnel barrier is given by: $T(\alpha)/T(\alpha=0) = \exp(-2d\Delta\kappa)$, where $\Delta\kappa$ equals $k^2\alpha^2/[2\kappa]$ to lowest order in α; d is the tunnel barrier width, and k is the wavevector of the impinging electron; for a square barrier κ is equal to $[2m\Phi_t/\hbar^2]^{1/2}$, where Φ_t is the tunnel

barrier height. Our experiment involves an AlAs barrier with a thickness (d) of 20 nm. AlAs has an energy gap of more than 2 eV, such that a tunnel barrier height (Φ_t) of 1 eV is a reasonable value; this yields $\kappa=5.2\,\mathrm{nm}^{-1}$. Assuming a wavevector $k=10\,\mathrm{nm}^{-1}$ for the impinging electron, we find that the relative transmission drops by a factor of ten for an angle of incidence (α) of 5°. This estimate is in agreement with the calculations of Ref. [49].

49. G. Beuermann, Z. Phys. B - Cond. Matt. **44**, 29 (1981)

50. G.W. Anderson, M.C. Hanf, and P.R. Norton, Phys. Rev. Lett. **74**, 2764 (1995); G.A. Prinz, Science **250**, 1092 (1990).

51. A. Moghadam, J.G. Booth, D.G. Lord, J. Boyle, and A.D. Boardman, IEEE Trans. Magn. **30**, 769 (1994); and references therein.

52. K. Sueoka, K. Mukasa, and K. Hayakawa, Jpn. J. Appl. Phys. **32**, 2989 (1993).

53. For a review on magneto-optical effects see: M.J. Freiser, IEEE Trans. Magn. **4**, 152 (1968).

54. W.B. Zeper, F.J.A.M. Greidanus, P.F. Garcia, and C.R. Fincher, J. Appl. Phys. **65**, 4971 (1989); W.B. Zeper, H.W. van Kesteren, B.A.J. Jacobs, J.H.M. Spruit, and P.F. Carcia, J. Appl. Phys. **70**, 2264 (1991). Our Pt/Co multilayers were prepared by H.W. van Kesteren, H.C. Donkersloot and J.M. Kerkhof at the Philips Research Laboratories, Eindhoven.

55. When an optical plane wave arrives at an abrupt interface (discrete change of refractive index from value N_1 to N_2), the relative Fresnel transmission coefficient for s-polarized light with respect to p-polarized light is given by: $\rho=t_s/t_p=[N_2\cos(\theta_1) + N_1\cos(\theta_2)]/[N_1\cos(\theta_1) + N_2\cos(\theta_2)]$, where θ_1 and θ_2 are the angles between the interface normal and the optical propagation direction in materials (1) and (2) respectively [56]. When the incident plane wave is circularly polarized, the ellipticity (ϵ) of the light transmitted into material (2) is given by: $\sin(2\epsilon)=2Im(\chi)/[1+|\chi|^2]$ [56], where $\chi=i\rho$. In case of an air-GaAs interface ($N_1=1$, $N_2\simeq3.7$ [60]) and an angle of incidence (θ_1) of 45° (which yields $\theta_2=11°$), we find that $\rho=0.83$ and $\epsilon=0.88\times\pi/4$. Since for circularly polarized light $\epsilon=\pi/4$, this calculation indicates the degree of circular polarization inside the GaAs is reduced by 12% when compared to the incident beam.

56. R.M.A. Azzam and N.M. Bashara, *Ellipsometry and polarized light* (North Holland, Amsterdam, 1987).

57. C. Kittel, *Introduction to solid state physics* (Wiley, New York, 1986).

58. H.-J. Drouhin, C. Hermann, and G. Lampel, Phys. Rev. **B31**, 3872 (1985).

59. D.T. Pierce and F. Meier, Phys. Rev. **B13**, 5484 (1976).

60. D.E. Aspnes and A.A. Studna, Phys. Rev. **B27**, 985 (1983).

61. G.E. Pikus and A.N. Titkov, chapter 3 in Ref.[7].

62. S.-H. Wei and A. Zunger, Appl. Phys. Lett. **64**, 1676 (1994).

Appendix A

Depletion field focusing*

This appendix deals with the traversal of minority carriers through a subsurface region of a semiconductor that is depleted of majority carriers. The carriers are assumed to have been excited outside the depletion region. In general the hot electron mean free path is one or two orders of magnitude smaller than the depth of the depletion region, such that in good approximation the minority carriers follow trajectories that are parallel to the direction of the electric field in the depletion region. We intend to investigate the dependence of the flux of collected carriers on the surface potential distribution, and on the surface shape. For this purpose we first consider a planar semiconductor with a non-constant potential on the surface at $z = 0$. A second exercise concerns a tip-shaped semiconductor with a constant potential on its curved surface. We do not intend to discuss the dependence of the surface potential distribution on the current. The calculations of this appendix were performed by A.P. van Gelder at the University of Nijmegen.

General. In order to calculate the electric field in the depletion region for a given surface potential, we should solve the Poisson equation:

$$\nabla^2 \Phi(x, y, z) = 1, \tag{A.1}$$

with a depletion region edge satisfying:

$$\Phi = 0, \text{ and } \nabla\Phi = 0. \tag{A.2}$$

Φ is defined in units $-[\epsilon_0\epsilon_r]^{-1}$ times the assumed homogeneous charge density in the depletion region. We neglect a small shift of the depletion region edge due to a nonzero temperature. The potential in the depletion region will be solved for a given

*Some of the results of this appendix were reported in *Depletion field focusing in semiconductors* by M.W.J. Prins and A.P. van Gelder, submitted.

potential distribution at the semiconductor surface, and requiring the existence of a depletion region edge with the combined constraints of Eq.(A.2). These boundary conditions generally give rise to nonlinear equations that are difficult to solve for an arbitrary surface potential and surface shape.

Planar semiconductor. For a flat surface with

$$\Phi(x, y, 0) = F_0 + F_1(x, y) , \tag{A.3}$$

where F_0 is constant, the solution of Eq.(A.1) is:

$$\Phi = \frac{1}{2}[z - w_0]^2 + \cosh(zp) F_1(x, y) + p^{-1}\sinh(zp) G(x, y) \tag{A.4}$$

$$\frac{1}{2}w_0^2 = F_0 \quad , \quad p^2 = -[\frac{\partial^2}{\partial x^2} + \frac{\partial^2}{\partial y^2}] ,$$

with p^2 equal to the negative transverse Laplace operator. The function $G(x, y)$ and the depletion region edge $w(x, y)$ are fixed by constrictions (A.2). These functions can be solved by means of a perturbation approach with respect to the strength of the potential modification $F_1(x, y)$ on the surface. The starting point for the perturbative approach is the unperturbed solution, i.e. the first term of Eq.(A.4): $\Phi_0(x, y, z) = [z - w_0]^2/2$. To succesive orders of F_1 the depletion region edge is given by:

$$z_w = w(x, y) = w_0 + w_1(x, y) + w_2(x, y) + \dots \tag{A.5}$$

A similar expansion is made for the function $G(x, y)$. Because p should not operate on $[z_w - w_0]$, the functions $\cosh(zp)$ and $\sinh(zp)$ are expanded as $\{1 + [z_w - w_0]^2p^2/2 + \dots\}\cosh(w_0p)$ and $\{[z_w - w_0]p + \dots\}\sinh(w_0p)$ respectively. Up to third order in $F_1(x, y)$, the contributions to the potential and the depletion region edge are given by:

$$
\begin{aligned}
\Phi_0 &= \tfrac{1}{2}[z - w_0]^2 & w_0 &= [2F_0]^{1/2} \\
\Phi_1 &= \frac{\sinh([w_0 - z]p)}{\sinh(w_0p)} F_1(x, y) & w_1 &= \frac{p}{\sinh(w_0p)} F_1(x, y) \\
\Phi_2 &= \frac{1}{2}\frac{\sinh(zp)}{\sinh(w_0p)} [w_1^2] & w_2 &= -\frac{1}{2}\frac{p}{\tanh(w_0p)} [w_1^2] \\
\Phi_3 &= \frac{\sinh(zp)}{\sinh(w_0p)} [w_1 w_2] & w_3 &= -\frac{1}{6}p^2[w_1^3] - \frac{p}{\tanh(w_0p)} [w_1 w_2]
\end{aligned} \tag{A.6}
$$

In order to calculate the minority carrier trajectories in the depletion field, we assume that $F_1(x, y)$ is a function of the radial coordinate $r = [x^2 + y^2]^{1/2}$. We define the focusing efficiency η_f as:

$$\eta_f \equiv \lim_{r \to 0} \frac{r^2(w)}{r^2(0)} , \tag{A.7}$$

where $r(z)$ represents the minority carrier trajectory in the depletion field. The efficiency describes how, by following the electric field, an infinitesimal area dA at $\vec{r} = \vec{0}$ is mapped onto an area $\eta_f \, dA$ at the edge of the depletion region. In the limit of $r \to 0$, the logarithm of the focusing efficiency can conveniently be expressed as:

$$\ln(\eta_f) \ = \ 2 \int_0^w dz \, q(z) \ , \quad \text{with} \quad q(z) = \frac{1}{r} \frac{dr}{dz} = \frac{1}{r} \frac{\partial \Phi / \partial r}{\partial \Phi / \partial z} \ , \quad \text{(A.8)}$$

where $q(z)$ is the inverse radius of curvature of the equipotential planes as they intersect the z-axis. To first order $q(z)$ is equal to $p^2 / 2 \, \Phi_1 / [w_0 - z]$. To quantify the focusing properties of the depletion field, let's consider a potential perturbation of Gaussian shape:

$$F_1(r) = f_1 F_0 \exp(-r^2 / \delta^2) \ , \qquad \text{(A.9)}$$

with a Gaussian width δ, and a relative amplitude f_1. The resulting first order approximation to $q(z)$ gives rise to the following expression for $\ln(\eta_f)$:

$$\ln(\eta_f) \ = \ \frac{1}{4} \frac{f_1}{\lambda^2} \int_0^\infty dk \, k^3 \frac{\exp(-k^2/4)}{\sinh(k/\lambda)} \int_0^{k/\lambda} dv \frac{\sinh(v)}{v} \ , \quad \text{with} \quad \lambda = \delta / w_0 \ . \ \text{(A.10)}$$

Proportionality with f_1 results from the linearity of the approximation. The results of a numerical integration to within 3×10^{-4} accuracy are given by:

$$\lambda < 1/2 \ : \ \ \ln(\eta_f)/f_1 = \sqrt{\pi}/[2\lambda] \frac{1 - c_1 \lambda + c_2 \lambda^2}{1 - c_3 \lambda + c_4 \lambda^2}$$

$$c_1 = 0.621103, \ c_2 = 4.316068, \ c_3 = 1.176367, \ c_4 = 3.593267$$

$$\lambda > 1/2 \ : \ \ \ln(\eta_f)/f_1 = \ 2/[\lambda^2] \frac{d_1 + d_2 \lambda^2 + \lambda^4}{d_3 + d_4 \lambda^2 + \lambda^4} \qquad \text{(A.11)}$$

$$d_1 = 0.042244, \ d_2 = 1.026517, \ d_3 = 0.668438, \ d_4 = 1.909611$$

These results are plotted in Fig. 2.3 of section 2.2.2.

Tip-shaped semiconductor. To determine the depletion region in a tip-shaped semiconductor, we model its surface as a (rotation) paraboloid:

$$z \ = \ r^2 / [2 r_c] \ , \qquad \text{(A.12)}$$

with a radius of curvature r_c at the tip apex, where $r = 0$ and $z = 0$. The potential on this paraboloid surface is assumed constant of value F_0. The shape of the depletion region and the potential within it are determined by Eqs.(A.1) and (A.2). Quantum confinement effects are neglected [see for example K. Hiruma, M. Yazawa, T. Katsuyama, K. Ogawa, K. Haraguchi, M. Koguchi, and H. Kakibayashi, J. Appl. Phys. **77**, 447 (1995)].

For what follows, use is made of paraboloid coordinates x and y defined by:

$$xy = -r^2/r_c^2 \quad , \quad \text{and} \quad 1 + x + y = 2z/r_c \ , \tag{A.13}$$

not to be confused with the Cartesian ones. The focus point of the paraboloid is given by $(x, y) = (0, 0)$, i.e. by $r = 0$ and $z = r_c/2$. With the paraboloid coordinates Eq.(A.1) transforms into:

$$\frac{\partial}{\partial x}\left\{ x \frac{\partial \Phi}{\partial x} \right\} - \frac{\partial}{\partial y}\left\{ y \frac{\partial \Phi}{\partial y} \right\} = \frac{r_c^2}{4}[x - y] \ . \tag{A.14}$$

The interior of the paraboloid (the semiconductor material) is mapped onto the strip: $x \geq 0$ and $-1 \leq y \leq 0$. The semiconductor surface is given by $y = -1$, for which $\Phi = F_0$. We may use the following expansion for the potential:

$$\Phi = F_0 S^2 + \sum_{m=1}^{N} f_m(x) S^m[1 - S] \ , \tag{A.15}$$
$$\text{with} \quad S = S(x, y) = 1 - [1 + y]/s(x) \ ,$$

where $S(x, y)$ equals unity on the semiconductor surface, and equals zero on the line defined by: $y = -1 + s(x)$, where $0 < s(x) \leq 1$. Note that $s(x)$ defines a line where the potential vanishes; this line is not necessarily the depletion region edge, because for a depletion region edge the derivatives of the potential should be zero also. For given boundary values of Φ on a given surface, the functions $f_m(x)$ may be resolved by making use of a variational method for solving Eq.(A.14). After having applied the variational method it is permitted to introduce the boundary condition $\partial \Phi/\partial x = \partial \Phi/\partial y = 0$ for the depletion region edge, by imposing the constraint: $f_1(x) = 0$. Before explaining the principle of the variational method, it is instructive to consider the expansion of Eq.(A.15) involving terms to third order in S:

$$\hat{\Phi} = F_0 S^2 + \hat{f}(x) S^2[1 - S] \tag{A.16}$$

as a non-variational approximation for Φ. This function satisfies the boundary conditions on the surface and on the depletion region edge, but it is only an approximate solution of Eq.(A.14) inside the depletion region. On the surface $(y = -1)$ it follows from Eq.(A.14) that $\partial/\partial y\{y\partial \Phi/\partial y\}$ equals $-r_c^2/4\,[1 + x]$. This implies that:

$$\hat{f}(x) = 2F_0 \frac{1 + s(x)}{4 + s(x)} - r_c^2/4\,[1 + x] \frac{s^2(x)}{4 + s(x)} \ . \tag{A.17}$$

A special point is defined by the position at which the depletion region edge intersects the z-axis. This so-called intersection point corresponds with $(x, y) = (x_i, y_i)$, where $x_i = 0$ or $y_i = 0$. At the tip apex, the depth of the depletion region (w) is related to the

intersection point as $w = [1 + x_i + y_i]r_c/2$. The intersection point is located on the y-axis if $w < r_c/2$ (the focus point of the paraboloid), or is located on the the x-axis if $w > r_c/2$. In the first case, Eq.(A.14) yields that $\partial^2 \Phi/\partial y^2 = r_c^2/4$ at the intersection point. This implies that $2F_0 + 2\hat{f}(0)$ equals $r_c^2 s^2(x)/4$, or:

$$F_0 = w^2/2 \frac{1 + [w/r_c]/3}{1 + [w/r_c]} \,, \quad \text{if } x_i = 0 \,. \tag{A.18}$$

The range of F_0-values is limited to $F_0/r_c^2 < 7/72$, when the focus point of the paraboloid is reached. For small values of F_0 or of w, Eq.(A.18) gives: $F_0 = w^2/2 \left[1 - 2/3 \left[w/r_c\right] + 2/3 \left[w/r_c\right]^2 - \ldots\right]$. The first two terms on the right hand side are equal to the exact expression for a tangential sphere with radius r_c.

We now consider the second case, for which the intersection point is located on the x-axis at $(x_i, 0)$. The expansion for Φ given in Eq.(A.15), or the approximate expression in Eq.(A.16), may still be considered to be valid for $x > x_i$. For $0 \le x \le x_i$ the general solution of Eq.(A.14) is:

$$\Phi = F_0 - [1 + x][1 + y]\, r_c^2/4 + \sum_{n=1}^{\infty} c_n\, P_n(x) P_n(y) \,. \tag{A.19}$$

The functions $P_n(y)$ are eigenfunctions of:

$$\frac{\partial}{\partial y} \left\{ y \frac{\partial P_n}{\partial y} \right\} = E_n\, P_n(y) \quad, \quad \text{with } P_n(-1) = 0 \,. \tag{A.20}$$

The $P_n(y)$ functions are orthogonal in the domain $-1 < y < 0$, and equal to the 0th-order Bessel functions $J_0([-4E_n y]^{1/2})$. The factors $4E_n$ are equal to the square of its nth root. For $P_n(x)$ we are dealing with the modified Bessel functions $I_0([4E_n x]^{1/2})$ because x is positive. These functions increase monotonously with increasing x. The coefficients c_n follow from a projection of Eq.(A.19) and the approximate solution (A.16) on the orthogonal functions $P_n(y)$. The unknown x_i follows from the requirement that $\partial \Phi/\partial x$ must vanish at $(x_i, 0)$. This results in the following transcendental equation for x_i:

$$\sum_{n=1}^{\infty} \frac{P_n'(x_i)}{P_n(x_i)} \frac{P_n(0)}{P_n'(-1)} \left\{ [4F_0/r_c^2][E_n^{-2} - E_n^{-1}] + \right. \tag{A.21}$$

$$\left. [1 + x_i]/4\, E_n^{-1} + F_0^{-1}\, \hat{f}(x_i)\, [36E_n^{-3} - 32E_n^{-2} + 5E_n^{-1}] \right\} = \frac{1}{4} \,.$$

This equation was solved for the range $0.1 \le F_0/r_c^2 \le 3$. With 10^{-3} accuracy, the results can be summarized by the following numerical approximation for $w = [1 + x_i]r_c/2$, i.e. for the z-value at which the depletion region edge intersects the z-axis:

$$F_0 = c_1 w^2 \frac{1 + c_2[w/r_c]}{1 + [w/r_c] + c_3[w/r_c]^2} \,, \tag{A.22}$$

where $c_1=0.5537520$, $c_2=0.0281201$, and $c_3=0.0215055$. The depletion region edge passes through the focus point of the paraboloid if $F_0 \simeq 0.094\,r_c^2$. For a spherical semiconductor as well as for a paraboloid-shaped semiconductor tip, the results are plotted in Fig. 2.4A of section 2.2.2, where w is normalized to the depletion region depth in a planar semiconductor: $w_0 = [2F_0]^{1/2}$. Since in the paraboloid tip the potential is known for $x \le x_i$, we are in the position to calculate the focusing efficiency with the aid of Eq.(A.8), by substituting for $q(z)$:

$$q = \frac{1}{r_c}\,\frac{\partial\Phi/\partial x - \partial\Phi/\partial y}{x\,\partial\Phi/\partial x - y\,\partial\Phi/\partial y}\,. \tag{A.23}$$

The values for $q(z)$ appear to be close to $-1/r_c$ for the considered range of F_0. Equipotential planes, intersecting the z-axis, hence appear to have a curvature that is close to (in fact larger than) the curvature of the paraboloid. To within an error of 10^{-3} the results are given by:

$$\ln(\eta_f) = -c_1\left\{[F_0/r_c^2 - c_2] + \big[[F_0/r_c^2 - c_2][F_0/r_c^2 + c_3]\big]^{1/2}\right\}, \tag{A.24}$$

where $c_1=1.328409220$, $c_2=0.0334509$, and $c_3=6.2078081$. For a spherical semiconductor the exact expression for the focusing efficiency is given by $\eta_f = [1-w/r_c]^2$. The results are plotted in Fig. 2.4B of section 2.2.2.

In a paraboloid tip the potential and the depletion region edge can be systematically determined in the following way. For a given zero-potential line, defined by the function $s(x)$, the potential can be solved with Eq.(A.15) in the domain $x > x_i$, and with Eq.(A.19) for $x < x_i$. Continuity of the potential at $x = x_i$ can serve to determine the relation of the coefficients c_n and the (left) derivative $\partial\Phi/\partial x$, with the functions $f_m(x)$ and their derivatives at $x = x_i$. This matching procedure is generally refered to in terms of the Green's functions for the domain $x < x_i$ and for the domain $x > x_i$. The chosen zero-potential line represents a genuine depletion region edge if on that line the solution for the potential satisfies the requirement that $\partial\Phi/\partial x = \partial\Phi/\partial y = 0$. This is the case if $f_1(x) = 0$. The condition that $f_1(x)$ vanishes is generally inconsistent, except for a uniquely chosen function $s(x)$ and its corresponding intersection point. The constituent equations for the functions $f_m(x)$ of Eq.(A.15) are obtained in the following way. Substitute into Eq.(A.14) the expression for Φ of Eq.(A.15), and multiply the resulting equation with $S^n[1-S]$, with $n=1,2,\cdots,N$. Integration of these N equations over the depth of the depletion region ($0 < S < 1$) results in a set of N coupled linear differential equations for the N functions $f_n(x)$. With the aid of variation calculus it can be proven that the thus found solution for Φ can be improved in a systematic way by increasing N. Necessary for the proof is that we project the equation upon the same set of functions $S^n[1-S]$ that belong to the expansion. The function $S[1-S]$ belongs to this set if $f_1(x)$ is not a priori zero. The equation

corresponding to this requirement is needed in order to find the zero-potential line that is also the depletion region edge. Substitution of $f_1(x) = 0$ into this equation gives rise to a non-linear partial differential equation for $s(x)$ of second order. This is connected with the fact that the coefficients of the (projected) equations for $f_m(x)$ are not constants, but functions of x, $s(x)$, or of the first and second derivatives of $s(x)$.

Appendix B

High-frequency modeling of a tunnel junction

In this appendix we describe a convenient formalism to calculate currents and voltages in an electronic system that contains *time-dependent* electronic components. This is an extension of the standard response theory that describes *time-invariant* electronic components (see standard textbooks such as P. Horowitz, and W. Hill, *The art of electronics*). For all observables and operators we adopt the discrete Fourier notation, e.g. for the current:

$$I(t) = \sum_{\omega=-\infty}^{\infty} I^\omega e^{j\omega t} , \tag{B.1}$$

where $j = \sqrt{-1}$. It follows from I(t) being real that $I^{-\omega} = [I^\omega]^*$. Electronic components are represented as operators, e.g. the admittance operator $\hat{Y}$ gives the current through a time-dependent admittance as a function of the potential drop V: $I(t) = \hat{Y}(t)V(t)$. The real part of $\hat{Y}$ describes the direct currents, the imaginairy part takes account of the displacement currents. In the frequency domain we will use the following definition:

$$\hat{Y}^{\omega_1} V^{\omega_2} = Y^{\omega_1}(\hat{\omega})V^{\omega_2} = Y^{\omega_1}(\omega_2)V^{\omega_2} \tag{B.2}$$

Note that the upper index ω refers to the ω-component in the frequency spectrum of a time-dependent variable. On the other hand, $\hat{\omega}$ is an operator, and as such assumes the value of the frequency of the component that $\hat{Y}$ acts upon. Using this definition, we derive the following expression for the current:

93

$$I(t) = \sum_{\omega} I^{\omega} e^{j\omega t} \quad = \quad \sum_{\omega_1 \omega_2} \hat{Y}^{\omega_1} V^{\omega_2} e^{j[\omega_1 + \omega_2]t} = \sum_{\omega} \left\{ \sum_{\omega_1} Y^{\omega_1}(\omega - \omega_1) V^{\omega - \omega_1} \right\} e^{j\omega t}$$

$$\rightarrow \quad I^{\omega} \quad = \quad \sum_{\omega_1} Y^{\omega_1}(\omega - \omega_1) V^{\omega - \omega_1} \tag{B.3}$$

As we can see, I consists of frequencies that are sums and differences of frequencies present in Y and V.

Attention should be paid to the fact that direct currents are driven by a drop of electrochemical potential, whereas displacement currents are caused by a drop of electrostatic potential. The respective electrical potentials are unequal in case of workfunction differences or a finite density of states of the electrodes. In case this issue is not of importance, a time-dependent conductance $G(t)$ parallel to a time-dependent capacitance $C(t)$ gives the following operator:

$$I(t) \quad = \quad GV + \frac{d}{dt}(CV) \quad = \quad \left[G + \frac{dC}{dt} \right] V + C \frac{dV}{dt}$$

$$\rightarrow \quad \hat{Y}^{\omega} \quad = \quad Y^{\omega}(\hat{\omega}) \quad = \quad [G^{\omega} + j\omega C^{\omega}] + j\hat{\omega} C^0 \tag{B.4}$$

To illustrate the use of the outlined formalism, we analyse the circuit of a current source I_0 connected to two admittances Y_1 and Y_2 in parallel. We define V to be the voltage that develops over the admittances. From Eq.(B.3), to first order in ω we find for the current I_i through the admittance Y_i:

$$I_i^{\omega} \quad = \quad Y_i^{\omega}(0)V^0 + Y_i^0(\omega)V^{\omega} , \quad i \in \{1, 2\} . \tag{B.5}$$

Using $I_0 = I_1 + I_2$ and solving for V^{ω}, we obtain the following expression for I_1^{ω}:

$$I_1^{\omega} \quad = \quad \frac{Y_1^0(\omega)}{Y_1^0(\omega) + Y_2^0(\omega)} \left[I_0^{\omega} - Y_2^{\omega}(0)V^0 \right] + \frac{Y_2^0(\omega)}{Y_1^0(\omega) + Y_2^0(\omega)} Y_1^{\omega}(0)V^0 \tag{B.6}$$

This equation gives the modulation of the current through admittance Y_1 due to the simultaneous modulation of I_0, Y_1 and Y_2. In a similar way we can find the modulation of current in a photoexcited metal-semiconductor tunnel junction, where now I_1^{ω} is the modulation of current flowing from the metal to the semiconductor, $Y_1^0(\omega)$ is the time-independent tunnel barrier admittance, $Y_2^0(\omega)$ is the time-independent Schottky barrier admittance, and I_0^{ω} is the modulation of photocurrent. $Y_2^{\omega}(0)$ is zero because the Schottky admittance is not time-dependent. V^0 is the time-averaged voltage across the tunnel barrier. In the constricted current channel (cf. Fig 2.5) $Y_1^{\omega}(0)$ is nonzero because of the tunnel gap modulation due to thermal expansion. In the wide current channel $Y_1^0(\omega)$ is purely imaginairy and $Y_1^{\omega}(0)$ can be neglected.

Summary

The scanning tunneling microscope (STM) is a suitable tool for the investigation of the atomic structure of surfaces. However, for more than a decade there has been a serious quest for a convenient magnetically sensitive version of the STM. This thesis describes how that goal can be reached with optically excited semiconductor tips, that can operate (i) as a local photodetector for near-field magneto-optical Faraday/Kerr imaging, and (ii) as a source of polarized electrons for spin-polarized tunneling.

Chapter 2 describes a model as well as experiments on the electrical properties of a photoexcited tunnel junction between a metal and a semiconductor material, as is established in an STM. The model treats the case that (non spin-polarized) carrier transport is mediated by capture and relaxation in the semiconductor surface states. In the semiconductor, majority carrier transport is determined by thermionic emission over the Schottky barrier and subsequent surface recombination. By optical excitation an additional minority carrier current is generated. The voltage that develops on the semiconductor surface is determined by the balance between majority and minority carrier current in the semiconductor, and the current across the tunnel barrier. Model calculations of the (non-planar) band-bending profile in the semiconductor are presented, that indicate that the subsurface electric field operates as an electrical lens that can focus or defocus the current.

Measurements were performed with moderately doped GaAs tips and samples prepared by cleavage. Continuous as well as modulated photoexcitation was used. Relationships were determined between tunnel current, applied voltage, incident optical power and tip-sample distance. The experimental results are well described by the model that includes carrier capture in the surface states. It is shown that the sensitivity of the tunnel current to small variations in optical power is determined by the ratio of the tunnel barrier conductance to the Schottky barrier conductance.

In the experiments of Chapter 3, the photosensitive cleaved GaAs tips were used for magneto-optical near-field imaging. In an STM, both the surface topography and the polarization-dependent optical transmission of a magnetic sample were measured.

Images of magnetic bits written in a Pt/Co multilayer are presented, where the magnetic contrast is achieved by detection of the Faraday effect. A magneto-optical lateral resolution of 250 nm is demonstrated; from the model description of Chapter 2 it is predicted that the lateral resolution can be further improved by more than an order of magnitude.

Chapter 4 deals with a model as well as experiments on spin-polarized tunneling. This involves tunnel junctions between a magnetic material and GaAs, where the latter is optically excited with circularly polarized light in order to generate spin-polarized carriers. As in the (non-polarized) transport model of Chapter 2, account is taken of carrier capture in the semiconductor surface states. It is proposed to describe the semiconductor surface in terms of the spin-dependent energy distribution function, the so-called surface spin-splitting. This can be calculated from the balance between the polarized electron and hole flow in the semiconductor subsurface region, the polarized tunneling current across the tunnel barrier between the magnetic material and the semiconductor surface, and the spin-relaxation at the semiconductor surface.

Measurements are presented on the circular-polarization-dependent photocurrent (the so-called helicity-asymmetry) in thin-film $Co/Al_2O_3/GaAs$ junctions. In the absence of a tunnel barrier, the helicity-asymmetry is caused by magneto-optical effects (magnetic circular dichroism). In case a tunnel barrier is present, the data cannot be explained by magneto-optical effects only; the deviations provide evidence that spin-polarized transmission due to optical spin-orientation occurs. In Co/τ-MnAl/AlAs/GaAs junctions deviations from the magneto-optical effects are observed, most probably due to the weak spin-polarization of τ-MnAl along the tunneling direction.

Also data are presented that are obtained in an STM with a GaAs tip and a Pt/Co multilayer sample under ambient conditions. A helicity-asymmetry of tunnel current was found with a size of 4 pA, which was verified not to be due to variations of the optical power. According to the model and estimations, this observation can be explained by spin-polarized tunneling, with a lower limit to the semiconductor surface spin-splitting and spin-lifetime of 4 mV and 0.4 ns respectively.

In conclusion, it is demonstrated that photoexcited semiconductor tips in an STM can be used for magneto-optical near-field imaging. In addition, evidence is presented that by optical spin-orientation in a GaAs tip a sufficiently high carrier polarization can be created to study spin-dependent electron tunneling to a magnetic surface. Both techniques have a high potential for wide-spread application to magnetic imaging, because: (i) the semiconductor probes are non-magnetic, so non-perturbing to the sample magnetization, (ii) the tips can operate under ambient conditions and with an applied magnetic field, and (iii) the lateral magnetic resolution can in principle be about ten nanometers for the magneto-optical effect, and of atomic magnitude for spin-polarized tunneling.

Samenvatting

De zogenaamde scanning tunneling microscoop (STM) is een geschikt instrument voor
het onderzoeken van de atomaire structuur van oppervlakken. Reeds langer dan tien
jaar wordt er naarstig gezocht naar een versie van de STM die gevoelig is voor mag-
netisme. Dit proefschrift beschrijft hoe dat doel bereikt kan worden met optisch
geëxciteerde halfgeleidende tips, die kunnen functioneren (i) als een lokale lichtdetec-
tor voor het maken van magneto-optische Faraday/Kerr afbeeldingen, en (ii) als een
bron van spin-gepolariseerde electronen voor spin-selectief tunnelen.

In hoofdstuk 2 worden een model en experimenten beschreven met betrekking tot de
foto-electrische eigenschappen van een tunneljunctie tussen een metaal en een halfge-
leider, zoals gemaakt in een STM. Het model beschrijft het geval dat het (ongepolari-
seerd) ladingtransport plaatsvindt via de oppervlaktetoestanden van de halfgeleider.
Het transport van meerderheidsladingdragers in de halfgeleider wordt bepaald door
thermionische emissie over de Schottky barrière en oppervlakterecombinatie. Opti-
sche excitatie genereert een additionele stroom van minderheidsladingdragers. De
spanning die op het halfgeleideroppervlak ontstaat, wordt bepaald door de balans
tussen de stroom van meer- en minderheidsladingdragers, en de stroom door de tun-
nelbarrière. Berekeningen aan het niet-planaire band-buigingprofiel in de halfgeleider,
tonen aan dat het electrisch veld als een lens functioneert die de stroom kan focusse-
ren of defocusseren.
Metingen zijn uitgevoerd met gekliefde GaAs tips en preparaten. Zowel een con-
stante als een gemoduleerde lichtexcitatie is gebruikt. Relaties zijn vastgesteld tussen
de tunnelstroom, de aangelegde spanning, het lichtvermogen en de afstand van de
tip tot het preparaat. De experimentele resultaten worden goed door het model met
oppervlaktetoestanden beschreven.

In de experimenten van hoofdstuk 3 zijn de optisch geëxciteerde gekliefde GaAs tips
gebruikt om magneto-optische nabij-veld afbeeldingen te maken. In een STM worden
zowel de topografie van het oppervlak als de polarisatie-afhankelijke optische trans-
missie van een magnetisch preparaat gemeten. Afbeeldingen worden getoond van

magnetische bits in een Pt/Co multilaag, waarbij het magnetische contrast via het Faraday effect wordt verkregen. Een magneto-optische laterale resolutie van 250 nm is aangetoond; het model van hoofdstuk 2 voorspelt dat de resolutie verbeterd kan worden met meer dan een orde van grootte.

Hoofdstuk 4 beschrijft zowel een model als experimenten met betrekking tot spin-gepolariseerd tunnelen. Dit gebeurt in een tunnel junctie tussen een magnetisch materiaal en GaAs, waarbij in het GaAs een spin-polarisatie gecreëerd wordt met circulair gepolariseerd licht. Net als in het model van hoofdstuk 2 wordt de invloed van de oppervlaktetoestanden in rekening gebracht, nu met een spin-afhankelijk bezetting. De laatste volgt uit de balans tussen de gepolariseerde electronen- en gatenstroom, de gepolariseerde tunnel stroom, en spin-relaxatie aan het halfgeleideroppervlak.

Metingen worden getoond met betrekking tot de afhankelijkheid van de tunnelstroom van de circulaire lichtpolarisatie (de zogenaamde heliciteitsasymmetrie) in dunne-film $Co/Al_2O_3/GaAs$ juncties. Zonder tunnel barrière wordt de heliciteitsasymmetrie gegeven door magneto-optische effecten (magnetisch circulair dischroisme). In geval van een tunnelbarrière kunnen de metingen niet alleen met magneto-optische effecten verklaard worden; de afwijkingen zijn een aanwijzing voor het optreden van spin-selectief tunnelen ten gevolge van optische spin-oriëntatie. In Co/τ-MnAl/AlAs/GaAs juncties zijn geen afwijking van de magneto-optische effecten waargenomen, waarschijnlijk wegens de lage spin-polarisatie van τ-MnAl langs de tunnelrichting.

Ook worden data getoond van een STM met een GaAs tip en een Pt/Co multilaag onder atmosferische condities. Een heliciteitsasymmetrie van de tunnelstroom is gevonden ter grootte van 4 pA, waarvan werd aangetoond dat deze niet voorkwam uit een modulatie van de optische intensiteit. Volgens ons model en enkele schattingen kan deze meting verklaard worden met spin-gepolariseerd tunnelen, bij een ondergrens voor de spin-splitsing en spin-levensduur aan het halfgeleider oppervlak van respectievelijk 4 mV en 0.4 ns.

Concluderend is aangetoond dat halfgeleidende tips in een STM gebruikt kunnen worden om magneto-optische nabij-veld afbeeldingen te maken. Bovendien zijn er aanwijzingen gevonden dat door optische spin-oriëntatie in een GaAs tip een voldoende grote polarisatie van ladingdragers gemaakt kan worden om spin-gepolariseerd transport naar een magnetisch oppervlak te meten. Beide principes kunnen in de toekomst van grote betekenis zijn als magnetische afbeeldingstechniek, omdat (i) de halfgeleider tips niet magnetisch zijn, en dus de magnetisatie van het preparaat niet beïnvloeden, (ii) de tips onder atmosferische omstandigheden en onder het aanleggen van een extern magnetisch veld kunnen functioneren, en (iii) de laterale magnetische resolutie in principe een tiental nanometers kan zijn voor het magneto-optische effect, en van atomaire grootte voor spin-gepolariseerd tunnelen.

Voor niet-natuurkundingen

De in dit boek beschreven experimenten en theorievorming hebben tot doel een techniek te ontwikkelen die magnetisme zichtbaar kan maken op de schaal van een miljardste meter (een nanometer). Op deze plaats wil ik graag in zo eenvoudig mogelijke bewoordingen uitleggen wat de achtergronden zijn van dit werk; om precies te zijn zal ik toelichten wat magnetisme is, waarom een hoog scheidend vermogen van belang is, en waarop de door ons ontwikkelde afbeeldingstechniek gebaseerd is.

Magnetisme. Iedereen heeft wel een bepaalde voorstelling van magnetisme. Je kunt denken aan het magnetische veld van de aarde dat je kunt gebruiken om de richting te bepalen met behulp van een kompas, of aan de magneetblokjes waarmee je iets op de koelkast kunt plakken. Iets meer achter de schermen speelt magnetisme een zeer belangrijke rol op het gebied van de informatie-opslag: de muziek- en videocassette, de floppy-disc en de harde schijf zijn alle gebaseerd op magnetische materialen. Magnetisme heeft te maken met de beweging van electrische deeltjes, de zogenaamde electronen. Dit kunnen we met een eenvoudig proefje toelichten: met een electrische stroom in een spoel (een gewikkelde metaaldraad) kunnen we een magnetische stof zoals ijzer aantrekken. IJzer op zich is magnetisch omdat er in het ijzer een continue draaibeweging van electronen plaatsvindt. We moeten dan wel bedenken dat een stuk ijzer uit ontzettend veel electronen bestaat, die alle een klein kringstroompje met een uitgebreidheid van ongeveer een miljardste meter belichamen.

Magnetische ordening. Net zoals een kompasnaald zich richt in het magnetische veld van de aarde, zo oriënteert elk klein draaiend ijzerelectron zich door het magnetische krachtenspel met de omgevende electronen. Met andere woorden, door de magnetische krachten gaan de electronen zich ten opzichte van elkaar ordenen. Het is meestal niet gemakkelijk te begrijpen hoe de vele electronen in een magnetisch materiaal zich zullen ordenen. Gaan ze met kop aan staart zitten, of kop-kop en staart-staart? Wordt het een overzichtelijke zichzelf repeterende structuur, of juist een totale wanorde? Gaan er verschillende groepen ontstaan (zogenaamde domeinen) en hoe groot zijn die dan? Kortom, om te begrijpen hoe een magnetische stof in elkaar zit, is het belangrijk om de magnetische ordening van de electronen te bepalen.

Magnetische gevoeligheid. Licht kan op verschillende manieren gepolariseerd zijn. Dit kun je eenvoudig inzien door twee Polaroid glaasjes ten opzichte van elkaar te draaien: in het ongunstige geval staan de polarisatierichtingen loodrecht op elkaar en laten de Polaroid glaasjes geen licht door; zijn de polarisaties parallel dan wordt het licht probleemloos doorgelaten. Het blijkt zo te zijn dat de polarisatie van licht gekoppeld is aan de magnetische oriëntatie van electronen in een materiaal: de mate van lichtabsorptie in een materiaal hangt af van de lichtpolarisatie en de magnetische ordening; evenzo kun je met gepolariseerd licht de magnetische oriëntatie van electronen beinvloeden. Kortom, door een geschikte lichtpolarisatie te kiezen kun je electronen met een bepaalde oriëntatie selecteren.

Microscopie op de miljardste meter. Met de in 1982 uitgevonden Scanning Tunneling Microscoop (STM) is het mogelijk om electronen aan het oppervlak van een materiaal zichtbaar te maken met een scheidend vermogen hoger dan een miljardste meter. Dit is 1000× hoger dan wat met een normale optische microscoop mogelijk is. De STM is gebaseerd op het aftasten ('scanning') van een preparaat met een scherp naaldje (de zogenaamde 'tip'), waarbij de electrische stroom (de 'tunneling current') gemeten wordt die van het naaldje naar het preparaat vloeit (zie Figuur 1.1). Hoewel de STM in principe uitermate geschikt is vanwege het hoge scheidend vermogen, blijkt het niet eenvoudig te zijn om een versie van de STM te ontwikkelen die magnetische ordening zichtbaar kan maken.

Een magnetische STM. In dit proefschrift wordt uitgelegd hoe magnetische gevoeligheid in een STM bereikt kan worden met behulp van gepolariseerd licht. Speciale tips zijn ontwikkeld die een hoge optische gevoeligheid hebben ('semiconductor tips'). Deze hebben het grote voordeel dat ze geen magnetisch veld opwekken, en dus het preparaat niet beïnvloeden. Hoofdstuk 2 bevat een algemene beschrijving van het gedrag van deze tips in de STM. De experimenten van Hoofdstuk 3 zijn gebaseerd op de polarisatie-afhankelijke absorptie van het licht in een magnetisch preparaat ('magneto-optical imaging'). Magnetische afbeeldingen worden getoond (zie Figuur 3.4) met een scheidend vermogen van ongeveer 250 nanometer; volgens onze modelberekeningen is met enige aanpassingen een verbetering met meer dan een factor tien haalbaar. Hoofdstuk 4 beschrijft de gevolgen van de polarisatie-afhankelijke absorptieprocessen in de tip ('optical spin-orientation'); de magnetische gevoeligheid wordt theoretisch beschreven en experimenteel aangetoond, wat de weg opent voor het daadwerkelijk bereiken van een magnetisch scheidend vermogen van een nanometer in een STM. Wegens haar relatieve eenvoud en gunstige eigenschappen, kan de in dit proefschrift ontwikkelde afbeeldingstechniek in de toekomst van groot belang worden voor het bestuderen en verbeteren van magnetische materialen.

Curriculum vitae

Menno Willem José Prins
geboren op 18 april 1967 te Renkum

1979-1985	Praedinius Gymnasium te Groningen.
1985-1988	Eerste drie studiejaren Technische Natuurkunde aan de Technische Universiteit Delft.
1988-1989	'Maîtrise de Physique et Applications' aan de Université Paris-Sud, [diploma met predikaat 'très bien'].
1989-1990	Afronding studie Technische Natuurkunde in de sectie Lage Temperaturen van prof. dr. H. Postma. Scriptietitel: 'Onderzoek aan hyperfijninteractie van onzuiverheden in grafiet' [ingenieursexamen TU Delft met predikaat 'cum laude'].
januari-mei 1991	Visiting scientist op het Indian Institute of Science in Bangalore.
juni 1991-juli 1995	In dienst van de Stichting FOM als Onderzoeker in Opleiding. Promotiewerk aan de Universiteit van Nijmegen, in de Vakgroep Experimentele Vaste-Stoffysica 2 onder leiding van prof. dr. H. van Kempen.
augustus 1995	In dienst van Philips Research te Eindhoven.

List of publications

'Spin-dependent transmission at ferromagnet/semiconductor interfaces',
M.W.J. Prins, D.L. Abraham, and H. van Kempen, J. Magn. Magn. Mat. **121**, 152-5 (1993); *ibid.*, Surf. Sci. **287/288**, 750-3 (1993).

'Nieuwe methode voor het meten van oppervlaktemagnetisme op subnanometer schaal', M.C.M.M. van der Wielen, R. Jansen, M.W.J. Prins, D.L. Abraham, and H. van Kempen, NEVAC blad **31**, 71-3 (1993).

'Inrichting voor het meten van de intensiteit en/of polarisatie van electromagnetische straling, voor het bepalen van fysische eigenschappen van een preparaat en voor het lezen van informatie vanaf een opslagmedium', H. van Kempen, D.L. Abraham, M.W.J. Prins, R. Jansen, en M.C.M.M. van der Wielen, Dutch patent 93.01617

'Progress toward spin-sensitive scanning tunneling microscopy using optical orientation in GaAs', R. Jansen, M.C.M.M. van der Wielen, M.W.J. Prins, D.L Abraham, and H. van Kempen, J. Vac. Sci. Technol. B**12**, 2133-5 (1994).

'Photoamperic probes in scanning tunneling microscopy',
M.W.J. Prins, M.C.M.M. van der Wielen, R. Jansen, D.L. Abraham, and H. van Kempen, Appl. Phys. Lett. **64**, 1207-9 (1994).

'Magneto-optical Faraday effect probed in a scanning tunneling microscope',
M.W.J. Prins, M.C.M.M. van der Wielen, D.L. Abraham, H. van Kempen,
and H.W. van Kesteren, IEEE Trans. Magn. **30**, 4491 (1994).

'Near-field magneto-optical imaging in scanning tunneling microscopy',
M.W.J. Prins, R.H.M. Groeneveld, D.L. Abraham, H. van Kempen,
and H.W. van Kesteren, Appl. Phys. Lett. **66**, 1141 (1995).

'Modulated photodetection with semiconductor tips in a scanning tunneling microscope', R.H.M. Groeneveld, M.W.J. Prins, and H. van Kempen, Surf. Sci. **331-333**, 1299 (1995).

'Photosensitive semiconductor tips in a scanning tunneling microscope', M.C.M.M. van der Wielen, M.W.J. Prins, R. Jansen, D.L. Abraham, and H. van Kempen, in 'Photons and local probes', edited by O. Marti, NATO-ASI (Elsevier, Amsterdam), accepted

'Depletion field focusing in semiconductors', M.W.J. Prins and A.P. van Gelder, submitted.

'Photoelectrical properties of semiconductor tips in scanning tunneling microscopy',
M.W.J. Prins, R. Jansen, R.H.M. Groeneveld, A.P. van Gelder, and H. van Kempen,
submitted.

'STM for magneto-optical imaging', M.W.J. Prins, R.H.M. Groeneveld, H.W. van
Kesteren, D.L. Abraham, R. Schad, and H. van Kempen, submitted.

'Spin-dependent transport in metal/semiconductor tunnel junctions',
M.W.J. Prins, H. van Kempen, H. van Leuken, R.A. de Groot, W. Van Roy, and J. De
Boeck, submitted.

'Spin-polarized tunneling with GaAs tips in scanning tunneling microscopy',
M.W.J. Prins, R. Jansen, and H. van Kempen, submitted.

• Magnetization-induced optical second-harmonic generation.

'Interface magnetism studied by optical second harmonic generation', G. Spierings,
V. Koutsos, H.A. Wierenga, M.W.J. Prins, D. Abraham, and Th. Rasing,
J. Magn. Magn. Mat. **121**, 109-11 (1993); *ibid.*, Surf. Sci. **287/288**, 747-9 (1993).

'Magnetisation-induced optical second-harmonic generation: a probe for interface mag-
netism', H.A. Wierenga, M.W.J. Prins, D.L. Abraham, and Th. Rasing,
Phys. Rev. **B50**, 1282-5 (1994).

'Magnetization induced optical second-harmonic generation from magnetic multilay-
ers', H.A. Wierenga, M.W.J. Prins, and Th. Rasing, Physica **204B**, 281 (1995).

'Interface magnetism and possible quantum well oscillations in ultrathin Co/Cu films
observed by magnetization induced second harmonic generation', H.A. Wierenga, W. de
Jong, M.W.J. Prins, Th. Rasing, R. Vollmer, A. Kirilyuk, H. Schwabe, and J. Kirschner,
Phys. Rev. Lett. **74**, 1462 (1995).

'Nonlinear and linear Kerr studies of Co/Cu multilayers', H.A. Wierenga, W. de Jong,
M.W.J. Prins, Th. Rasing, R. Vollmer, A. Kirilyuk, H. Schwabe, and J. Kirschner,
Surf. Sci. **331-333**, 1294 (1995).

• Other fields.

'Penetration depth of broadcast urea granules in puddled wetland rice soils',
M.W.J. Prins and P.A.C. Raats, Fertilizer Research **19**, 29-38 (1989).

'Nuclear electric quadrupole interaction of ion-implanted ^{203}Hg and ^{69m}Zn in graphite',
B. Kastelein, M.W.J. Prins, J. Andriessen, H. Postma, L. Klosterman, P. Herzog, and
J. Prinz, Phys. Rev. **B46**, 8818-27 (1992).

'Dependence of the reactivity of Ag and Ni clusters deposited on solid materials
on the cluster size', C.N.R. Rao, V. Vijayakrishnan, A.K. Santra, and M.W.J. Prins,
Angw. Chem. Int. ed. Eng. **31**, 1062 (1992); *ibid.*, Angew. Chemie **104**, 1110 (1992).

'An automated thermal relaxation calorimeter for operation at low temperature
$(0.5 < T < 10\,K)$', S. Banerjee, M.W.J. Prins, K.P Rajeev, and A.K. Raychaudhuri,
Pramana J. Phys. **39**, 391-404 (1992).

Stellingen behorend bij het proefschrift
'Magnetic imaging with photoexcited semiconductor tips
in scanning tunneling microscopy'
door Menno W.J. Prins.

1. Met behulp van halfgeleidende tips in een scanning tunneling microscoop is het mogelijk magneto-optische afbeeldingen te maken met een laterale magnetische resolutie beneden de optische diffractielimiet, waarbij een resolutie van een tiental nanometers tot de mogelijkheden behoort.
   Dit proefschrift.

2. De conclusie dat spin-gepolariseerd tunnelen door middel van optische oriëntatie in GaAs niet met lage lichtvermogens bewerkstelligd kan worden [D.T. Pierce, Phys. Scr. **38**, 291 (1988)] gaat voorbij aan de gunstige werking van de bandbuiging voor het verzamelen van ladingdragers aan het halfgeleideroppervlak.
   Dit proefschrift.

3. Voor het detecteren van spin-gepolariseerd tunnelen met behulp van optische oriëntatie in een scanning tunneling microscoop [K. Sueoka, K. Mukasa, and K. Hayakawa, Jpn. J. Appl. Phys. **32**, 2989 (1993)] is het essentieel in één meting de spin-gevoelige en spin-ongevoelige effecten te scheiden.
   Dit proefschrift.

4. Lokale optische excitatie van geoxydeerd GaAs geeft door electron-gat separatie in het bandbuigingsgebied een oppervlaktefotovoltage dat langs het oppervlak varieert. De beschrijving van het ladingtransport langs het halfgeleideroppervlak in termen van alleen diffusie [J. Qi, W. Angerer, M.S. Yeganeh, A.G. Yodh, and W.M. Theis, Phys. Rev. **B51**, 13533 (1995)] is daarom onjuist.

5. Pas in de daadwerkelijke uitvoering toont een goed idee zijn waarde. Daarom is:
   – bij de presentatie van een nieuw onderzoeksresultaat, de veel voorkomende reactie 'Dat hebben wij jaren geleden al bedacht' van generlei waarde.
   – het van groot belang, bij de beoordeling van een projectvoorstel, in rekening te brengen hoe voorgaande projecten zijn uitgevoerd.

6. Het leuke van muziekmaken is dat je nog eens wat van elkaar hoort.

7. Al vier jaar woedt een oorlog in Europa.

The scanning tunneling microscope (STM) is a suitable tool for investigating the atomic structure of surfaces. However, it has been difficult to develop a convenient magnetically sensitive version of the STM. This thesis reveals how that goal can be reached with optically excited semiconductor tips. Experiments show that a tunneling tip made of gallium arsenide can function as:

- a scanning near-field optical detector
  for magneto-optical Faraday/Kerr imaging, and

- a source of polarized electrons
  sensitive to the spin-structure of surfaces.

The observations are supported by theoretical modeling of the (spin-polarized) charge carrier flow in a metal/semiconductor STM junction.